PROCEEDINGS OF THE ROMANIAN ACADEMY

Series A:

Mathematics, Physics, Technical Sciences, Information Science

Volume 15, Number 3 *July–September 2014*

CONTENTS

MATHEMATICS

Hossein JAVANSHIRI, Mehdi NEMATI, *On certain product of Banach algebras and some of its properties* 219

PHYSICS

Khosro SAYEVAND, Dumitru BALEANU , Mojtaba FARDI, *A perturbative analysis of nonlinear cubic-quintic Duffing oscillators* 228

A. H. BHRAWY, A. A. ALSHAERY, E. M. HILAL, Daniela MILOVIC, Luminita MORARU, Michelle SAVESCU, Anjan BISWAS, *Optical solitons with polynomial and triple-power law nonlinearities and spatio-temporal dispersion* 235

Abdul-Majid WAZWAZ, *Multiple king solutions for the* (2+1)*-dimensional integrable Gardner equation* 241

Hana SEBESTOVA, Radim CTVRTLIK, Hana CHMELICKOVA, Jan TOMASTIK, *Micro and nanohardness testing of laser welds* 247

TECHNICAL SCIENCES

Maria VINȚAN, *Ground fault location influence on AC power lines impedance* 254

Iuliana-Florina CIORTAN, Ioan-Tiberiu GIURGIU, Cristina PUPĂZĂ, *Passive mitigation solutions using explicit dynamic simulation* 262

Cristian RUGINA, Adrian TOADER, Victor GIURGIUTIU, Ioan URSU, *The electromechanical impedance method for structural health monitoring of thin circular plates* 272

Zheng LIANG, Fei WANG, Xiong DENG, *Analytical-numerical coupling analysis of submarine pipeline in J-lay problem* 283

Marius GIUCLEA, Ana-Maria MITU, Ovidiu SOLOMON, *Generation of stationary Gaussian time series compatible with given power spectral density* 292

Abdolvahed KAMI, Bijan MOLLAEI DARIANI, Ali SADOUGH VANINI, Dan-Sorin COMSA, Dorel BANABIC, *Application of a GTN damage model to predict the fracture of metallic sheets subjected to deep-drawing* 300

INFORMATION SCIENCE

Mugurel-Ionuț ANDREICA, Nicolae ȚĂPUȘ, *Efficient computation of the number of solutions of the linear diophantine equqtion of Frobenius with small coefficients* 310

THE PUBLISHING HOUSE
OF THE ROMANIAN ACADEMY

PROCEEDINGS OF THE ROMANIAN ACADEMY, Series A,
Volume 15, Number 3/2014, pp. 219–227

ON A CERTAIN PRODUCT OF BANACH ALGEBRAS AND SOME OF ITS PROPERTIES

Hossossein JAVANSHIRI [1], Mehdi NEMATI [2,3]

[1] Yazd University, Department of Mathematics, P.O. Box: 89195-741, Yazd, Iran
[2] Isfahan University of Technology, Department of Mathematical Sciences, Isfahan 84156-83111, Iran
[3] Institute for Research in Fundamental Sciences (IPM), School of Mathematics, P. O. Box: 19395-5746, Tehran, Iran
E-mail: m.nemati@cc.iut.ac.ir

In this paper, for two arbitrary Banach algebras A and B and a homomorphism $T: B \to A$, we construct and study a product on the Cartesian product space $A \times B$, and we denote this algebra by $A \times_T B$. Among other things, we characterize the set of all continuous derivations from $A \times_T B$ into its nth dual space $(A \times_T B)^{(n)}$ and as an application we study the n-weak amenability of $A \times_T B$ and its relation with A and B. Moreover, we obtain characterizations of (bounded) approximate identities and study the ideal structure of these products.

Key words: Banach algebra, Arens regularity, weak amenability.

1. INTRODUCTION

The Lau product of two Banach algebras that are pre-duals of von Neumann algebras, and for which the identity of the dual is a multiplicative linear functional, was introduced and investigated by Lau [13]. This paper initiated a series of subsequent publications [6, 7, 9, 15, 16, 17] and has had a great impact. Extension to arbitrary Banach algebras was proposed by Monfared [14] with the notation $A \times_\theta B$, where θ is a non-zero multiplicative linear functionals on B.

Recently, a new extension of Lau product has been studied by Bhatt and Dabhi [1]. More precisely, for a *commutative* Banach algebra A and arbitrary Banach algebra B, by using the algebra homomorphism $T: B \to A$ they defined T-Lau product on the Cartesian product space $A \times B$ perturbing the pointwise-defined product resulting in a new Banach algebra $A \times_T B$, as follows

$$(a,b)(a',b') = (aa' + T(b)a' + T(b')a, bb'),$$

for all $a, a' \in A$ and $b, b' \in B$ and they investigated the Arens regularity and some notions of amenability of $A \times_T B$. Note that T-Lau product coincides with Lau product and θ-Lau product of Banach algebras. However, routine observations show that the imposed hypothesis on A for the definition of T-Lau product given by [1, p. 1] is too strong. As an evidence for this claim, recall that for two arbitrary Banach algebras A and B and a multiplicative linear functional $\theta: B \to \mathbb{C}$, Monfared [14, Corollary 2.13] proved that the Banach algebra $A \times_\theta B$ is Arens regular if and only if both A and B are Arens regular, but Bhatt and Dabhi [1, Theorem 3.1] proved the same result for $A \times_T B$ only when A is an Arens regular commutative Banach algebra; This is because of, on the one hand the commutativity assumption is needed in the Bhatt and Dabhi's definition, and on the other hand we know that the second dual of a commutative Banach algebra is commutative when it is Arens regular.

This paper continues these investigations. In Section 2, by a change in the Bhatt and Dabhi's definition we show that T-Lau products can be defined for Banach algebras in a fairly general setting; Indeed, we remove the commutativity assumption imposed on the definition of T-Lau products given by [1] and we show that we can recover most of the results obtained in [1] in the general case. Moreover, we study the ideal structure of T-Lau product of Banach algebras and we characterize the existence of the (bounded) approximate identity for this product. In the third part we introduce a bimodule action of $(A\times_T B)$ on $(A\times_T B)^{(n)}$ and, we characterize the set of all continuous derivations from $A\times_T B$ into $(A\times_T B)^{(n)}$, where $(A\times_T B)^{(n)}$ denotes the nth dual space of $A\times_T B$. Finally, we study the n-weak amenability of $A\times_T B$ and its relation with A and B and then we apply our results to some particular instances of Banach algebras such as quotient space of Banach algebras with a closed ideal, Banach algebras related to locally compact group and unital Banach algebra.

2. THE DEFINITION AND SOME BASIC RESULTS

Let A and B be arbitrary Banach algebras (not necessary commutative) and $T: B\to A$ be an algebra homomorphism. If we replaced the first coordinate of the ordered pair in equation (1) above by "$aa'+aT(b')+T(b)a'$", then $A\times_T B$ will be an associative algebra. So, we are lead to the following definition, where it paves the way to remove the commutativity assumption imposed on A in the definition of $A\times_T B$ given by [1, Page 1].

Definition 2.1. Let A and B be arbitrary Banach algebras and $T: B\to A$ be an algebra homomorphism. The T-Lau product $A\times_T B$ is defined as the Cartesian product $A\times B$ with the algebra product

$$(a,b)(a',b') := (aa'+aT(b')+T(b)a', bb'),$$

and the norm $\|(a,b)\| = \|a\|+\|b\|$ for all $a,a'\in A$ and $b,b'\in B$.

The reader will remark that, routine computations show that if $\|T\|\le 1$, then $A\times_T B$ is a Banach algebra. In what follows A and B are arbitrary Banach algebras and $T: B\to A$ is an algebra homomorphism, with $\|T\|\le 1$.

We now proceed to show that we can recover most of the results obtained in [1] in the general case. First, by an argument similar to the proof of [1, Theorem 2.1, Theorem 4.1], we can prove the following improvement of those. Note that in Theorems 2.1 and 4.1 of [1] the commutativity of A is needed only to conclude that $A\times_T B$ is Banach algebra; whereas by Definition 2.1 above this Banach spaces always is Banach algebra without any further assumptions on A. Moreover, the weak amenability of the Banach algebra $A\times_T B$ is considered in Corollary 3.6 below as a special case of the Propositions 3.4 and 3.5 in section 3 below.

THEOREM 2.2. *The following assertions hold.*

(i) *Let the Gelfand space $\Delta(B)$ is non-empty and*

$E=\{(\lambda,\lambda\circ T):\lambda\in\Delta(A)\}$, $F=\{(0,\phi):\phi\in\Delta(B)\}$. *Set $E=\varnothing$ if $\Delta(A)$ is emptyt. Then $\Delta(A\times_T B)$ is equal to the union of its closed disjoint set E and F.*

(ii) *$A\times_T B$ is amenable if and only if both A and B are amenable;*

(iii) *$A\times_T B$ is* (*approximately*) *cyclic amenable if and only if both A and B are* (*approximately*) *cyclic amenable.*

In order to state our next results we need to set some terminology. In what follows for a Banach space X the notation $X^{(n)}$ is used to denote the nth dual space of X and we always consider X as naturally embedded into $X^{(2)}$. For $x\in X$ and $f\in X^{(1)}$, by $\langle x,f\rangle$ (and also $\langle f,x\rangle$) we denote the natural duality

between X and $X^{(1)}$. Now let A be a Banach algebra. On $A^{(2)}$ there exists two natural products extending the one on A, known as the first and second Arens products of $A^{(2)}$. For a,b in A, f in $A^{(1)}$ and Φ,Ψ in $A^{(2)}$, the elements fa and Φf of $A^{(1)}$ and $\Psi\bullet\Phi$ of $A^{(2)}$ are defined, respectively, as follows.

$$\langle fa,b\rangle=\langle f,ab\rangle,\qquad \langle \Phi f,a\rangle=\langle \Phi,fa\rangle \qquad \text{and} \qquad \langle \Psi\bullet\Phi,f\rangle=\langle \Psi,\Phi f\rangle.$$

Also, the second Arens product "$\Diamond$" is defined using symmetry. Equipped with these products, $A^{(2)}$ is a Banach algebra and A is a subalgebra of it. These products are in general not separately weak* to weak* continuous on $A^{(2)}$. In general, the first and the second Arens products do not coincide on $A^{(2)}$ and A is said to be Arens regular if these products coincide on $A^{(2)}$. The first topological center $Z_t^1(A^{(2)})$ of $A^{(2)}$ is the set of all $\Phi\in A^{(2)}$ such that $\Phi\bullet\Psi=\Phi\Diamond\Psi$, for all $\Psi\in A^{(2)}$.

In [1, Theorem 3.1], Bhatt and Dahbi proved that if A is commutative and Arens regular Banach algebra, then

(i) $(A\times_T B)^{(2)}$ is isometrically isomorphic to $A^{(2)}\times_{T[2]} B^{(2)}$, when the algebras are equipped with the same either of its Arens products; (ii) $Z_t^1((A\times_T B)^{(2)})=A^{(2)}\times_{T[2]} Z_t^1(B^{(2)})$;

(iii) $A\times_T B$ is Arens regular if and only if B is Arens regular,

where $T^{[2]}$, the second adjoint of T, is a continuous homomorphisms in a natural way. Now, by an argument similar to the proof of [1, Theorem 3.1], we can prove the following improvement of it; Indeed, we remove the following assumptions from the Bhatt-Dahbi's result for Arens regularity of $A\times_T B$:

- The commutativity assumption on A,
- The Arens regularity assumption on A.

Note that, the Banach algebra $A^{(2)}$ is commutative, if the underlying Banach algebra is commutative and Arens regular, so in Theorem 3.1 of [1] the commutativity and Arens regularity of A are needed only to conclude that $A\times_T B$ and $A^{(2)}\times_{T[2]} B^{(2)}$ are Banach algebras; whereas by Definition 2.1 above these Banach spaces always are Banach algebras without any further assumptions on A.

THEOREM 2.3. T*he following assertions hold.*

(i) $(A\times_T B)^{(2)}$ *is isometrically isomorphic to the* $A^{(2)}\times_{T[2]} B^{(2)}$*;*

(ii) $Z_t^1((A\times_T B)^{(2)})=Z_t^1(A^{(2)})\times_{T[2]} Z_t^1(B^{(2)})$;

(iii) $A\times_T B$ *is Arens regular if and only if both* A *and* B *are Arens regular*.

We end this section by the following three results, which are of interest in its own right.

PROPOSITION 2.4. *Let* I *be a left ideal of* A *and* J *be a left ideal of* B*. Then the following assertions hold.*

(i) *If* $T(J)\subseteq I$*. Then* $I\times_T J$ *is a left ideal of* $A\times_T B$.

(ii) *If* I *is a prime left ideal and* $I\times_T J$ *is a left ideal of* $A\times_T B$*, then* $T(J)\subseteq I$.

(iii) *If* A *is a unital Banach algebra. Then* $I\times_T J$ *is a left ideal of* $A\times_T B$ *if and only if* $T(J)\subseteq I$.

(iv) *If* I *is a close left ideal of* A *and, suppose that* A *has a left approximate identity. Then* $I\times_T J$ *is a left ideal of* $A\times_T B$ *if and only if* $T(J)\subseteq I$.

Proof. The proof of (i) is routine and is omitted. For the proof of (ii) we need only note that if I is a prime ideal of A and $I\times_T J$ is an ideal of $A\times_T B$, then $T(J)\subseteq I$. To this end, assume that there exists $b'\in J$ such that $T(b')\notin I$. Then

$$(a,0)(a',b')=(aa'+aT(b'),0)\in I\times_T J,$$

for all $a'\in I$ and $a\in A\setminus I$, which contradicts with assumption.

(iv) Let $(a_\alpha)_\alpha$ be a left approximate identity for A, and suppose that $a' \in I$ and $b' \in J$. Then

$$(a_\alpha, 0)(a', b') = (a_\alpha a' + a_\alpha T(b'), 0) \in I \times_T J,$$

for all α. Since I is closed it follows that $a' + T(b') \in I$. Consequently, $T(J) \subseteq I$. Finally, note that one can prove the assertion (iii) by the same manner as in the proof of (iv).□

Next we consider the converse.

PROPOSITION 2.5. *Let N be a left ideal of $A \times_T B$ and*
$I = \{a \in A : (a,b) \in N \text{ for some } b \in B\}$, $J = \{b \in B : (a,b) \in N \text{ for some } a \in A\}$.
Then the following assertions hold.

(i) *J is a left ideal in B.*

(ii) *If T is onto, then I is a left ideal of A.*

(iii) *If N is closed and A has a left approximate identity, then a necessary condition for the equality $N = I \times_T J$ is that $T(J) \subseteq I$.*

Proof. For briefness we only give the proof for (ii) and (iii). Let $c \in I$ and $a \in A$. Then there exists $b \in B$ such that $T(b) = a$. Therefore, $(a,b)(c,0) \in N$ and hence $ac \in I$. Now, we give a proof for (iii). To this end, let $N = I \times_T J$ and $j \in J$. Then there is $i \in I$ such that $(i,j) \in N$. If now $(a_\alpha)_\alpha$ is a left approximate identity for A, then $(a_\alpha, 0)(i,j) \in N$. Hence $i + T(j) \in I$ and this implies that $T(j) \in I$.□

PROPOSITION 2.6. *The Banach algebra $A \times_T B$ has a bounded* (*resp. unbounded*) *left* (*resp. right, or two-sided*) *approximate identity if and only if A and B have the same approximate identity.*

Proof. First assume that the nets $(a_\alpha)_\alpha$ and $(b_\alpha)_\alpha$ are bounded left approximate identities for A and B, respectively. Then the net $((a_\alpha - T(b_\alpha), b_\alpha))_\alpha$ is a bounded left approximate identity for $A \times_T B$; Indeed, for every $(a,b) \in A \times_T B$

$$(a_\alpha - T(b_\alpha), b_\alpha)(a,b) = ((a_\alpha - T(b_\alpha))a + T(b_\alpha)a + (a_\alpha - T(b_\alpha))T(b), b_\alpha b).$$

Conversely, if $((a_\alpha, b_\alpha))_\alpha$ is a bounded left approximate identity for $A \times_T B$, then the nets $(a_\alpha + T(b_\alpha))_\alpha$ and $(b_\alpha)_\alpha$ are bounded. Also for every $a \in A$ and $b \in B$ we must have

$$\|b_\alpha b - b\| \le \|(a_\alpha, b_\alpha)(0,b) - (0,b)\| \to 0, \quad \|(a_\alpha + T(b_\alpha))a - a\| = \|(a_\alpha, b_\alpha)(a,0) - (a,0)\| \to 0.$$

Since a and b are arbitrary we conclude that the nets $(a_\alpha + T(b_\alpha))_\alpha$ and $(b_\alpha)_\alpha$ $(b_\alpha)_\alpha$ are bounded left approximate identities for A and B, respectively. This completes the proof of this proposition, since one can obtain a proof for other cases by similar argument. □

3. DERIVATIONS INTO ITERATED DUALS

We commence this section with some notations. In this section A and B are two arbitrary Banach algebras and $T : B \to A$ be an algebra homomorphism with norm at most 1. Then $(A \times_T B)^{(1)}$, the first dual space of $A \times_T B$, can be identified with $A^{(1)} \times B^{(1)}$ in the natural way

$$\langle (a^{(1)}, b^{(1)}), (a,b) \rangle = \langle a^{(1)}, a \rangle + \langle b^{(1)}, b \rangle,$$

for all $a \in A, b \in B, a^{(1)} \in A^{(1)}$ and $b^{(1)} \in B^{(1)}$. The dual norm on $A^{(1)} \times B^{(1)}$ is of course the maximum norm $\|(a^{(1)}, b^{(1)})\| = \max\{\|a^{(1)}\|, \|b^{(1)}\|\}$. Now for integer $n \ge 0$, take $A^{(n)} \times B^{(n)}$ as the underlying space of

$(A\times_T B)^{(n)}$. From induction, we can find that the $(A\times_T B)$-bimodule actions on $(A\times_T B)^{(n)}$ are formulated as follows:

$$(a,b)\cdot(a^{(n)},b^{(n)})=\begin{cases}\left((a+T(b))\cdot a^{(n)}+a\cdot T^{[n]}(b^{(n)}),b\cdot b^{(n)}\right) & \text{if } n \text{ is even}\\ \left((a+T(b))\cdot a^{(n)},T^{[n]}(a\cdot a^{(n)})+b\cdot b^{(n)}\right) & \text{if } n \text{ is odd}\end{cases}$$

and

$$(a^{(n)},b^{(n)})\cdot(a,b)=\begin{cases}\left(a^{(n)}\cdot(a+T(b))+T^{[n]}(b^{(n)})\cdot a,b^{(n)}\cdot b\right) & \text{if } n \text{ is even}\\ \left(a^{(n)}\cdot(a+T(b)),T^{[n]}(a^{(n)}\cdot a)+b^{(n)}\cdot b\right) & \text{if } n \text{ is odd,}\end{cases}$$

for all $(a,b)\in A\times_T B$ and $(a^{(n)},b^{(n)})\in A^{(n)}\times B^{(n)}$, where $T^{[n]}$ denotes the n-th adjoint of T.

Let A be a Banach algebra and X be a Banach A-bimodule. Then a linear map $D:A\to X$ is called a derivation if $D(ab)=a\cdot D(b)+D(a)\cdot b,$ for all $a,b\in A$. For $x\in X$, we define $d_x:A\to X$ as follows $d_x(a)=a\cdot x-x\cdot a,$ for all $a,b\in A$. It is easy to show that d_x is a derivation; such derivations are called inner derivations. A derivation $D:A\to X$ is called inner if there exist $x\in X$ such that $D=d_x$. We denote the set of all continuous derivations from A into X by $Z^1(A,X)$. The first cohomology group $H^1(A,X)$ is the quotient of the space of continuous derivations by the inner derivations, and in many situations triviality of this space is of considerable importance. In particular, A is called contractible if $H^1(A,X)=0$ for every Banach A-bimodule X, A is called amenable if $H^1(A,X^{(1)})=0$ for every Banach A-bimodule X, for every $n\geq 0$, A is called n-weakly amenable if $H^1(A,A^{(n)})=0$, and weakly amenable if A is 1-weakly amenable, where $A^{(n)}$ is the n-th dual module of A when $n\geq 1$, and is A itself when $n=0$. Let us mention that, the concept of weak amenability was first introduced and intensively studied by Bade, Curtis and Dales [2] for commutative Banach algebras, and then by Johnson [12] for a general Banach algebra. Dales, Ghahramani and Grønbæk [4] initiated and intensively developed the study of n-weak amenability of Banach algebras; see also [8, 10, 11, 18].

The following result characterize the set of all continuous derivations from $A\times_T B$ into $(A\times_T B)$-bimodule $(A\times_T B)^{(2n+1)}$. In the sequel the notation M is used to denote the T-Lau product of the Banach algebras A and B.

THEOREM 3.1. *Let $M=A\times_T B$ and $n\geq 0$. Then $D\in Z^1(M,M^{(2n+1)})$ if and only if there exist $d_1\in Z^1(A,A^{(2n+1)})$, $d_2\in Z^1(B,B^{(2n+1)})$, $d_3\in Z^1(B,A^{(2n+1)})$ and a bounded linear map $S:A\to B^{(2n+1)}$, such that for each $a,a'\in A$ and $b\in B$;*

(i) $D((a,b))=(d_1(a)+d_3(b),S(a)+d_2(b))$,

(ii) $d_1(T(b)a)=d_3(b)a+T(b)d_1(a)$,

(iii) $d_1(aT(b))=ad_3(b)+d_1(a)T(b)$,

(iv) $S(T(b)a)=T^{[2n+1]}(d_3(b)a)+bS(a)$,

(v) $S(aT(b))=T^{[2n+1]}(a\ \ d_3(b))+S(a)b$,

(vi) $S(aa')=T^{[2n+1]}(d_1(aa'))$.

Proof. Suppose that $D\in Z^1(M,M^{(2n+1)})$. Then there exist bounded linear maps $D_1:A\times B\to A^{(2n+1)}$ and $D_2:A\times B\to B^{(2n+1)}$ such that $D=(D_1,D_2)$. Let $d_1(a)=D_1((a,0))$, $d_2(b)=D_2((0,b))$, $d_3(b)=D_1((0,b))$ and $S(a)=D_2((a,0))$ for all $a\in A$ and $b\in B$. Then trivially d_1, d_2, d_3 and S are linear maps satisfying (i). Moreover for every $a,a'\in A$ and $b,b'\in B$ we have

$$\begin{aligned} &D((a,b)(a',b')) = D((aa' + T(b)a' + aT(b'), bb')) = \\ &\big(d_1(aa' + T(b)a' + aT(b')) + d_3(bb'), d_2(bb') + S(aa' + T(b)a' + aT(b'))\big), \end{aligned} \tag{1}$$

and

$$\begin{aligned} &D((a,b))(a',b') + (a,b)D((a',b')) = \\ &= \big(d_1(a) + d_3(b), S(a) + d_2(b)\big)(a',b') + (a',b')\big(d_1(a') + d_3(b'), S(a') + d_2(b')\big) = \\ &= \Big((d_1(a) + d_3(b))a' + (d_1(a) + d_3(b))T(b'), T^{[2n+1]}((d_1(a) + d_3(b))a')) + (S(a) + d_2(b))b'\Big) = \\ &+ \Big(a(d_1(a') + d_3(b')) + T(b)(d_1(a') + d_3(b')), T^{[2n+1]}(a(d_1(a') + d_3(b'))) + b(S(a') + d_2(b'))\Big). \end{aligned} \tag{2}$$

It follows that $D \in Z^1(M, M^{(2n+1)})$ if and only if (1) and (2) coincide. Thus

$$\begin{aligned} d_1(aa' + T(b)a' + aT(b')) + d_3(bb') = d_1(a)a' + d_3(b)a' + d_1(a)T(b') + d_3(b)T(b') \\ + ad_1(a') + ad_3(b') + T(b)d_1(a') + T(b)d_3(b'), \end{aligned} \tag{3}$$

and

$$\begin{aligned} S\big(aa' + T(b)a' + aT(b')\big) + d_2(bb') = T^{[2n+1]}\big(d_1(a)a' + d_3(b)a'\big) + S(a)b' \\ + d_2(b)b' + T^{[2n+1]}\big(ad_1(a') + ad_3(b')\big) + bS(a') + bd_2(b'). \end{aligned} \tag{4}$$

Therefore $D \in Z^1(M, M^{(2n+1)})$ if and only if the equations (3) and (4) are satisfied. Now a straightforward verification shows that if d_1, d_2 and d_3 are derivations and the equalities (ii), (iii), (iv), (v), (vi) are satisfied, then (3) and (4) are valid. Applying (3) and (4) for suitable values of a, a', b, b' shows that d_1, d_2 and d_3 are derivations and the equalities (ii), (iii), (iv), (v), (vi) are also satisfied, as claimed. □

As an immediate corollary we have the following result, which characterize the set of all inner derivations from $A \times_T B$ into $(A \times_T B)$-bimodule $(A \times_T B)^{(2n+1)}$.

COROLLARY 3.2. *Let* $M = A \times_T B$ *and* $n \geq 0$. *Then* $D \in Z^1(M, M^{(2n+1)})$ *and* $D = d_{\left(a^{(2n+1)}, b^{(2n+1)}\right)}$ *if and only if* $D((a,b)) = \big(d_1(a) + d_3(b), S(a) + d_2(b)\big)$, *for all* $a \in A$ *and* $b \in B$, *where* $d_1 = d_{a^{(2n+1)}}$, $d_2 = d_{b^{(2n+1)}}$, $d_3 = d_{a^{(2n+1)}}$, $S = \delta_{a^{(2n+1)}}$ *and* $\delta_{a^{(2n+1)}}(a) = T^{[2n+1]}(d_{a^{(2n+1)}}(a))$ *for all* $a \in A$.

Proof. For the proof we need only note that if $D = d_{\left(a^{(2n+1)}, b^{(2n+1)}\right)}$ for some $a^{(2n+1)} \in A^{(2n+1)}$ and $b^{(2n+1)} \in B^{(2n+1)}$, then

$$\big(d_1(a), S(a)\big) = D((a,0)) = d_{\left(a^{(2n+1)}, b^{(2n+1)}\right)}(a,0) = \Big(d_{a^{(2n+1)}}(a), T^{[2n+1]}(d_{a^{(2n+1)}}(a))\Big),$$

for all $a \in A$. It follows that $d_1 = d_{a^{(2n+1)}}$ and $S = \delta_{a^{(2n+1)}}$. Similarly $d_2 = d_{b^{(2n+1)}}$ and $d_3 = d_{a^{(2n+1)}}$, and this completes the proof. □

By replacing $(2n+1)$ by $(2n)$ in Theorem 3.1 and Corollary 3.2 and using a similar argument, one can obtain the following result.

THEOREM 3.3. *Let* $M = A \times_T B$ *and* $n \geq 0$. *Then* $D \in Z^1(M, M^{(2n)})$ *if and only if there exist* $d_2 \in Z^1(B, B^{(2n)})$, $d_3 \in Z^1(B, A^{(2n)})$ *and bounded linear maps* $S : A \to B^{(2n)}$ *and* $R : A \to A^{(2n)}$ *such that for each* $a, a' \in A$ *and* $b \in B$;

(i) $D((a,b)) = (R(a) + d_3(b), S(a) + d_2(b))$,

(ii) $R(aa') = R(a)a' + T^{[2n]}(S(a))a' + aR(a') + aT^{[2n]}(S(a'))$,

(iii) $R(T(b)a) = d_3(b)a + T^{[2n]}(d_2(b))a + T(b)R(a)$,
(iv) $R(aT(b)) = ad_3(b) + aT^{[2n]}(d_2(b)) + R(a)T(b)$,
(v) $S(T(b)a) = bS(a)$,
(vi) $S(aT(b)) = S(a)b$,
(vii) $S(aa') = 0$.
Moreover, $D = d_{\left(a^{(2n)}, b^{(2n)}\right)}$ *if and only if* $R = d_{a^{(2n)} + T^{[2n]}(b^{(2n)})}$, $S = 0$, $d_2 = d_{b^{(2n)}}$ *and* $d_3 = d_{a^{(2n)}}$.

Now we apply these results to study the n-weak amenability of $A \times_T B$. Our starting point is the following proposition which gives a necessary condition for the $(2n+1)$-weak amenability of $A \times_T B$.

PROPOSITION 3.4. *Let* $M = A \times_T B$ *be* $(2n+1)$*-weakly amenable for some* $n \geq 0$. *Then* A *and* B *are* $(2n+1)$*-weakly amenable.*

Proof. Suppose that $d_1 \in Z^1(A, A^{(2n+1)})$ and $d_2 \in Z^1(B, B^{(2n+1)})$. By Theorem 3.1 we conclude that the map $D : A \times_T B \to A^{(2n+1)} \times B^{(2n+1)}$ defined by

$$D((a,b)) = \left(d_1(a) + d_3(b), S(a) + d_2(b)\right) \ \left((a,b) \in A \times_T B\right),$$

is a derivation, where $d_3 = d_1 \circ T$ and $S = T^{[2n+1]} \circ d_1$. Therefore, there exists $\left(a^{(2n+1)}, b^{(2n+1)}\right) \in A^{(2n+1)} \times B^{(2n+1)}$ such that $D = d_{\left(a^{(2n+1)}, b^{(2n+1)}\right)}$. Hence, $d_1 = d_{a^{(2n+1)}}$ and $d_2 = d_{b^{(2n+1)}}$ by Corollary 3.2.□

In the following proposition, for $n \geq 0$ we denote by $X_{A^{(2n)}}$ the closed linear span of the set $\left(A \cdot A^{(2n)} \cup A^{(2n)} \cdot A\right)$ in $A^{(2n)}$. The following result, with a suitable condition, gives a sufficient condition for the $(2n+1)$-weak amenability of $A \times_T B$.

PROPOSITION 3.5. *Let* n *be a positive integer number such that* $X_{A^{(2n)}} = A^{(2n)}$. *If* A *and* B *are* $(2n+1)$*-weakly amenable, then* M *is* $(2n+1)$*-weakly amenable.*

Proof. Suppose that $D \in Z^1(M, M^{(2n+1)})$. Then there exist $d_1 \in Z^1(A, A^{(2n+1)})$, $d_2 \in Z^1(B, B^{(2n+1)})$, $d_3 \in Z^1(B, A^{(2n+1)})$ and a bounded linear map $S : A \to B^{(2n+1)}$ such that

$$D((a,b)) = (d_1(a) + d_3(b), S(a) + d_2(b)),$$

for all $(a,b) \in A \times B$. By assumption there exist $a^{(2n+1)} \in A^{(2n+1)}$ and $b^{(2n+1)} \in B^{(2n+1)}$ such that $d_1 = d_{a^{(2n+1)}}$ and $d_2 = d_{b^{(2n+1)}}$. Thus, by Theorem 3.1, we have $S(aa') = T^{[2n+1]}(d_1(aa'))$, for all $a, a' \in A$. Since A is $(2n+1)$-weak amenable, it follows that $\overline{A^2} = A$. Hence, we conclude that $S = T^{[2n+1]} \circ d_1 = \delta_{a^{(2n+1)}}$. On the other hand by Theorem 3.1 and Corollary 3.2, we have

$$d_{a^{(2n+1)}}(T(b)a) = d_3(b)a + T(b)d_{a^{(2n+1)}}(a),$$

for all $a \in A$ and $b \in B$. Therefore, $\left(d_3(b) - d_{a^{(2n+1)}}(T(b))\right)a = 0$ for all $a \in A$ and $b \in B$. By replacing d'_3 with $(d_3 - d_{a^{(2n+1)}})$ we conclude that $d'_3(b)|_{\overline{A.A^{(2n)}}} = 0$ for all $b \in B$. Similarly we can show that $d'_3(b)|_{\overline{A^{(2n)}.A}} = 0$ for all $b \in B$. It follows from assumption that $d_3 = d_{a^{(2n+1)}}$. Hence, $D = d_{\left(a^{(2n+1)}, b^{(2n+1)}\right)}$ by Theorem 3.1.□

We recall from [4, Proposition 1.2] that if A is weakly amenable, then $\overline{A^2} = A$. Thus by Propositions 3.4 and 3.5 we have the following result.

COROLLARY 3.6. *A and B are weakly amenable if and only if M is weak amenable.*

Below we observe that *2n*-weak amenability of A is necessary for $2n$-weak amenability of M.

PROPOSITION 3.7. *Let $M = A \times_T B$ be $2n$-weakly amenable for some $n \geq 0$. Then A is $2n$-weakly amenable and all derivations $d_2 \in Z^1(B, B^{(2n)})$ with $d_2(B) \subseteq \ker T^{[2n]}$ are inner.*

Proof. Suppose that $d_1 \in Z^1(A, A^{(2n+1)})$ and $d_2 \in Z^1(B, B^{(2n)})$ such that $d_2(B) \subseteq \ker T^{[2n]}$. By Theorem 3.3, we conclude that the map $D : A \times_T B \to A^{(2n)} \times_{T^{[2n]}} B^{(2n)}$ defined by

$$D((a,b)) = \big(d_1(a) + d_1(T(b)), d_2(b)\big) \quad \big((a,b) \in A \times_T B\big),$$

is a derivation. Therefore, there exists $(a^{(2n)}, b^{(2n)}) \in A^{(2n)} \times_{T^{[2n]}} B^{(2n)}$ such that $D = d_{\left(a^{(2n)}, b^{(2n)}\right)}$. It follows that $d_1 = d_{a^{(2n)} +_T {}^{[2n]} (b^{(2n)})}$ and $d_2 = d_{b^{(2n)}}$. ■

Let I be a closed ideal in A. Then it is trivial that the natural quotient map $q : A \to A/I$ is an algebra homomorphism with $\|q\| \leq 1$. In particular $\ker q = I$ and $\ker q^{[2n]} \cong I^{(2n)}$ for all $n \geq 0$.

COROLLARY 3.8. *Let I be a closed ideal in A and $n \geq 0$. Suppose that $A/I \times_q A$ is $2n$-weakly amenable. Then A/I is $2n$-weakly amenable and each derivation from A into $I^{(2n)}$ is inner.*

As two applications of Theorems 3.1 and 3.3, for the case that A is unital we have the following characterizations for elements in $Z^1(A \times_T B, (A \times_T B)^{(n)})$.

COROLLARY 3.9. *Let A be unital and $n \geq 0$. Then $D \in Z^1(M, M^{(2n+1)})$ if and only if*

$$D((a,b)) = \big(d_1(a) + d_3(b), S(a) + d_2(b)\big),$$

where $d_1 \in Z^1(A, A^{(2n+1)})$, $d_2 \in Z^1(B, B^{(2n+1)})$, $d_3 \in Z^1(B, A^{(2n+1)})$ and $S : A \to B^{(2n+1)}$ is a bounded linear map such that $d_3 = d_1 \circ T$ and $S = T^{[2n+1]} \circ d_1$. Moreover, D is inner if and only if both d_1 and d_2 are inner.

COROLLARY 3.10. *Let A be unital and $n \geq 0$. Then $D \in Z^1(M, M^{(2n)})$ if and only if*

$$D((a,b)) = \big(d_1(a) + d_3(b), d_2(b)\big),$$

where $d_1 \in Z^1(A, A^{(2n)})$, $d_2 \in Z^1(B, B^{(2n)})$ and $d_3 \in Z^1(B, A^{(2n)})$ such that $d_3 = d_1 \circ T - T^{[2n]} \circ d_2$. Moreover, D is inner if and only if both d_1 and d_2 are inner.

As an immediate corollary we have the following result. The details are omitted.

PROPOSITION 3.11. *Let A be unital and $n \geq 0$. Then M is n-weakly amenable if and only if A and B are n-weakly amenable.*

We end this work with the following example.

EXAMPLE 3.12. (*i*) It is well known that for any locally compact group G, the group algebra $L^1(G)$ is n-weakly amenable for all $n \in N$. Now, suppose that G_1 and G_2 are two locally compact groups and let

$T: L^1(G_1) \to L^1(G_2)$ be an algebra homomorphism with $\|T\| \leq 1$. Then $L^1(G_1) \times_T L^1(G_2)$ is weakly amenable by Corollary 3.6.

(*ii*) Let $T: M(G_1) \to L^1(G_2)$ be an algebra homomorphism with $\|T\| \leq 1$. Then [5, Theorem 1.2] and Proposition 3.11 implies that G_1 is discrete if and only if $M(G_1) \times_T L^1(G_2)$ is n-weakly amenable for all $n \in N$.

ACKNOWLEDGEMENTS

The authors would like to express their sincere thanks to the referee for invaluable comments that helped us to improve considerably the presentation of this paper. The second author's research was supported in part by a grant from IPM (No. 92470046).

REFERENCES

1. BHATT, S. J., DABHI, P. A., *Arens regularity and amenability of Lau product of Banach algebras defined by a Banach algebra morphism*, Bull. Austral. Math. Soc., **87**, pp. 195–206, 2013.
2. BADE, W. G., CURTIS, P. C., DALES, H. G., *Amenability and weak amenability for Beurling and Lipschits algebras*, Proc. Londan Math. Soc., **55** , pp. 359–377, 1987.
3. BONSAL, F. F.,DUNCAN, J., *Complete normed algebras*, Springer, Berlin, 1973.
4. DALES, H. G., GHAHRAMANI, F., GRØNBÆK, N., *Derivations into iterated duals of Banach algebras*, Studia Math., **128**, pp. 19–53, 1998.
5. DALES, H. D., GHAHRAMANI, F., HELEMSKII, A. Ya., *The amenability of measure algebras*, J. London Math. Soc., **66**, pp. 213–226, 2002.
6. E. VISHKI, H. R., KHODAMI, A. R., *Character inner amenability of certain Banach algebras*, Colloq. Math., **122**, pp. 225–232, 2011.
7. GHADERI, E., NASR-ISFAHANI, R., NEMATI, M., *Some notions of amenability for certain products of Banach algebras*, Colloq. Math., **130** , pp. 147–157, 2013.
8. H. AZAR, K. RIAZI, A., *A generalization of the weak amenability of some Banach algebras*, Proc. Rom. Acad. Ser. A. Math. Phys. Tech. Sci. Inf. Sci., **12** , pp. 9–15, 2011.
9. HU, Z., MONFARED, M. S., TRAYNOR, T., *On character amenable Banach algebras*, Studia Math., **193**, pp. 53–78, 2009.
10. JOHNSON, B. E., *Cohomology in Banach Algebras*, Mem. Amer. Math. Soc., **127**, 1972.
11. JOHNSON, B. E., *Weak amenability of group algebras*, Bull. Lodon Math. Soc. **23**, pp. 281–284, 1991.
12. JOHNSON, B. E., *Derivations from* $L^1(G)$ *into* $L^1(G)$ *and* $L^\infty(G)$, Lecture Notes in Math., **1359**, Springer, Berlin, New York, pp. 191–198, 1988.
13. LAU, A. T., *Analysis on a class of Banach algebras with applications to harmonic analysis on locally compact groups and semigroups*, Fund. Math., **118**, pp. 161–175, 1983.
14. MONFARED, M. S., *On certain products of Banach algebras with applications to harmonic analysis*, Studia Math., **178**, pp. 277–294, 2007.
15. MONFARED, M. S, *Character amenability of Banach algebras*, Math. Proc. Cambridge Philos. Soc., **144**, pp. 697–706, 2008.
16. NASR-ISFAHANI, R., NEMATI, M., *Essential character amenability of Banach algebras*, Bull. Aust. Math. Soc., **84**, pp. 372–3866, 2011.
17. NASR-ISFAHANI, R., NEMATI, M., *Cohomological characterizations of character seudo-amenable Banach algebras*, Bull. Aust. Math. Soc., **84**, pp. 229–2377, 2011.
18. YAZDANPANAH, T., *Weak amenability of tensor product of Banach algebras*, Proc. Rom. Acad. Ser. A Math. Phys. Tech. Sci. Inf. Sci., **13**, pp. 310–313, 2012.

Received February 24, 2014

THE PUBLISHING HOUSE
OF THE ROMANIAN ACADEMY

PROCEEDINGS OF THE ROMANIAN ACADEMY, Series A,
Volume 15, Number 3/2014, pp. 228–234

A PERTURBATIVE ANALYSIS OF NONLINEAR CUBIC-QUINTIC DUFFING OSCILLATORS

Khosro SAYEVAND [1], Dumitru BALEANU [2], Mojtaba FARDI [3]

[1] Malayer University, Faculty of Mathematical Sciences, Malayer, Iran
[2] Cankaya University, Faculty of Art and Sciences, Department of Mathematics and Computer Sciences, Ankara, Turkey
[2] King Abdulaziz University, Faculty of Engineering, Department of Chemical and Materials Engineering, P.O. Box 80204, Jeddah, 21589, Saudi Arabia
[2] Institute of Space Sciences, MG-23, R 76900, Magurele-Bucharest, Romania
[3] Islamic Azad University, Department of Mathematics, Najafabad Branch, Najafabad, Iran
E-mail: ksayehvand@malayeru.ac.ir

Duffing oscillators comprise one of the canonical examples of Hamilton systems. The presence of a quintic term makes the cubic-quintic Duffing oscillator more complex and interesting to study. In this paper, the homotopy analysis method (HAM) is used to obtain the analytical solution for the nonlinear cubic-quintic Duffing oscillators. The HAM helps to obtain the frequency ω in the form of approximation series of a convergence control parameter $\hbar$. The valid region of $\hbar$ is determined by plotting the ω - $\hbar$ curve and afterwards we compared the obtained results with the exact solutions.

Key words: homotopy analysis method, homotopy-Padé technique, oscillator.

1. INTRODUCTION

Duffing equation is used to model the conservative double-well oscillators, which can occur, for example, in magneto-elastic mechanical systems [1]. These systems can be presented in the following form

$$\begin{cases} \dfrac{\mathrm{d}^2u}{\mathrm{d}t^2} + \alpha u(t) + \beta u^3(t) + \gamma u^5(t) = 0, \\ u(0) = B, \qquad u'(0) = 0, \end{cases} \tag{1}$$

where B is the amplitude of the oscillator. Under the initial conditions mentioned above the nonlinear cubic-quintic Duffing oscillator has the exact frequency [2]:

$$\begin{aligned} \omega_\varepsilon &= \frac{\pi\sqrt{\alpha + \beta\dfrac{B^2}{2} + \gamma\dfrac{B^4}{4}}}{2\displaystyle\int_0^{\frac{\pi}{2}} (1 + M\ \sin^2(t) + N\ \sin^4(t))^{\frac{-1}{2}}\,\mathrm{d}t}, \\ M &= \frac{3\beta B^2 + 2\gamma B^4}{6\alpha + 3\beta B^2 + 2\gamma B^4}, \\ N &= \frac{2\gamma B^4}{6\alpha + 3\beta B^2 + 2\gamma B^4}. \end{aligned} \tag{2}$$

Eq. (1) describes an oscillator with an unknown frequency ω. Under the transformations

$$\tau = \omega t, \quad u(t) = BU(\tau), \tag{3}$$

the original Eq. (1) becomes

$$\begin{cases} \omega^2 \dfrac{\mathrm{d}^2 U}{\mathrm{d}\tau^2} + \alpha U(\tau) + B^2 \beta U^3(\tau) + B^4 \gamma U^5(\tau) = 0, \\ U(0) = 1, \quad U'(0) = 0. \end{cases} \tag{4}$$

In the present paper, we use the homotopy analysis method (HAM) to obtain the periodic solutions of the nonlinear cubic-quintic Duffing oscillators. It is to be noted that Liao [3] employed the basic ideas of the homotopy to overcome the restrictions of traditional techniques [4–18] namely the HAM. Notice that the HAM contains an auxiliary parameter $\hbar$ which provides a convenient way to control the convergence region and the rate of approximation series. Liao investigated the influence of $\hbar$ on the convergence of solution series by means of $\hbar$-curves [3].

2. APPLICATION OF HOMOTOPY ANALYSIS METHOD

The periodic solution of $U(\tau)$ with the frequency ω can be written as

$$U(\tau) = \sum_{m=0}^{\infty} c_m \cos(m\tau), \tag{5}$$

where c_m are coefficients. It is convenient to choose

$$U_0(\tau) = \cos\tau, \tag{6}$$

as the initial guess of $U(\tau)$. Let ω_0 denotes the initial guess of ω, then we choose the auxiliary linear operator

$$L\left[\varphi(\tau;q)\right] = \omega_0^2 \left[\frac{\mathrm{d}^2 \varphi(\tau;q)}{\mathrm{d}\tau^2} + \varphi(\tau;q) \right], \tag{7}$$

with the property

$$L\left[C_1 \cos\tau + C_2 \sin\tau\right] = 0, \tag{8}$$

where C_1 and C_2 are coefficients. We define a nonlinear operator

$$N\left[\varphi(\tau;q), \Omega(q)\right] = \Omega^2(q) \frac{\mathrm{d}^2 \varphi(\tau;q)}{\mathrm{d}\tau^2} + \alpha\varphi(\tau;q) + B^2 \beta \varphi^3(\tau;q) + B^4 \gamma \varphi^5(\tau;q). \tag{9}$$

Let $\hbar$ denotes a nonzero auxiliary parameter and $H(\tau)$ a nonzero auxiliary function. Then, we construct the zero-order deformation equation

$$(1-q)L[\varphi(\tau;q)] = q\hbar H(\tau) N[\varphi(\tau;q), \Omega(q)], \quad q \in [0,1], \tag{10}$$

such that

$$\varphi(0,q) = 1, \qquad \frac{\partial \varphi(\tau;q)}{\partial \tau}\Big|_{\tau=0} = 0. \tag{11}$$

When $q \in [0,1]$, the solution $\varphi(\tau;q)$ varies from $U_0(\tau)$ to $U(\tau)$ so does $\Omega(q)$ from ω_0 to ω. The Taylor's series with respect to q can be constructed for $\varphi(\tau;q)$ and $\Omega(q)$ and if these two series are convergent at $q = 1$, we have:

$$U(\tau) = U_0(\tau) + \sum_{j=0}^{\infty} U_j(\tau), \quad \omega = \omega_0 + \sum_{j=0}^{\infty} \omega_j, \tag{12}$$

where

$$U_m(\tau) = \frac{\partial^m \varphi(\tau;q)}{m! \partial q^m}\Big|_{q=0}. \tag{13}$$

and

$$\omega_m = \frac{\partial^m \Omega(q)}{m! \partial q^m}\Big|_{q=0}. \tag{14}$$

Differentiating the zero-order deformation Eq. (10) and Eq. (11) m times with respect to embedding parameter q and then dividing them by $m!$ and finally setting $q=0$, we have the so-called mth order deformation equation

$$L\left[U_m(\tau)-\chi_m U_{m-1}(\tau)\right]=\hbar R_m(U_0,\omega_0,...,U_{m-1},\omega_{m-1}), \tag{15}$$

$$U_m(0)=0, \qquad U'_m(0)=0, \quad m\geq 1, \tag{16}$$

where

$$R_m(U_0,\omega_0,...,U_{m-1},\omega_{m-1})=\frac{\partial^{m-1}N\left[\varphi(\tau;q),\Omega(q)\right]}{(m-1)!\partial q^{m-1}}\Big|_{q=0}. \tag{17}$$

Note that U_m,ω_{m-1} are all unknown, but we have only Eq. (15) for U_m, thus an additional algebraic equation is required for determining ω_{m-1}. It is found that the right-hand side of the m^{th} order deformation Eq. (15) is expressed by

$$R_m(U_0,\omega_0,...,U_{m-1},\omega_{m-1})=\sum_{k=0}^{\psi(m)} c_{m,k}(\omega_{m-1})\cos((2k+1)\tau), \tag{18}$$

where $c_{m,k}$ is a coefficient and $\psi(m)$ is a positive integer dependent on order m.

If $R_m(U_0,\omega_0,...,U_{m-1},\omega_{m-1})$ contains the term $\cos\tau$ then the solution of Eq. (15) involves the so-called secular term $\tau\cos\tau$ that this disobeys the rules of solutions expression, thus coefficient $c_{m,0}$ must be enforced to be zero. This provides with the additional algebraic equation for determining ω_{m-1}

$$c_{m,0}(\omega_{m-1})=0. \tag{19}$$

Consequently, we obtain

$$U_m(\tau)=\chi_m U_{m-1}(\tau)+\frac{\hbar}{\omega_0^2}\sum_{j=1}^{\psi(m)}\frac{c_{m,j}(\omega_{m-1})}{1-(2j+1)^2}\cos\left[(2j+1)\tau\right]+C_1\cos\tau+C_2\sin\tau, \tag{20}$$

where C_1,C_2 are two coefficients and to be determined by conditions $U_m(0)=0$ and $U'_m(0)=0$.

Thus the N th order approximation can be given by

$$U(\tau)=U_0(\tau)+\sum_{j=0}^{N}U_j(\tau), \tag{21}$$

and

$$\omega=\omega_0+\sum_{j=0}^{N}\omega_j. \tag{22}$$

3. NUMERICAL RESULTS AND DISCUSSION

For given $\alpha=\beta=\gamma=1$ the amplitude ω_{m-1} can be determined by the analytic approach mentioned above. For $m=1,2$ we have:

$$\begin{cases}\omega_0=\dfrac{1}{\sqrt{10B^4+12B^2+16}},\\ \omega_1=\dfrac{1}{96}\dfrac{B^2\hbar(48+100B^2+65B^6+96B^4)}{\sqrt{10B^4+12B^2+16}(5B^4+6B^2+8)}.\end{cases} \tag{23}$$

Note. The obtained results contain the auxiliary parameter $\hbar$. It is found that convergence regions of the approximation series are dependent upon $\hbar$ [3]. For example, consider cases $B = 0.1, 0.15$. We plotted the $\omega - \hbar$ curve to determine the so-called valid region of $\hbar$, as shown in Fig. 1. Obviously, the valid regions of $\hbar$ for $B = 0.1, 0.15$ are $-4 < \hbar < 4$ and $-3.5 < \hbar < 3.5$, respectively, for instance for $B = 0.1$ we have the result $\omega = 1.003733$ as shown in Table 1.

Also, we consider cases $B = 1, 1.1$. We plotted the $\omega - \hbar$ curve to determine the so-called valid region of $\hbar$ as shown in Fig. 2. It is shown that the valid regions of $\hbar$ for $B = 1, 1.1$ are $-1 < \hbar < 0.9$ and $-0.9 < \hbar < 0.8$, respectively. Furthermore for $B = 1$, we have result $\omega = 1.538669$ as shown in Table 1. In Table 2, we compared the 14th order approximations of HAM with the exact solutions.

Table 1

Approximation of ω for $B = 0.1, 1$ and comparison with exact frequency ω_e

M	$B = 0.1 (\omega_e = 1.003770)$	$B = 1 (\omega_e = 1.523590)$
7	1.003753	1.538663
8	1.003728	1.538669
9	1.003733	1.538669
10	1.003732	1.538695
11	1.003733	1.538669
12	1.003733	1.538669
13	1.003733	1.538669
14	1.003733	1.538669

Table 2

Comparison of the 14 th-order approximations of HAM with the exact solutions

B	HAM	Exact	Error
0.3	1.035516	1.035540	2.32×10^{-5}
0.5	1.107092	1.106540	4.99×10^{-4}
3	7.636706	7.268630	5.06×10^{-2}
5	20.256660	19.181500	5.60×10^{-2}
8	51.078098	48.294600	5.75×10^{-2}
10	79.536112	75.177400	5.79×10^{-2}
20	316.703160	299.223000	5.84×10^{-2}
50	1976.897968	1867.570000	5.85×10^{-2}

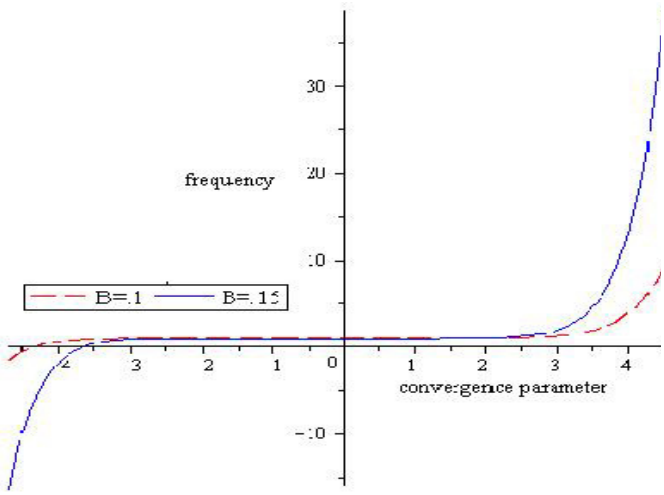

Fig. 1 – The $\omega - \hbar$ curve for $B = 0.1, 0.15$.

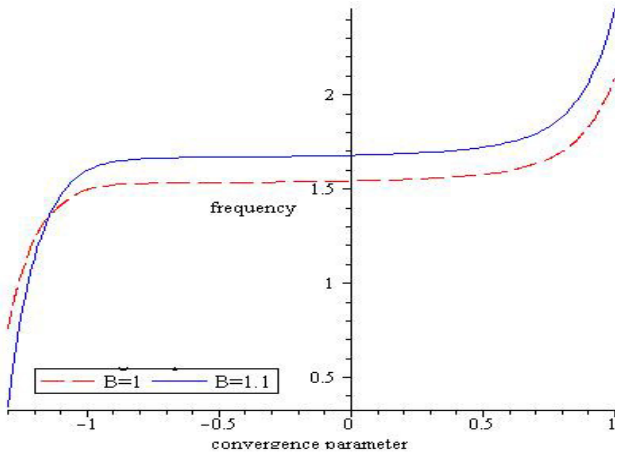

Fig. 2 – The $\omega - \hbar$ curve for $B = 1, 1.1$.

3.1. Square residual error

We obtained the constant $\hbar$ using the least square method. In theory, at the M th-order of approximation, we can define the exact square residual error

$$\Delta_M(\hbar) = \int_D (N(\sum_{k=0}^{M} U_k(\tau), \sum_{k=0}^{M} \omega_k))^2 d\tau. \tag{24}$$

Clearly, the more rapidly $\Delta_M(\hbar)$ decreases to zero, the faster the approximation series converges.

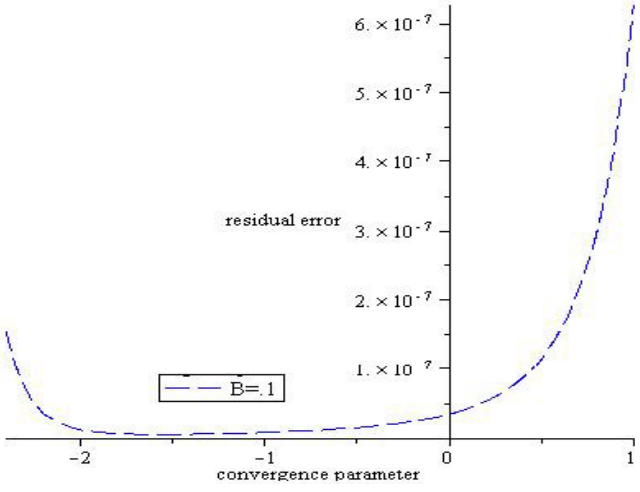

Fig. 3 – The $\Delta_{10}(\hbar)$ - $\hbar$ curve for $B = 0.1$.

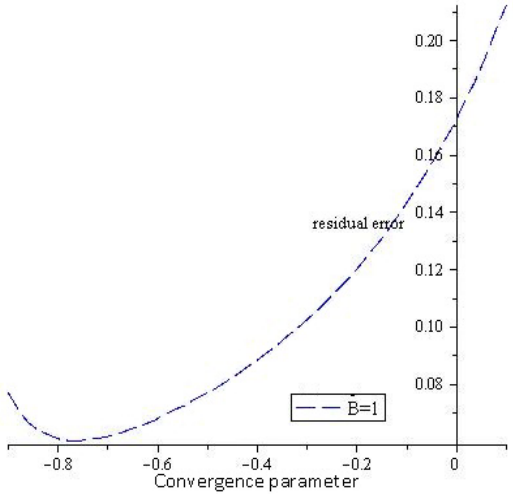

Fig. 4 – The $\Delta_{10}(\hbar) - \hbar$ curve for $B = 1$.

Remark 1. The curve of $\Delta_{10}(\hbar)$ *versus* $\hbar$ at $B = 0.1$ is shown in Fig. 3, which indicates that the optimal values of $\hbar$ is about -1.5.

Remark 2.The curve of $\Delta_{10}(\hbar)$ *versus* $\hbar$ at $B = 1$ is shown in Fig. 4, which indicates that the optimal values of $\hbar$ is about -0.78.

4. HOMOTOPY-PADÉ TECHNIQUE

The Padé technique is widely applied to enlarge the convergence region and convergence rate of given series. The so-called homotopy-Padé technique was suggested by means of combining the Padé technique with HAM.

For a given series

$$S_k(q) = \sum_{j=0}^{k} \omega_j q^j, \tag{25}$$

the corresponding $[n, m]$ Padé approximate is expressed by

$$S_{n+m}(q) = \frac{C_{n,m}(q)}{D_{n,m}(q)} = \frac{\sum_{j=0}^{n} c_j q^j}{1 + \sum_{j=1}^{m} d_j q^j}, \tag{26}$$

where c_j, d_j can be determined by solving the linear system:

$$\begin{cases} \omega_i + \sum_{j=0}^{i-1} \omega_j d_{i-j} = c_i, \ \ i = 0,1,2,...,n, \\ \omega_i + \sum_{j=i-m}^{i-1} \omega_j d_{i-j} = 0, \ \ i = n+1,...,n+m. \end{cases} \tag{27}$$

Setting $q = 1$ provides the $[n,m]$ homotopy-Padé approximation

$$\omega^{[n,m]} = S_{n+m}(1) = \sum_{j=0}^{n+m} \omega_j = \frac{C_{n,m}(1)}{D_{n,m}(1)} = \frac{\sum_{j=0}^{n} c_j}{1 + \sum_{j=1}^{m} d_j}, \tag{28}$$

which accelerate the convergence rate of solution series of HAM. We have applied the homotopy-Padé technique to accelerate the convergence rate of M th-order approximations of HAM. In Table 3 we compared the approximations of homotopy-Padé technique with exact solutions.

Table 3

Comparison the exact solution with approximation of homotopy-Padé technique

	$B = 0.1$	$B = 0.3$	$B = 1$	$B = 3$
$\omega^{[1,1]}/\omega_e$	1.00037	1.00482	1.01757	1.01842
$\omega^{[2,2]}/\omega_e$	1.00015	1.00326	1.01317	1.01674
$\omega^{[3,3]}/\omega_e$	1.00011	1.00232	1.01219	1.01655
$\omega^{[4,4]}/\omega_e$	1.00013	1.00236	1.01087	1.01638
$\omega^{[5,5]}/\omega_e$	1.00010	1.00219	1.01058	1.01550
$\omega^{[6,6]}/\omega_e$	1.00010	1.00168	1.00876	1.01537
$\omega^{[7,7]}/\omega_e$	1.00010	1.00143	1.00781	1.01531

5. CONCLUSIONS

In this paper, the HAM is presented to calculate the frequency and the solution of the nonlinear cubic-quintic Duffing oscillators. According to obtained results, the HAM and homotopy-Padé technique could give efficient frequency approximations for the nonlinear cubic-quintic Duffing oscillators. It is worth mentioning that nonlinear cubic-quintic oscillator models arise in many areas of nonlinear science, e.g., in the study of optical solitons [19]-[20]; thus in nonlinear optics the cubic-quintic Ginzburg-Landau partial differential equation is a generic nonlinear dynamical model describing optical soliton propagation in laser cavities, see, for example, Ref. [21].

REFERENCES

1. Z.-Y. ZHANG, J. ZHONG, S.S. DOU, J. LIU, D. PENG, T. GAO, *A new method to construct traveling wave solutions for the Klein-Gordon-Zakharov equations,* Rom. J. Phys., **58**, pp. 766–777, 2013.
Z.-Y. ZHANG, J. ZHONG, S.S. DOU, J. LIU, D. PENG, T. GAO, *Abundant exact traveling wave solutions for the Klein-Gordon-Zakharov equations via the tanh-coth expansion method and and Jacobi elliptic function expansion method*, Rom. J. Phys., **58**, pp. 749–765, 2013.
2. S.K. LAI, C. W. LAM, B.S. WU, C. WANG, Q.C. ZENG, X.F. HE, *Newton-harmonic balancing approach for accurate solutions to nonlinear cubic-quinitic Duffing oscillators,* Appl. Math. Model., **33**, pp. 852–866, 2008.
3. S.J. LIAO, *Beyond Perturbation*: *Introduction to Homotopy Analysis Method*, Chapman & Hall CRC Press, Boca Raton, 2003.
4. A.H. NAYFEH, *Perturbation method*, New York, John Wiley & Sons, 2000.
5. A.M. LYAPUNOV, *General problem on stability of motion*, London, Taylor & Francis, 1992.

6. A.V. KARMISHIN, AT. ZHUKOV, V.G. KOLOSOV, *Method of dynamics calculation and testing for thin-walled structures* (in Russian), Mashinostroyenie, Moscow, 1990.
7. G. ADOMIAN, *Nonlinear stochastic differential equations*, J. Math. Anal. Appl., **55**, pp. 441–52, 1976.
8. G. ADOMIAN, G.E. ADOMIAN, *A global method for solution complex system*s, Math. Model., **51**, pp. 521–68, 1984.
9. M. GHASEMI, M. FARDI, M. TAVASSOLI KAJANI, R. KHOSHSIAR GHAZIANI, *Numerical solution of fifth order KdV equations by homotopy perturbation method,* Math. Sci. Quarterly J., **2**, pp. 169–181, 2011.
10. M. GHASEMI, A. AZIZI, M. FARDI, *Numerical solution of seven-order Sawada-Kotara equations by homotopy perturbation method*, Math. Scientific J., **1**, pp. 69–77, 2011.
11. S. VAHDATI, Z. ABBAS, M. GHASEMI, Math. *Application of Homotopy Analysis Method to Fredholm and Volterra integral equations* , Sci. Quarterly J., **4**, pp. 267–282, 2010.
12. H. JAFARI, A. GOLBABAI, S. SEIFI, K. SAYEVAND, *Homotopy analysis method for solving multi-term linear and nonlinear diffusion wave equations of fractional order,* Comput. Math. Appl., **59**, pp. 1337–1344, 2010.
13. A. GOLBABAI, M. FARDI, K. SAYEVAND, *Application of the optimal homotopy asymptotic method for solving a strongly nonlinear oscillatory system,* Comput. Math. Model., **58**, pp. 1837–1843, 2013.
14. H. JAFARI, K. SAYEVAND, H. TAJADODI, D. BALEANU, *Homotopy analysis method for solving Abel differential equation of fractional order,* Cent. Eur. J. Phys. Doi: 2013.10.24781, 2013.
15. A. K. GOLMANKHANEH, N.A. PORGHOVEH, D. BALEANU, *Mean square solutions of second-order random differential equations by using homotopy analysis method,* Rom. Rep. Phys., **65**, pp. 350–362, 2013.
16. X.-J. YANG, D. BALEANU, W.-P. ZHONG*, Approximate solutions for diffusion equations on Cantor space-time,* Proc. Romanian. Acad. A, **14**, pp. 127–133, 2013;
    A. JAFARIAN *et al*., *On a one-dimensional coupled system of equations in the theory of thermoelasticity*, Rom. J. Phys., **58**, pp. 694–702, 2013.
17. D. KUMAR, J. SINGH, SUSHILA, *Application of homotopy analysis transform method to fractional biological population model*, Rom. Rep. Phys., **65**, pp. 63–75, 2013;
    A. JAFARIAN *et al*., *Construction of soliton solutions to the Kadomtsev-Petviashvili-II equation using homotopy analysis method*, Rom. Rep. Phys., **65**, pp. 76–83, 2013;
    A.K. GOLMANKHANEH *et al*., *Homotopy perturbation method for solving a system of Schrödinger-Korteweg-de Vries equations*, Rom. Rep. Phys., **63**, pp. 609–623, 2011.
18. S. AL-JABER, *Solution of the radial N-dimensional Schrödinger equation using homotopy perturbation method*, Rom. J. Phys., **58**, pp. 247–259, 2013.
19. Y.V. KARTASHOV *et al*., *Solitons in nonlinear lattices*, Rev. Mod. Phys., **83**, pp. 247–306, 2011;
    D. MIHALACHE, *Linear and nonlinear light bullets: Recent theoretical and experimental studies*, Rom. J. Phys., **57**, pp. 352–371, 2012;
    Y.V. KARTASHOV *et al*., *Generation of surface soliton arrays*, Opt. Lett., **31**, pp. 2329–2331, 2006;
    D. MIHALACHE *et al*., *Stationary walking solitons in bulk quadratic nonlinear media*, Opt. Commun., **137**, pp. 113–117, 1997;
    D. MIHALACHE *et al*., *Multiple-humped bright solitary waves in second-order nonlinear media*, Opt. Eng., **35**, pp. 1616–1623, 1996.
20. H. LEBLOND, D. MIHALACHE, *Models of few optical cycle solitons beyond the slowly varying envelope approximation*, Phys. Reports, **523**, pp. 61–126, 2013;
    H. LEBLOND *et al*., *Theoretical studies of ultrashort-soliton propagation in nonlinear optical media from a general quantum model*, Rom. Rep. Phys., **65**, pp. 925–942, 2013.
21. V. SKARKA *et al*., *Varieties of stable vortical solitons in Ginzburg-Landau media with radially inhomogeneous losses*, Phys. Rev. Lett., **105**, 213901 (2010);
    D. MIHALACHE *et al*., *Collisions between coaxial vortex solitons in the three-dimensional cubic-quintic Ginzburg-Landau equation*, Phys. Rev. A, **77**, 033817, 2008.

Received November 8, 2013

THE PUBLISHING HOUSE
OF THE ROMANIAN ACADEMY

PROCEEDINGS OF THE ROMANIAN ACADEMY, Series A,
Volume 15, Number 3/2014, pp. 235–240

OPTICAL SOLITONS WITH POLYNOMIAL AND TRIPLE-POWER LAW NONLINEARITIES AND SPATIO-TEMPORAL DISPERSION

A. H. BHRAWY [1,2], A. A. ALSHAERY [3], E. M. HILAL [3], Daniela MILOVIC [4], Luminita MORARU [5], Michelle SAVESCU [6,7], Anjan BISWAS [6,1]

[1] King Abdulaziz University, Faculty of Science, Department of Mathematics, Jeddah, Saudi Arabia
[2] Beni-Suef University, Faculty of Science, Department of Mathematics, Beni-Suef, Egypt
[3] King Abdulaziz University, Faculty of Science for Girls, Department of Mathematics, Jeddah, Saudi Arabia
[4] University of Nis, Faculty of Electronic Engineering Department of Telecommunications, Aleksandra Medvedeva 14, 18000 Nis, Serbia
[5] "Dunarea de Jos" University Galaţi, Physics and Environment, Department of Chemistry, 111 Domneasca Street, 800201 Galati, Romania
[6] Delaware State University, Department of Mathematical Sciences, Dover, DE 19901-2277, USA
[7] Kuztown University of Pennsylvania, Department of Mathematics, 15200 Kutztown Road, Kuztown, PA-19530, USA
E-mail: biswas.anjan@gmail.com

This paper obtains exact traveling wave solutions to the nonlinear Schrödinger's equation that is considered with spatio-temporal dispersion in addition to group-velocity dispersion. The two types of nonlinearity associated with this equation are polynomial and triple-power law. The obtained optical soliton solutions are in terms of elliptic function of third kind.

Key words: spatio-temporal dispersion, integrability, optical solitons.

1. INTRODUCTION

The theory of optical solitons is one of the most progressive areas of research in applied and theoretical physics [1-32]. This research has lead to several overwhelming and interesting results. The most commonly studied aspects of optical solitons are conservation laws, birefringent fibers, dense wavelength-division multiplexing (DWDM) systems, polarization mode dispersion, Thirring solitons, cascaded systems, timing, frequency and amplitude jitter, four-wave mixing, and several other aspects. The governing equation is the nonlinear Schrödinger's equation (NLSE) that contains the nonlinear term and the group velocity dispersion (GVD), besides the linear evolution term. It is the delicate balance between GVD and nonlinearity that results in the formation of optical solitons. These temporal optical solitons propagate along trans-continental and trans-oceanic distances along the optical fibers.

It was very recently pointed out that NLSE with only GVD and nonlinearity is an ill-posed model [4, 7]. The inclusion of spatio-temporal dispersion (STD) was suggested in 2012 in order to make NLSE a well posed model [7]. This paper will therefore address NLSE with GVD and STD terms included. The types of nonlinearity that will be studied in this paper are polynomial law as well as triple-power law. It must be noted that the cases of Kerr law, power law, parabolic law, dual-power law as well as the log law nonlinearity are already studied with the so called "improved" NLSE [9]. Also, the cases of polynomial law and triple-power law nonlinearity of NLSE with just GVD, without STD, was studied in 2009 [2]. Additionally in Ref. [2] this problem was studied with only GVD, and the GVD coefficient was a particular constant, namely 1/2. However, this paper will study with GVD and STD, both with arbitrary real-valued coefficients. Therefore, the results of this paper will match the results obtained earlier for special choice of the parameters and the coefficients of the evolution equation. The *traveling wave hypothesis* will be the integration tool that will be adopted here.

2. DYNAMICAL MODEL

In non-Kerr law media, the dynamics of soliton propagation for long distances is governed by dimensionless NLSE with GVD and STD as follows

$$iq_t + aq_{xx} + bq_{xt} + F(|q|^2)\ \ q = 0, \tag{1}$$

where $q(x,t)$ represents the complex-valued wave profile. Here x and t represent spatial and temporal variables, respectively. The coefficients a and b are GVD and STD, respectively. The first term is the linear evolution of the pulses in nonlinear optical fibers. The last term represents non-Kerr law nonlinearity. Here, $F(|q|^2)q : C \to C$. If the complex plane C is a two-dimensional linear space R^2, $F(|q|^2)q$ is k times continuously differentiable, then

$$F(|q|^2)q \in \bigcup_{m,n-1}^{\infty} C^k\left((-n,\ n)\times(-m,\ m); R^2\right).$$

The current trend is to study the dynamics of solitons with GVD and nonlinearity. The STD term is newly proposed so that equation (1) is a well-posed problem [7]. Solitons are the outcome of a delicate balance between nonlinearity and dispersion, in this case between GVD and STD. In this paper we will integrate equation (1) by traveling wave hypothesis for two forms of nonlinear optical media. They are polynomial law nonlinearity and triple-power law nonlinearity.

In order to integrate (1), the traveling wave hypothesis given by [2, 9]

$$q(x,t) = g(s)\mathrm{e}^{\mathrm{i}\phi(x,\ t)} \tag{2}$$

is selected. Here

$$s = x - vt, \tag{3}$$

where v is the speed of the soliton and the phase is

$$\phi(x,\ t) = -\kappa x + \omega t + \theta. \tag{4}$$

The frequency is denoted by κ while the wave number of the soliton is denoted by ω. Substituting (2) into (1) and decomposing into real and imaginary parts leads to

$$v = \frac{\omega b - 2a\kappa}{1 - b\kappa} \tag{5}$$

$$(a - bv)g'' = (\omega + a\kappa^2 - b\omega\kappa)g - F(g^2)g \tag{6}$$

respectively. Here the notations $g' = \mathrm{d}g/\mathrm{d}s$ and $g'' = \mathrm{d}^2 g/\mathrm{d}s^2$ are introduced. Thus, the imaginary part leads to the speed of the soliton irrespective of the type of nonlinearity in question. Multiplying both sides of (6) by g' and integrating leads to

$$(a - bv)(g')^2 = (\omega + a\kappa^2 - b\omega\kappa)g^2 - 2\int_g F(h^2)hh'\mathrm{d}h \tag{7}$$

after choosing integration constant to be zero, since the search is for a localized soliton solution. Next, separating variables and integrating leads to

$$x - vt = \int \frac{\sqrt{a - bv}\mathrm{d}g}{\left[(\omega + a\kappa^2 - b\omega\kappa)g^2 - 2\int_g F(h^2)hh'\mathrm{d}h\right]^{1/2}}. \tag{8}$$

Equation (8) will now be separately analyzed for the two laws of nonlinearity in the next two subsections.

2.1. Polynomial law nonlinearity

Polynomial law nonlinearity is an extension of parabolic law nonlinearity. Therefore this type of nonlinear optical medium takes the form

$$F(s) = k_1 s + k_2 s^2 + k_3 s^3 \tag{9}$$

so that the NLSE (1) transforms to

$$iq_t + aq_{xx} + bq_{xt} + (k_1|q|^2 + k_2|q|^4 + k_3|q|^6)q = 0\,. \tag{10}$$

Equation (8) therefore reduces to

$$x - vt = \int \frac{2\sqrt{3(a-bv)}\,dg}{g\sqrt{12(\omega + a\kappa^2 - b\omega\kappa) - g^2(6k_1 + 4k_2 g^2 + 3k_3 g^4)}}\,. \tag{11}$$

Performing the integration in (11) gives the implicit solution

$$\begin{aligned} &\frac{x-vt}{2\sqrt{3(a-bv)}}\, g_3\sqrt{12a\kappa^2 - 6g^2k_1 - 4g^4k_2 - 3g^6k_3 + 12\omega(1-b\kappa)} = \\ &= -\prod\left(1 - \frac{g_2}{g_3};\ \sin^{-1}\sqrt{\frac{g^2 - g_3}{g_2 - g_3}},\ \frac{g_2 - g_3}{g_1 - g_3}\right)\sqrt{\frac{(g^2 - g_1)(g^2 - g_2)(g^2 - g_3)}{g_1 - g_3}}, \end{aligned} \tag{12}$$

where Π is the incomplete elliptic integral of third kind that is defined as

$$\prod(n;\phi,\alpha) = \int_0^{\phi} \frac{\mathrm{d}\theta}{(a - n\sin^2\theta)\sqrt{1 - \sin^2\alpha\sin^2\theta}}. \tag{13}$$

Here

$$g_1 = \frac{1}{9k_3}\left[4k_2 - \frac{2(8k_2^2 - 27k_1k_3)}{(2R_1)^{1/3}} - (2R_1)^{1/3}\right], \tag{14}$$

$$g_2 = -\frac{1}{9k_3}\left[4k_2 + (8k_2^2 - 27k_1k_3)\left(-\frac{4}{R_1}\right)^{1/3} + \left(-\frac{R_1}{4}\right)^{1/3}\left(1 - \mathrm{i}\sqrt{3}\right)\right], \tag{15}$$

$$g_3 = -\frac{1}{9k_3}\left[4k_2 - (8k_2^2 - 27k_1k_3)\left(-\frac{4}{R_1}\right)^{1/3} + \left(-\frac{R_1}{4}\right)^{1/3}\left(1 + \mathrm{i}\sqrt{3}\right)\right], \tag{16}$$

and

$$R_1 = r_1 + \frac{1}{2}\left[\left(-16k_2^2 + 54k_1k_3\right)^3 + 4r_1\right]^{1/2}, \tag{17}$$

with

$$r_1 = -32k_2^3 + 162k_1k_2k_3 + 729k_3^2\left[a\kappa^2 + \omega(1 - b\kappa)\right]. \tag{18}$$

Thus, relation (18) prompts the constraint condition

$$\left(-16k_2^2 + 54k_1k_3\right)^3 + 4r_1 > 0 \tag{19}$$

in order for the solution to exist.

2.2. Triple-power law nonlinearity

This is a generalization of polynomial law nonlinearity and an extension of dual-power law nonlinearity. In this case,

$$F(s) = k_4 s^n + k_5 s^{2n} + k_6 s^{3n} \tag{20}$$

so that the NLSE (1) transforms to

$$iq_t + aq_{xx} + bq_{xt} + (k_4 |q|^{2n} + k_5 |q|^{4n} + k_6 |q|^{6n}) \quad q = 0 . \tag{21}$$

Equation (8) therefore reduces to

$$x - vt = \sqrt{(n+1)(2n+1)(3n+1)(a-bv)} \int \frac{\mathrm{d}\, g}{g\sqrt{G(g)}} . \tag{22}$$

Here

$$\begin{aligned} G(g) &= (n+1)(2n+1)(3n+1)(\omega + a\kappa^2 - \omega b\kappa) - \\ &- \left[(2n+1)(3n+1)k_4 g^{2n} + (n+1)(3n+1)k_5 g^{4n} + (n+1)(2n+1)k_6 g^{6n}\right]. \end{aligned} \tag{23}$$

Performing the integration in (22) leads to the solution

$$\begin{aligned} &\frac{x - vt}{\sqrt{(n+1)(2n+1)(3n+1)(a-bv)}} g_3 n\sqrt{P} = \\ &= -\prod\left(1 - \frac{g_5}{g_6};\ \sin^{-1}\sqrt{\frac{g^{2n} - g_6}{g_5 - g_6}},\ \frac{g_5 - g_6}{g_4 - g_6}\right)\sqrt{\frac{(g^{2n} - g_4)(g^{2n} - g_5)(g^{2n} - g_6)}{g_4 - g_6}}. \end{aligned} \tag{24}$$

Here

$$\begin{aligned} P &= (n+1)(2n+1)(3n+1)[a\kappa^2 + \omega(1 - b\kappa)] - \\ &- \left[(2n+1)(3n+1)k_4 g^{2n} - [(n+1)(3n+1)]k_5 g^{4n} - (n+1)(2n+1)k_6 g^{6n}\right]. \end{aligned} \tag{25}$$

Also,

$$\begin{aligned} g_4 &= \frac{1}{3k_6(n+1)(2n+1)}\left\{-k_5(n+1)(3n+1) + \right. \\ &\left. + (n+1)(3n+1)\left(\frac{2}{R_2}\right)^{1/3}\left[k_5^2(n+1)(3n+1) - 3k_4k_6(2n+1)^2\right] + \left(\frac{R_2}{2}\right)^{1/3}\right\}, \end{aligned} \tag{26}$$

$$\begin{aligned} g_5 &= \frac{1}{3k_6(n+1)(2n+1)}\left\{-k_5(n+1)(3n+1) - \right. \\ &\left. - (n+1)(3n+1)(1+\mathrm{i}\sqrt{3})\left(\frac{1}{4R_2}\right)^{1/3}\left[k_5^2(n+1)(3n+1) - 3k_4k_6(2n+1)^2\right] + (-1+\mathrm{i}\sqrt{3})\left(\frac{R_2}{16}\right)^{1/3}\right\}, \end{aligned} \tag{27}$$

$$\begin{aligned} g_6 &= \frac{1}{3k_6(n+1)(2n+1)}\left\{k_5(n+1)(3n+1) + \right. \\ &\left. + (n+1)(3n+1)(1-\mathrm{i}\sqrt{3})\left(\frac{1}{4R_2}\right)^{1/3}\left[k_5^2(n+1)(3n+1) - 3k_4k_6(2n+1)^2\right] + (1+\mathrm{i}\sqrt{3})\left(\frac{R_2}{16}\right)^{1/3}\right\}, \end{aligned} \tag{28}$$

and

$$
\begin{aligned}
R_2 &= -2k_5^3(n+1)^3(3n+1)^3 + 9k_4k_5k_6(1+6n+11n^2+6n^3)^2 + \\
&+27k_6^2(n+1)^3(2n+1)^3(3n+1)[a\kappa^2+\omega(1-b\kappa)] + \\
&+[(n+1)^3(3n+1)^3[(n+1)\{27k_6^2(n+1)(2n+1)^3[a\kappa^2+\omega(1-b\kappa)]+9k_4k_5k_6(2n+1)^2(3n+1)- \\
&-2k_5^3(n+1)(3n+1)^2]^2\}+4(3n+1)\{3k_4k_6(2n+1)^2-k_5^2(n+1)^3(3n+1)^3]^{1/2}.
\end{aligned}
\tag{29}
$$

The relation for R_2 given by (29) prompts the constraint condition

$$
\begin{aligned}
&(n+1)^4(3n+1)[27k_6^2(n+1)(2n+1)^3[a\kappa^2+\omega(1-b\kappa)]+9k_4k_5k_6(2n+1)^2(3n+1)- \\
&-2k_5^3(n+1)(3n+1)^2]^2+4\{3k_4k_6(2n+1)^2-k_5^2(n+1)^3(3n+1)^3\}>0,
\end{aligned}
\tag{30}
$$

that must remain valid in order for the soliton solution to exist.

3. CONCLUSIONS

This paper studied optical solitons with polynomial and triple-power law nonlinearity. The traveling wave hypothesis revealed exact solutions that are in terms of incomplete elliptic functions of third kind. These exact solutions, which are rather complicated ones, are however important in nonlinear optics studies. One can easily employ these solutions to address several important aspects of optical solitons that were enumerated in introduction. The inclusion of perturbation terms such as inter-modal dispersion, multi-photon absorption, and several others will give an additional flavor to this research area. Those results, along with several other interesting aspects will be reported elsewhere.

ACKNOWLEDGMENTS

This work was funded by the Deanship of Scientific Research (DSR), King Abdulaziz University, under grant No. (14-130/1433 HiCi). The authors, therefore, acknowledge technical and financial support of KAU.

REFERENCES

1. A. BISWAS, S. KONAR, *Introduction to non-Kerr law optical solitons,* CRC Press Boca Raton, FL., USA, 2006.
2. A. BISWAS, D. MILOVIC, *Traveling wave solutions of the nonlinear Schrödinger's equation in non-Kerr law media*, Communications in Nonlinear Science and Numerical Simulation, **15**, pp. 1993–1998, 2009.
3. A. S. FOKAS, *On a class of physically important integral equations*, Physica D, **87**, pp. 145–150, 1995.
4. X. GENG, Y. LV, *Darboux transformation for an integrable generalization of the nonlinear Schrödinger equation*, Nonlinear Dynamics, **69**, pp. 1621–1630, 2012.
5. H. LEBLOND, H. TRIKI, D. MIHALACHE, *Theoretical studies of ultrashort-soliton propagation in nonlinear optical media from a general quantum model*, Romanian Reports in Physics, **65**, pp. 925–942, 2013.
6. H. LEBLOND, D. MIHALACHE, *Models of few optical cycle solitons beyond the slowly varying envelope approximation*, Physics Reports, **523**, pp. 61–126, 2013.
7. S. KUMAR, K. SINGH, R. K. GUPTA, *Coupled Higgs field equation and Hamiltonian amplitude equation: Lie classical approach and G'/G- expansion method*, Pramana, **79**, pp. 41–60, 2012.
8. L. LENELLS, A. S. FOKAS, *Dressing for a novel integrable generalization of the nonlinear Schrödinger's equation*, J. Nonlinear Sci., **20**, pp. 709–722, 2010.
9. M. SAVESCU, K. R. KHAN, P. NARUKA, H. JAFARI, L. MORARU, A. BISWAS, *Optical solitons in photonic nanowaveguides with an improved nonlinear Schrödinger's equation*, Journal of Computational and Theoretical Nanoscience, **10**, pp. 1182–1191, 2013.
10. M. WADATI, H. SEGUR, M. J. ABLOWITZ, *A new Hamiltonian amplitude equation governing modulated wave instabilities*, Journal of the Physical Society of Japan, **61**, pp. 1187–1193, 1992.
11. H. TRIKI, S.CRUTCHER, A. YILDIRIM, T. HAYAT, O. M. ALDOSSARY, A. BISWAS, *Bright and dark solitons of the modified complex Ginzburg-Landau equation with parabolic and dual-power law nonlinearity*, Romanian Reports in Physics, **64**, pp. 367–380, 2012.
12. G. EBADI, A.YILDIRIM, A. BISWAS, *Chiral solitons with Bohm potential using G'/G method and exp-function method*, Romanian Reports in Physics, **64**, pp. 357–366, 2012.

13. L. GIRGIS, D. MILOVIC, S. KONAR, A. YILDIRIM, H. JAFARI, A. BISWAS, *Optical gaussons in birefringent fibers and DWDM systems with inter-modal dispersion*, Romanian Reports in Physics, **64**, pp. 663–671, 2012.
14. H. TRIKI, A. YILDIRIM, T. HAYAT, O. M. ALDOSSARY, A. BISWAS, *Topological and non-topological solitons of a generalized derivative nonlinear Schrödinger's equation with perturbation terms*, Romanian Reports in Physics, **64**, pp. 672–684, 2012.
15. A. H. BHRAWY, M. A. ABDELKAWY, S. KUMAR, A. BISWAS, *Solitons and other solutions to Kadomtsev-Petviashvili equation of B-type*, Romanian Journal of Physics, **58**, pp. 729–748, 2013.
16. B. S. AHMED, A. BISWAS, E. V. KRISHNAN, S. KUMAR, *Solitons and other solutions to the generalized Maccari system*, Romanian Reports in Physics, **65**, pp. 1138–1154, 2013.
17. A. G. JOHNPILLAI, A.YILDIRIM, A. BISWAS, *Chiral solitons with Bohm potential by Lie group analysis and traveling wave hypothesis*, Romanian Journal of Physics, **57**, pp. 545–554, 2012.
18. H. TRIKI, A. YILDIRIM, T. HAYAT, O. M. ALDOSSARY, A. BISWAS, *Shock wave solution of the Benney-Luke equation*, Romanian Journal of Physics, **57**, pp. 1029–1034, 2012.
19. G. EBADI, N. YOUSEFZADEH, H. TRIKI, A. YILDIRIM, A. BISWAS, *Envelope solitons, periodic waves and other solutions to Boussinesq-Burgers equation*, Romanian Reports in Physics, **64**, pp. 915–932, 2012.
20. G. EBADI, A. MOJAVER, H. TRIKI, A. YILDIRIM, A. BISWAS, *Topological solitons and other solutions of the Rosenau-KdV equation with power law nonlinearity*, Romanian Journal of Physics, **58**, pp. 3–14, 2013.
21. A. H. KARA, H. TRIKI, A. BISWAS, *Conservation laws of the Bretherton equation*, Applied Mathematics and Information Sciences, **7**, pp. 877–879, 2013.
22. A. BISWAS, S. KUMAR, E. V. KRISHNAN, B. AHMED, A. STRONG, S. JOHNSON, A. YILDIRIM, *Topological solitons and other solutions to potential KdV equation,* Romanian Reports in Physics, **65**, pp. 1125–1137, 2013.
23. S. CRUTCHER, A. OSEO, A. YILDIRIM, A. BISWAS, *Oscillatory parabolic law optical spatial solitons*, Journal of Optoelectronics and Advanced Materials, **14**, pp. 29–40, 2012.
24. A. BISWAS, K. KHAN, A. RAHMAN, A.YILDIRIM, T. HAYAT, O. M. ALDOSSARY, *Bright and dark optical solitons in birefringent fibers with Hamiltonian perturbations and Kerr law nonlinearity*, Journal of Optoelectronics and Advanced Materials, **14**, pp. 571–576, 2012.
25. L. CHERBI, A. BELLALIA, M. UTHMAN, A. BISWAS, *Modeling of two rings-photonic crystal fibers with the scalar finite element method*, Journal of Optoelectronics and Advanced Materials, **15**, pp. 1385–1391, 2013.
26. B. AHMED, A. BISWAS, *Solitons, kinks and singular solitons of coupled Korteweg-de Vries equation*, Proc. Romanian Acad. A, **14**, pp. 111–120, 2013.
27. A. BISWAS, A. YILDIRIM, O. M. ALDOSSARY, R. SASSAMAN, *Soliton perturbation theory for the generalized Klein Gordon equation with full nonlinearity*, Proc. Romanian Acad. A, **13**, pp. 32–41, 2012.
28. G. EBADI, A. H. KARA, M. D. PETKOVIC, A. YILDIRIM, A. BISWAS, *Solitons and conserved quantities of the Ito equation*, Proc. Romanian Acad. A, **13**, pp. 215–224, 2012.
29. D. MIHALACHE, *Linear and nonlinear light bullets: Recent theoretical and experimental studies*, Romanian Journal of Physics, **57**, pp. 352–371, 2012.
30. G. YANG et al., *Control of high power pulses extracted from the maximally compressed pulse in a nonlinear optical fiber*, Romanian Reports in Physics, **65**, pp. 902–914, 2013.
31. G. YANG *et al*., *High power pulses extracted from the Peregrine rogue wave*, Romanian Reports in Physics, **65**, pp. 391–400, 2013.
32. A. M. WAZWAZ, *Multiple soliton solution for two integrable couplings of the modified Korteweg-de Vries equation*, Proc. Romanian Acad. A, **14**, pp. 219–225, 2013.

Received December 16, 2013

THE PUBLISHING HOUSE
OF THE ROMANIAN ACADEMY

PROCEEDINGS OF THE ROMANIAN ACADEMY, Series A,
Volume 15, Number 3/2014, pp. 241–246

MULTIPLE KINK SOLUTIONS FOR THE (2+1)-DIMENSIONAL INTEGRABLE GARDNER EQUATION

Abdul-Majid WAZWAZ

Saint Xavier University, Department of Mathematics, Chicago, IL 60655, USA
E-mail: wazwaz@sxu.edu

In this work we study the (2+1)-dimensional integrable Gardner equation. The simplified form of Hirota's direct method is used to derive multiple kink solutions and multiple singular kink solutions for this equation.

Key words: (2+1)-dimensional Gardner equation; Hirota bilinear method; multiple kink solutions.

1. INTRODUCTION

The (1+1)-dimensional Gardner equation reads

$$u_t + 6\beta u u_x + u_{xxx} - \frac{3}{2}\alpha^2 u^2 u_x = 0, \tag{1}$$

that combines the Korteweg-de Vries (KdV) equation and the modified KdV (mKdV) equation. For $\alpha = 0$, Eq. (1) reduces to the KdV equation, whereas for $\beta = 0$ it reduces to the mKdV equation. The KdV equation was complemented with a higher-order cubic nonlinear term of the form $u^2 u_x$ to obtain the Gardner equation (1), which is completely integrable like the KdV equation and the mKdV equation. The function $u(x,t)$ is the amplitude of the relevant wave mode. Gardner equation is widely used in various branches of physics, such as plasma physics, fluid physics, and quantum field theory [1–7]. It also describes a variety of wave phenomena in plasma and solid state physics [5, 6].

Kadomtsov and Petviashivilli [7] extended the KdV equation to obtain the Kadomtsov–Petviashivilli (KP) equation

$$(u_t + 6uu_x + u_{xxx})_x + u_{yy} = 0. \tag{2}$$

Kadomtsov and Petviashivilli [7] relaxed the restriction that the waves be strictly one dimensional, namely the *x*-direction of the KdV equation, to derive the completely integrable KP equation (2). The KP equation describes the evolution of quasi-one dimensional shallow-water waves when effects of the surface tension and the viscosity are negligible. However, Wazwaz [6] used the sense of Kadomtsov and Petviashivilli of the relaxation of the restriction that the waves be strictly one dimensional in the Gardner equation, and introduced the Gardner-KP equation given by

$$(u_t + 6uu_x + 6u^2 u_x + u_{xxx})_x + u_{yy} = 0. \tag{3}$$

The Gardner-KP equation was proved to be integrable. The Lie symmetries, conservation laws, reductions, and exact solutions via generalized double reduction theorem are computed for the Gardner-KP equation in [8]. However, in [9], the bifurcation concept was used to handle (3) and explicit parameter expressions of all types of bounded traveling wave solutions were derived.

In [2, 3], the (2+1)-dimensional Gardner equation was proposed in the integro-differential form

$$u_t + 6\beta u u_x + u_{xxx} - \frac{3}{2}\alpha^2 u^2 u_x + 3\sigma^2 \partial_x^{-1} u_{yy} - 3\alpha\sigma u_x \partial_x^{-1} u_y = 0, \tag{4}$$

where $\sigma^2 = \pm 1$, α and β are arbitrary constants, and ∂_x^{-1} is the inverse of ∂_x with $\partial_x \partial_x^{-1} = \partial_x^{-1} \partial_x = 1$. The (2+1)-dimensional Gardner equation (4) was examined in [2,3] by using the inverse scattering theorem and proved to be a completely integrable equation. In [4], the authors presented the Casorati and Grammian determinant solutions to the (2+1)-dimensional Gardner equation (4). In [1–3], it was stated that the (2+1)-dimensional Gardner equation (4) has amazing properties that in appropriate limits it reduces to the KdV equation, mKdV equation, the Gardner equation, KP equation, and the modified KP (mKP) equation. For example for $\alpha = 0$, this equation reduces to the KP equation. For $\beta = 0$, it reduces to the mKP equation. For $\alpha = 0$ and $\sigma = 0$ it becomes the KdV equation [1–3]. For $\beta = 0$ and $\sigma = 0$ it becomes the mKdV equation. For $\sigma = 0$, the (2+1)-dimensional Gardner equation becomes the (1+1)-dimensional Gardner equation. We recall here that all the aforementioned equations are integrable.

The Lax pair [1]–[3] for the (2+1)-dimensional Gardner equation (4) is given by

$$\sigma\psi_y + \psi_{xx} + \alpha u \psi_x + \beta u \psi = 0, \tag{5}$$

$$\begin{aligned} \psi_t + 4\psi_{xxx} + \alpha u \psi_{xx} + (3\alpha u_x + \frac{3}{2}\alpha^2 u^2 + 6\beta u - 3\alpha\sigma\partial_x^{-1} u_y)\psi_x + \\ + (3\beta u_x + \frac{3}{2}\alpha^2 \beta u^2 + 3\beta\sigma\partial_x^{-1} u_y)\psi = 0. \end{aligned} \tag{6}$$

The compatibility condition [1] between (5) and (6) gives the (2+1)-dimensional Gardner equation (4). Many kinds of solitons occur for this equation, including pulse-type solitons, positive and negative solitons, and kinks and table-top solitons [1].

Studies of various physical structures of nonlinear equations had attracted much attention in connection with the important problems that arise in scientific applications [10–23]. Many powerful methods, such the Bäcklund transformation method, Darboux transformation, Pfaffian technique, the inverse scattering method, the Painlevé analysis, and the generalized symmetry method are commonly used to integrate nonlinear evolution equations. The Hirota's bilinear method [10] and the simplified Hirota method [13], are rather heuristic and the most commonly used. These approaches possess powerful features that make them practical for the determination of multiple soliton solutions for a wide class of nonlinear evolution equations. The computer symbolic systems such as Maple and Mathematica allow us to perform complicated and tedious calculations.

It is the aim of this work to focus on deriving multiple kink solitons and multiple singular kink solutions for the (2+1)-dimensional Gardner equation (4). The constraint condition for the existence of multiple kink solutions will be established. The simplified Hirota's method, developed by Hereman-Nuseir [13] will be employed to achieve this goal.

2. MULTIPLE KINK SOLUTIONS

In this section, we will derive multiple kink solutions for the (2+1)-dimensional Gardner equation

$$u_t + 6\beta u u_x + u_{xxx} - \frac{3}{2}\alpha^2 u^2 u_x + 3\sigma^2 \partial_x^{-1} u_{yy} - 3\alpha\sigma\partial_x^{-1} u_y = 0, \tag{7}$$

where ∂_x^{-1} is the inverse of ∂_x with $\partial_x \partial_x^{-1} = \partial_x^{-1} \partial_x = 1$, and

$$(\partial_x^{-1} f)(x) = \int_{-\infty}^{x} f(t)\mathrm{d}t, \tag{8}$$

under the decaying condition at infinity.

To get rid of the inverse operator, we use the potential transformation

$$u(x, y, t) = v_x(x, y, t), \tag{9}$$

that carries (7) to the potential form

$$v_{xt} + 6\beta v_x v_{xx} + v_{xxxx} - \frac{3}{2}\alpha^2 v_x^2 v_{xx} + 3\sigma^2 v_{yy} - 3\alpha\sigma v_{xx} v_y = 0. \tag{10}$$

To determine the dispersion relation c_i, we substitute

$$v(x,y,t)=\mathrm{e}^{k_i x+r_i y-c_i t}, \tag{11}$$

into the linear terms of (10); we obtain the dispersion relation

$$c_i=k_i^3+\frac{3\sigma^2 r_i^2}{k_i}, \tag{12}$$

and hence we set the dispersion variable as

$$\theta_i=k_i x+r_i y-(k_i^3+\frac{3\sigma^2 r_i^2}{k_i})t. \tag{13}$$

The multi-kink solutions of (7), using the Cole-Hopf transformation, are assumed to be

$$u(x,y,t)=R\left(\ln f(x,y,t)\right)_x, \tag{14}$$

and therefore

$$v(x,y,t)=R\left(\ln f(x,y,t)\right). \tag{15}$$

The simplified Hirota's method admits the use of the auxiliary function $f(x,y,t)$ for the single kink solution by

$$f(x,y,t)=1+\mathrm{e}^{k_1 x+r_1 y-(k_1^3+\frac{3\sigma^2 r_1^2}{k_1})t}. \tag{16}$$

Substituting (15) into (10) and solving for R we find

$$R=\frac{2}{\alpha}, \tag{17}$$

and the kink solutions exist if the coefficients r_i satisfy the constraint condition

$$r_i=\frac{k_i(2\beta-\alpha k_i)}{\sigma\alpha}, \quad i=1,2,\cdots,N. \tag{18}$$

Based on this result, the dispersion relation (12) becomes

$$c_i=\frac{4k_i(\alpha^2 k_i^2-3\alpha\beta k_i+3\beta^2)}{\alpha^2}, \quad i=1,2,\cdots,N. \tag{19}$$

Using the potential (9) gives the single kink solution

$$u(x,y,t)=\frac{2k_1\mathrm{e}^{k_1 x+\frac{k_1(2\beta-\alpha k_1)}{\sigma\alpha}y-\left(\frac{4k_i(\alpha^2 k_1^2-3\alpha\beta k_1+3\beta^2)}{\alpha^2}\right)t}}{\alpha\left(1+\mathrm{e}^{k_1 x+\frac{k_1(2\beta-\alpha k_1)}{\sigma\alpha}y-\left(\frac{4k_1(\alpha^2 k_1^2-3\alpha\beta k_1+3\beta^2)}{\alpha^2}\right)t}\right)}. \tag{20}$$

For the two kink solutions we set

$$f(x,y,t)=1+\mathrm{e}^{\theta_1}+\mathrm{e}^{\theta_2}. \tag{21}$$

Substituting these results into (15) we find the two kink solutions given by

$$u(x,y,t)=\frac{2\sum_{i=1}^{2}k_i\mathrm{e}^{k_i x+\frac{k_i(2\beta-\alpha k_i)}{\sigma\alpha}y-\left(\frac{4k_i(\alpha^2 k_i^2-3\alpha\beta k_i+3\beta^2)}{\alpha^2}\right)t}}{\alpha\left(1+\sum_{i=1}^{2}\mathrm{e}^{k_i x+\frac{k_i(2\beta-\alpha k_i)}{\sigma\alpha}y-\left(\frac{4k_i(\alpha^2 k_i^2-3\alpha\beta k_i+3\beta^2)}{\alpha^2}\right)t}\right)}. \tag{22}$$

For the three kink solutions, we set

$$f(x,y,t)=1+\mathrm{e}^{\theta_1}+\mathrm{e}^{\theta_2}+\mathrm{e}^{\theta_3}. \tag{23}$$

Proceeding as before, we find the three kink solutions given by

$$u(x,y,t)=\frac{2\sum_{i=1}^{3}k_i\,\mathrm{e}^{k_ix+\frac{k_i(2\beta-\alpha k_i)}{\sigma\alpha}y-\left(\frac{4k_i(\alpha^2k_i^2-3\alpha\beta k_i+3\beta^2)}{\alpha^2}\right)t}}{\alpha\left(1+\sum_{i=1}^{3}\mathrm{e}^{k_ix+\frac{k_i(2\beta-\alpha k_i)}{\sigma\alpha}y-\left(\frac{4k_i(\alpha^2k_i^2-3\alpha\beta k_i+3\beta^2)}{\alpha^2}\right)t}\right)}. \tag{24}$$

This shows that the (2+1)-dimensional Gardner equation (7) gives *N*-kink solutions for finite N, where $N\geq 1$. Based on the obtained results, the general *N*-kink solutions can be set in the form

$$u(x,y,t)=\frac{2\sum_{i=1}^{N}k_i\,\mathrm{e}^{k_ix+\frac{k_i(2\beta-\alpha k_i)}{\sigma\alpha}y-\left(\frac{4k_i(\alpha^2k_i^2-3\alpha\beta k_i+3\beta^2)}{\alpha^2}\right)t}}{\alpha\left(1+\sum_{i=1}^{N}\mathrm{e}^{k_ix+\frac{k_i(2\beta-\alpha k_i)}{\sigma\alpha}y-\left(\frac{4k_i(\alpha^2k_i^2-3\alpha\beta k_i+3\beta^2)}{\alpha^2}\right)t}\right)}. \tag{25}$$

3. MULTIPLE SINGULAR KINK SOLUTIONS

We will next derive multiple singular kink solutions for the (2+1)-dimensional Gardner equation

$$u_t+6\beta uu_x+u_{xxx}-\frac{3}{2}\alpha^2u^2u_x+3\sigma^2\partial_x^{-1}u_{yy}-3\alpha\sigma\partial_x^{-1}u_y=0, \tag{26}$$

that becomes

$$v_{xt}+6\beta v_xv_{xx}+v_{xxxx}-\frac{3}{2}\alpha^2v_x^2v_{xx}+3\sigma^2v_{yy}-3\alpha\sigma v_{xx}v_y=0, \tag{27}$$

upon using the potential

$$u(x,y,t)=v_x(x,y,t). \tag{28}$$

The dispersion relation c_i, the dispersion variables, the coefficient R, and the constraint condition for the coefficients r_i remain the same, given by

$$c_i=k_i^3+\frac{3\sigma^2r_i^2}{k_i}, \tag{29}$$

$$\theta_i=k_ix+r_iy-(k_i^3+\frac{3\sigma^2r_i^2}{k_i})t, \tag{30}$$

$$R=\frac{2}{\alpha}, \tag{31}$$

and

$$r_i=\frac{k_i(2\beta-\alpha k_i)}{\sigma\alpha},\quad i=1,2,\cdots,N. \tag{32}$$

respectively.

The simplified Hirota's method admits the use of the auxiliary function $f(x,y,t)$ for the singular kink solution by

$$f(x,y,t)=1-\mathrm{e}^{\theta}. \tag{33}$$

Using the potential (28) gives the single singular kink solution by

$$u(x,y,t)=-\frac{2k_1\mathrm{e}^{k_1x+\frac{k_1(2\beta-\alpha k_1)}{\sigma\alpha}y-\left(\frac{4k_i(\alpha^2k_1^2-3\alpha\beta k_1+3\beta^2)}{\alpha^2}\right)t}}{\alpha\left(1-\mathrm{e}^{k_1x+\frac{k_1(2\beta-\alpha k_1)}{\sigma\alpha}y-\left(\frac{4k_1(\alpha^2k_1^2-3\alpha\beta k_1+3\beta^2)}{\alpha^2}\right)t}\right)}. \tag{34}$$

For the two kink solutions we set

$$f(x,y,t)=1-\mathrm{e}^{\theta_1}-\mathrm{e}^{\theta_2}. \tag{35}$$

This in turn gives the two singular kink solutions given by

$$u(x,y,t)=-\frac{2\sum_{i=1}^{2}k_i\mathrm{e}^{k_ix+\frac{k_i(2\beta-\alpha k_i)}{\sigma\alpha}y-\left(\frac{4k_i(\alpha^2k_i^2-3\alpha\beta k_i+3\beta^2)}{\alpha^2}\right)t}}{\alpha\left(1-\sum_{i=1}^{2}\mathrm{e}^{k_ix+\frac{k_i(2\beta-\alpha k_i)}{\sigma\alpha}y-\left(\frac{4k_i(\alpha^2k_i^2-3\alpha\beta k_i+3\beta^2)}{\alpha^2}\right)t}\right)}. \tag{36}$$

For the three kink solutions, we set

$$f(x,y,t)=1-\mathrm{e}^{\theta_1}-\mathrm{e}^{\theta_2}-\mathrm{e}^{\theta_3} \tag{37}$$

Proceeding as before, we find that the three kink solutions are given by

$$u(x,y,t)=-\frac{2\sum_{i=1}^{3}k_i\mathrm{e}^{k_ix+\frac{k_i(2\beta-\alpha k_i)}{\sigma\alpha}y-\left(\frac{4k_i(\alpha^2k_i^2-3\alpha\beta k_i+3\beta^2)}{\alpha^2}\right)t}}{\alpha\left(1-\sum_{i=1}^{3}\mathrm{e}^{k_ix+\frac{k_i(2\beta-\alpha k_i)}{\sigma\alpha}y-\left(\frac{4k_i(\alpha^2k_i^2-3\alpha\beta k_i+3\beta^2)}{\alpha^2}\right)t}\right)}. \tag{38}$$

This shows that the (2+1)-dimensional Gardner equation (26) gives N-kink solutions for finite N, where $N\geq 1$. Based on the obtained results, the general singular *N*-kink solutions can be set in the form

$$u(x,y,t)=-\frac{2\sum_{i=1}^{N}k_i\mathrm{e}^{k_ix+\frac{k_i(2\beta-\alpha k_i)}{\sigma\alpha}y-\left(\frac{4k_i(\alpha^2k_i^2-3\alpha\beta k_i+3\beta^2)}{\alpha^2}\right)t}}{\alpha\left(1-\sum_{i=1}^{N}\mathrm{e}^{k_ix+\frac{k_i(2\beta-\alpha k_i)}{\sigma\alpha}y-\left(\frac{4k_i(\alpha^2k_i^2-3\alpha\beta k_i+3\beta^2)}{\alpha^2}\right)t}\right)}. \tag{39}$$

4. DISCUSSION

We studied in this work the (2+1)-dimensional Gardner equation proposed by Konopelchenko and Dubrovsky in [2, 3]. We employed the simplified form of Hirota's direct method to derive multiple kink solutions and multiple singular kink solutions. This equation is integrable and can be reduced to other integrable equations.

REFERENCES

1. A. OSBORNE, *Nonlinear ocean waves and inverse scattering transform*, Elsevier, Amsterdam, 2010.
2. B.G. KONOPELCHENKO, *Inverse spectral transform for the (2+1)-dimensional Gardner equation*, Inverse Problems, **7**, pp. 739–753, 1991.

3. B.G. KONOPELCHENKO, V.G. DUBROVSKY, *On the general structure of nonlinear equations integrable by the general linear spectral problem*, Phys. Lett. A, **95**, *9*, pp. 457–461, 1983.
4. G.-FU, and H.-E. TAM, *On the (2+1)-dimensional Gardner equation: Determinant solutions and pfaffianization*, J. Math. Anal. Appl., **330**, pp. 989–1001, 2007.
5. A.M.WAZWAZ, *New solitons and kink solutions for the Gardner equation*, Commun. Nonlin. Sci. Numer. Simulat., **12**, *8*, pp. 1395–1404, 2007.
6. A. M. WAZWAZ, *Solitons and singular solitons for the Gardner-KP equation*, Appl. Math. Comput., **204**, *1*, pp. 162–169, 2008.
7. B.B. KADOMTSEV, V.I. PETVIASHVILI, On the stability of solitary waves in weakly dispersive media, Sov. Phys. Dokl., **15**, pp. 539–541, 1970.
8. R. NAZ, Z. ALI, I. NAEEM, *Reductions and new exact solutions of ZK, Gardner KP, and modified KP Equations via generalized double reduction theorem*, Abstract and Applied Analysis, **2013**, 340564, 2013.
9. P. CAI, J.-S. TANG, Z.-B. LI, *Bifurcation of exact traveling wave solutions for Gardner and Gardner-KP equations*, Intern. J of Appl. Math. and Statistics, **44**, *14*, pp. 461–468, 2013.
10. R. HIROTA, *The Direct Method in Soliton Theory*, Cambridge University Press, Cambridge, 2004.
11. H. LEBLOND, H. TRIKI, D. MIHALACHE, *Derivation of a generalized double-sine-Gordon equation describing ultrashort-soliton propagation in optical media composed of multilevel atoms*, Phys. Rev. A, **86**, 063825, 2012.
12. H. LEBLOND, D. MIHALACHE, *Models of few optical cycle solitons beyond the slowly varying envelope approximation*, Phys. Reports, **523**, pp. 61–126, 2013.
13. W. HEREMAN, A. NUSEIR, *Symbolic methods to construct exact solutions of nonlinear partial differential equations*, Mathematics and Computers in Simulation, **43**, pp. 13–27, 1997.
14. A. JAFARIAN et al., *Construction of soliton solutions to the Kadomtsev-Petviashvili-II equation using homotopy analysis method*, Rom. Rep. Phys., **65**, pp. 76–83, 2013.
15. A. M. WAZWAZ, *Multiple soliton solution for two integrable couplings of the modified Korteweg-de Vries equation*, Proc. Romanian Acad. A, **14**, pp. 219–225, 2013.
16. H. TRIKI et al., *Shock wave solution of Benney-Luke equation*, Rom. J. Phys., **57**, pp. 1029–1034, 2012.
17. H. LEBLOND, H. TRIKI, D. MIHALACHE, *Theoretical studies of ultrashort-soliton propagation in nonlinear optical media from a general quantum model*, Rom. Rep. Phys., **65**, pp. 925–942, 2013.
18. A.M. WAZWAZ, *Partial Differential Equations and Solitary Waves Theorem*, Springer and HEP, Berlin, 2009.
19. A.M. WAZWAZ, *Multiple-front solutions for the Burgers equation and the coupled Burgers equations*, Appl. Math. Comput., **190**, pp. 1198–1206, 2007.
20. A.M. WAZWAZ, *Multiple-front solutions for the Burgers-Kadomtsev-Petvisahvili equation*, Appl. Math. Comput., **200**, pp. 437–443, 2008.
21. A.M. WAZWAZ, *Solitary wave solutions of the generalized shallow water wave (GSWW) equation by Hirota's method, tanh-coth method and Exp-function method*, Appl. Math. Comput., **202**, pp. 275–286, 2008.
22. A.M. WAZWAZ, *Integrable couplings of the Burgers equation and the Sharma-Tasso-Olver equation*, Rom. Rep. Phys., **65**, pp. 383–390, 2013.
23. A.M. WAZWAZ, The *Volterra integro-differential forms of the singular Flierl-Petviashvili and the Lane-Emden equations with boundary conditions*, Rom. J. Phys., **58**, pp. 685–693, 2013.

Received January 6, 2014

THE PUBLISHING HOUSE
OF THE ROMANIAN ACADEMY

PROCEEDINGS OF THE ROMANIAN ACADEMY, Series A,
Volume 15, Number 3/2014, pp. 247–253

MICRO AND NANOHARDNESS TESTING OF LASER WELDS

Hana SEBESTOVA [1], Radim CTVRTLIK [2], Hana CHMELICKOVA [1], Jan TOMASTIK [1]

[1] Palacky University of Olomouc, Faculty of Science, RCPTM, Joint Laboratory of Optics of Palacky University and Institute of Physics of the ASCR, 17. listopadu 12, 771 46 Olomouc, Czech Republic
[2] Institute of Physics of the Academy of Sciences of the Czech Republic, Joint Laboratory of Optics of Palacky University and Institute of Physics of the ASCR, 17. listopadu 50a, 772 07 Olomouc, Czech Republic
E-mail: hana.sebestova@upol.cz

Local mechanical properties of pulsed Nd:YAG laser bead-on-plate welds on 0.6 thick AISI 304 stainless steel were investigated. Conventional Vickers micro-hardness, based on measurement of dimension of residual indent, and depth sensing nanoindentation were used. Measurements were performed on both transversal and longitudinal weld cross sections. Seam welds performed with the pulsed laser reached very inhomogeneous microstructure resulting from the principle of successive pulses landing on the material surface whereas each pulse partially overlaps and re-melts the area melted by the previous one. This led to the fluctuations in both Vickers microhardness and indentation hardness of the weld metal.

Key words: Vickers microhardness, depth sensing indentation, laser welding.

1. INTRODUCTION

Laser welding is a high power density technology of materials joining that has many advantages in comparison with conventional fusion welding methods, for example high accuracy, flexibility, repeatability and especially very narrow heat affected zone which results in minimal workpiece distortions [1].

Hardness tests are widely used for weld mechanical properties evaluation and thus its quality estimation. Typical increase of weld metal hardness followed by its decrease in heat affected zone can be observed in most of conventionally prepared weld joints [2]. In case of laser welding, much higher cooling rates are present and thus different weld characteristics can be expected. Especially thin sheets (< 1.5 mm) seam welding with a pulsed laser results in very small-sized welds with heat affected zone often unobservable using light microscopic techniques [3]. In such cases utilization of micro- and especially nanoindentation techniques is appropriate for reliable measurement of mechanical properties of the welded material [4–8].

2. EXPERIMENT

Pulsed Nd:YAG laser LASAG KLS 246-102 with maximal average power 150 W was used for bead-on-plate welding of 0.6 mm thick AISI 304 stainless steel sheets. Pulse repetition frequency 13 Hz, welding speed 4 $mm \cdot s^{-1}$ and working distance 4 mm under the focal plane were kept constant during all experiments. Protective argon gas (8 $l \cdot min^{-1}$) was applied coaxially with the laser beam. Other processing parameters are concluded in Table 1. Fig. 1 presents used laser system. Experimental set-up is displayed in Fig. 2.

Table 1

Applied processing parameters

Sample no.	Pulse length [ms]	Pulse energy [J]	Average power [W]	Peak power [kW]
I	2.6	3.5	45.5	1.35
II	3.9	4.7	61.1	1.21
III	3.4	5.9	76.7	1.74
IV	3.4	6.2	80.6	1.82

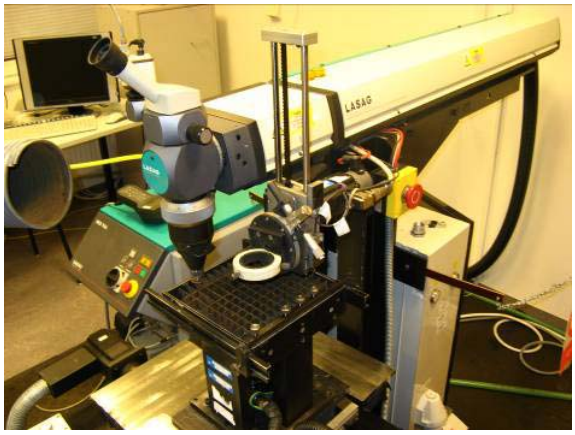

Fig. 1 – Laser system LASAG.

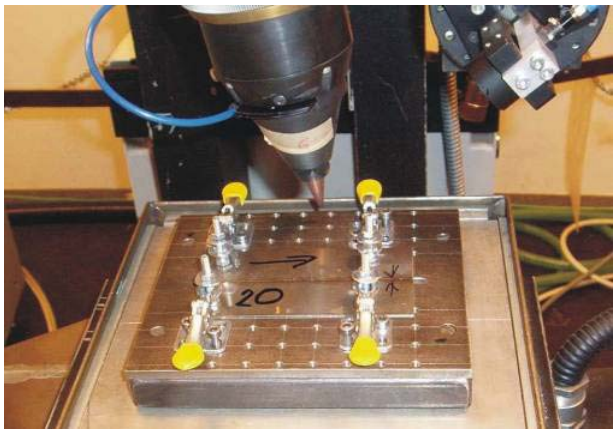

Fig. 2 – Experimental set-up.

3. HARDNESS MEASUREMENT

Laser welds were cut perpendicularly and selected welds both longitudinally to the welding direction to study its local hardness properties in detail. Polished samples of basic material and laser weld cross sections mounted in cold casting resin were etched with a mixture of hydrochloric and nitric acid (3:1) to induce their microstructure.

3.1. Vickers microhardness tests

First, basic material microhardness was evaluated using automatic hardness tester LECO AMH43 with Vickers indenter at applied load of 500 mN. Fifteen measurements were performed. The average value reached (270 ± 25) HV 0.05.

Second, metallographic specimens of cross sections perpendicular to the welding direction were analysed. Weld microhardness was measured along the centre of the weld cross section from its surface to the root in discrete points spaced by 70 μm or 100 μm, respectively. Supplemental measurements were performed perpendicularly, in the centre of the metal sheet. Fig. 3 presents weld perpendicular cross sections micrographs with the designation of indents positions and corresponding values of measured microhardness.

Laser power applied in case of sample I and II was insufficient for the full penetration. Thus only few indents lie in the weld metal. Sample I weld metal microhardness is within the tolerance limit of basic material microhardness. Little decrease of microhardness was detected 50 μm far from the weld line although no visible heat affected zone was observed using light microscope. Measurements performed in the centre of the metal sheet confirmed this decrease.

Sample II exhibits generally lower microhardness in both weld metal and basic material and it is almost constant for all investigated positions from the weld surface towards its centre. Local decrease was detected only in the centre of the metal sheet close to the weld root.

Typical microstructure of pulsed laser seam weld perpendicular cross section can be found at sample III, which results in not uniform values of weld metal local microhardness. Comparing sample III and IV corresponding to nearly similar welding conditions, very different microhardness values were detected. This is probably thanks to the different cross section position and grain orientation effect resulting from relatively small pulse overlap (63 %). Sample IV was the only one exhibiting weld metal microhardness increase and it reached about 20 %.

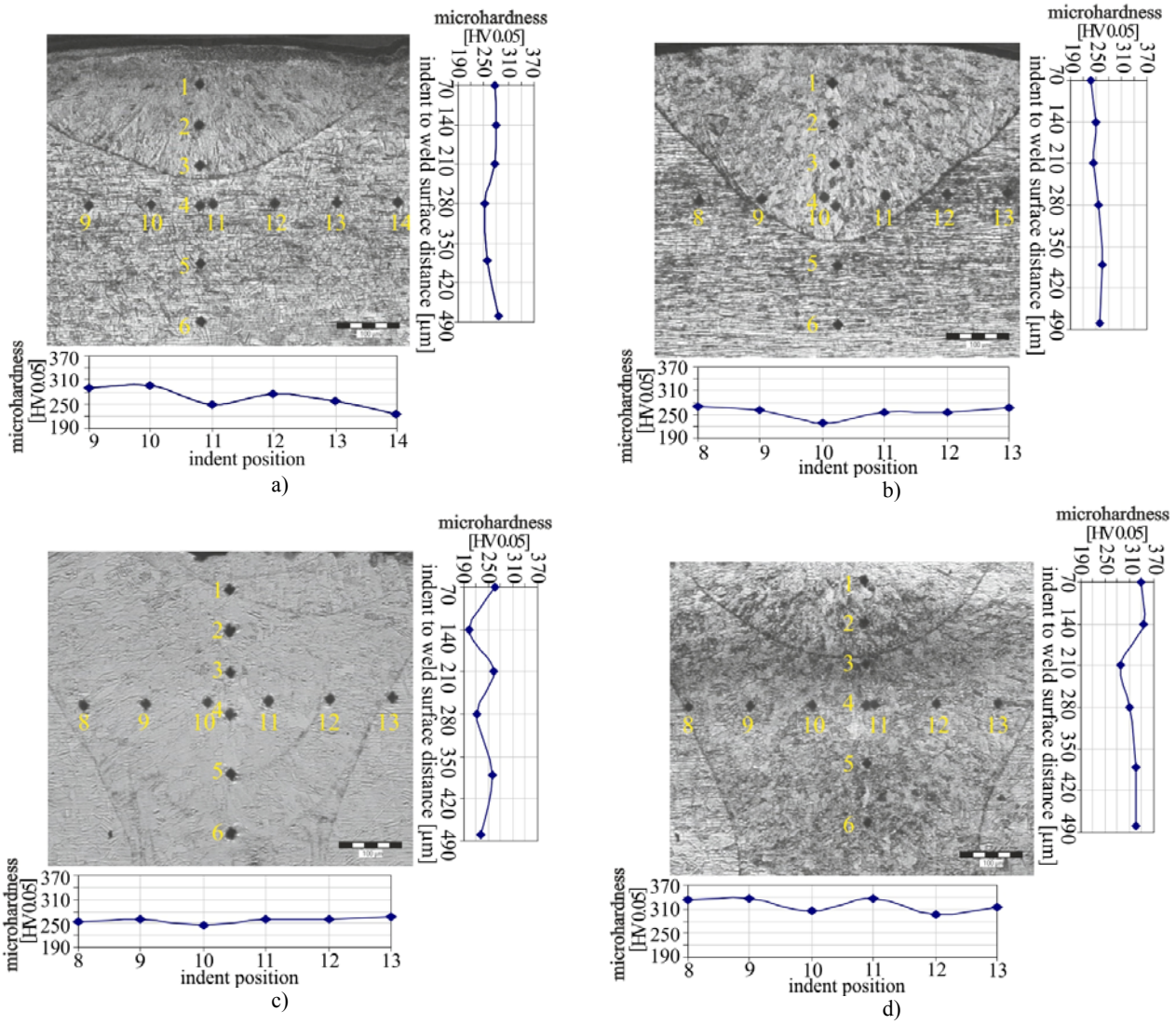

Fig. 3 – Weld perpendicular cross sections with results of Vickers microhardness tests of sample no.: a) I; b) II; c) III; d) IV.

3.2. Depth sensing indentation tests

Nanoindentation (depth sensing indentation) is a contact based technique widely used for evaluation of mechanical properties at small scales. During a typical test a diamond tip of known geometry is pressed into the sample surface, while the indentation load and depth are continuously recorded. Unlike traditional hardness measurements it allows evaluation of reduced elastic modulus or creep characteristics. Therefore it can provide us with new information about fine welds properties.

Selected samples of laser welds were also examined by the nanoindentation to study local weld properties in detail. The measurements were carried out using the fully calibrated NanoTest NTX system (MicroMaterials). Room temperature indentation with Berkovich indenter was performed at different loads. Measured indentation curves were analysed using standard method [9-10].

First, basic material and sample II indentation hardness and elastic modulus were evaluated at load of 50 mN. Basic material indentation hardness reached (2.6 ± 0.3) GPa and its reduced elastic modulus was (205 ± 11) GPa. Selected region of sample II covering both weld metal and basic material was investigated. 48 indents with spacing of 30 µm were performed over the area of 60 × 450 µm. The positions of indents together with measured data of sample II are displayed in Fig. 4.

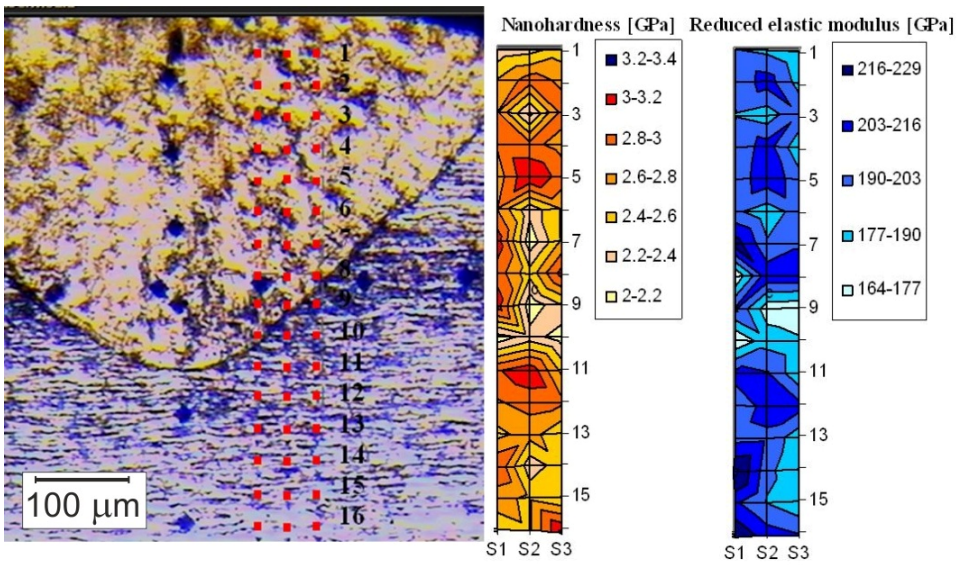

Fig. 4 – Sample II micrograph with indentation hardness and reduced elastic modulus data (measured at 50 mN).

Higher spatial resolution of nanoindentation revealed local decrease of hardness and reduced elastic modulus at the weld line of sample II. To confirm this result, sample III was investigated. Weld metal, heat affected zone and weld line were analysed on perpendicular weld cross section of sample III. Maximal indentation load was 50, 80 and 250 mN. Spacing between indents was 30 µm. Several regions of sample III were investigated in series of indents perpendicular to the weld line. An overview of regions, those nanohardness results are presented in this paper, with their designation and position towards the weld is depicted in Fig. 5.

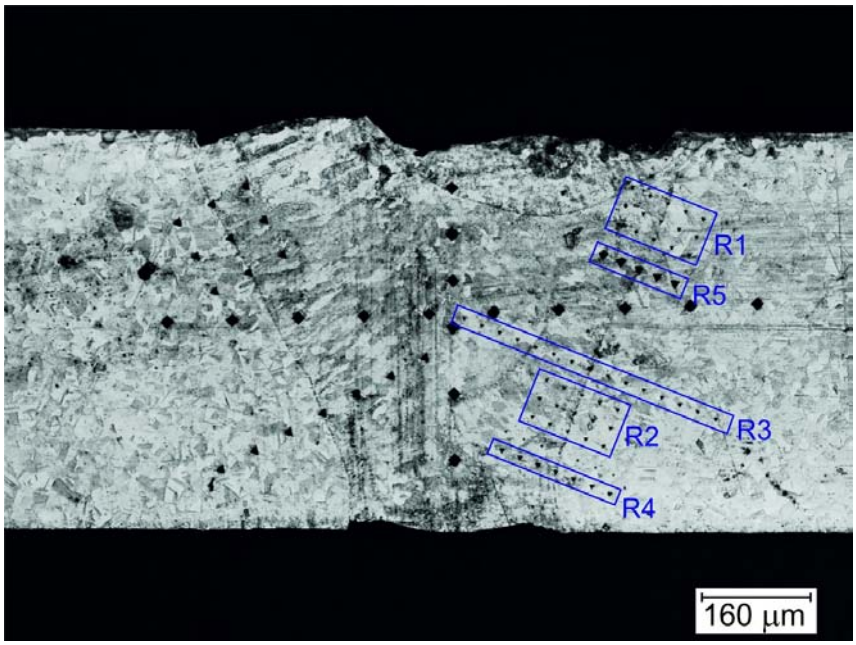

Fig. 5 – Sample III micrograph with investigated regions designation.

First, the same maximal load (50 mN) was applied as in the case of sample II. Local mechanical properties were analysed near the top, in the central and in the root region of the weld. Figs. 6 and 7 present details of investigated regions R1 and R2 with measured indentation hardness data. Very diverging values were reached at corresponding positions at region R1 both R2. Indentation hardness decrease at the weld line was identified only individually, thus general decrease of hardness on the weld line was not proved.

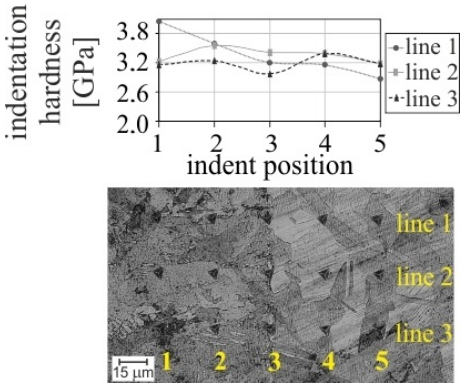

Fig. 6 – Detail of investigated region R1 of sample III with indentation hardness data (measured at 50 mN).

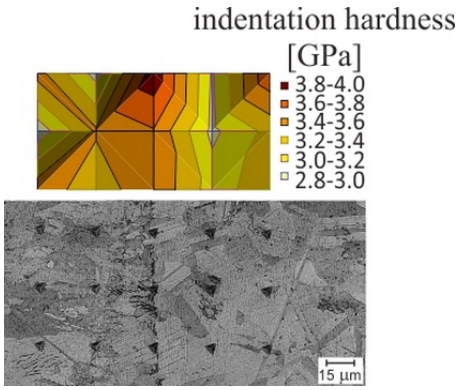

Fig. 7 – Detail of investigated region R2 of sample III with indentation hardness data (measured at 50 mN).

Depth sensing indentation provides us also with the creep data. Fig. 8 presents indentation hardness measured in region R3 of sample III together with three creep curves corresponding to the indent position 6 (weld metal), 8 (weld line) and 10 (heat affected zone/basic material). Analysed creep curves were shifted to start at the same depth, so as their shape could be easily compared. Higher hardness corresponded to the lower creep.

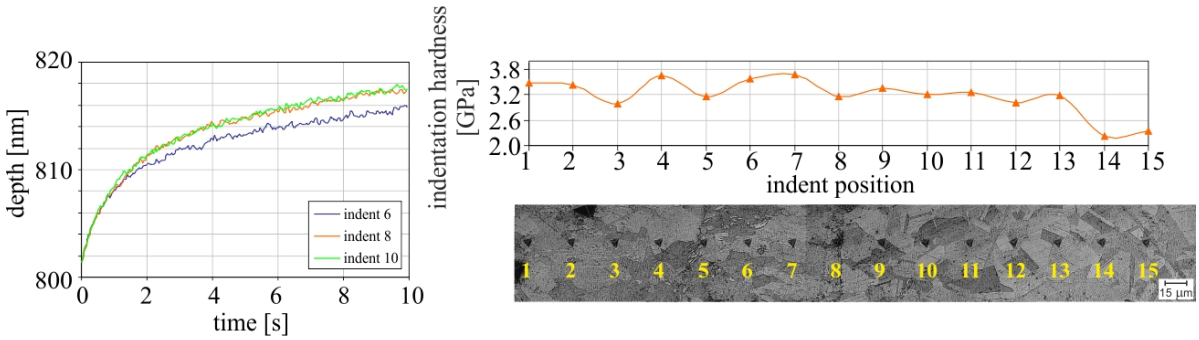

Fig. 8 – Detail of investigated region R3 of sample III with indentation hardness data and creep curves (measured at 50 mN).

Complementary measurements were performed with maximal applied load of 80 mN in region R4 (Fig. 9) and 250 mN in region R5 (Fig. 10), respectively. It is evident that increase of indentation load does not have any effect on hardness values.

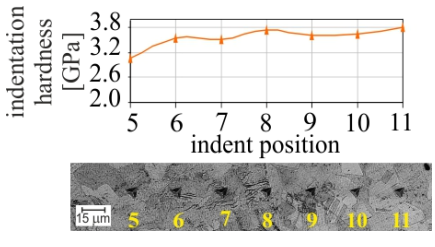

Fig. 9 – Detail of investigated region R4 of sample III with indentation hardness data (measured at 80 mN).

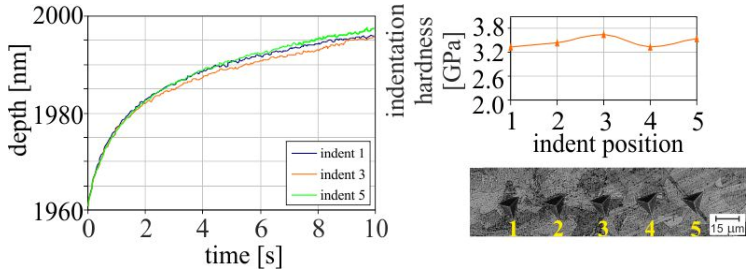

Fig. 10 – Detail of investigated region R5 of sample III with measured indentation hardness data and creep curves (measured at 250 mN).

Indentation hardness measured at sample III is generally higher in comparison to the sample II, which was also revealed by Vickers microhardness measurements.

Weld off-axis longitudinal cross section was prepared to study the effect of individual laser pulses on weld mechanical properties at the boarders between regions melted by consecutive laser pulses. Both indentation hardness and reduced elastic modulus were investigated along the line with indents spacing of

60 μm with maximal applied load of 250 mN. Positions of indents together with measured data are displayed in Fig. 11. Seam welds performed with a pulsed laser have very inhomogeneous structure resulting from repetitive melting of the weld metal. Thus very different data can be found when different perpendicular cross sections of the one weld are analysed. About 10% fluctuation of indentation hardness data measured on longitudinal cross section can be observed. This fluctuation does not strictly correspond to the periodicity of the weld structure.

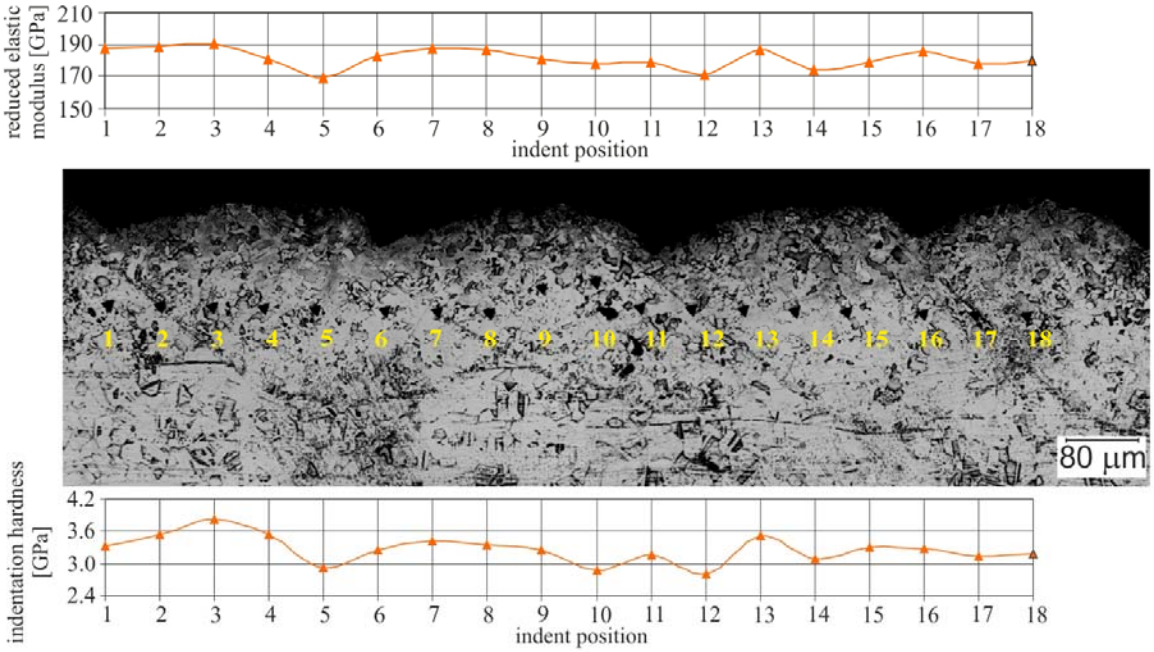

Fig. 11 – Weld off-axis longitudinal cross section with results of sample III indentation hardness and reduced elastic modulus measurements (measured at 250 mN).

4. CONCLUSION

Bead-on-plate welding experiments were carried out with different energies and pulse lengths. After the preparation of metallographic specimens Vickers microhardness and depth sensing indentation tests were performed. Basic material microhardness reached (270 ± 25) HV 0.05. Weld metal microhardness increase (+20 %) was detected only at sample IV, while other samples exhibit rather decrease (II, III) or almost no change. Typical microstructure of pulsed laser seam weld perpendicular cross section can be found at sample III, which results in not uniform values of weld metal local microhardness. Comparing sample III and IV corresponding to similar welding conditions, very different microhardness values were detected. This is probably thanks to the grain orientation effect resulting from relatively small pulse overlap (63 %). To reach average weld metal microhardness, more cross sections of the one sample would have to be evaluated.

Comparing depth sensing indentation data with respect to the indents positions, no definite relation was found. Hardness of adequate regions significantly fluctuates, which corresponds to the Vickers microhardness measurements. Individual grain orientation probably influences local hardness. Although applied maximal loads were quite high, the benefit of depth sensing indentation towards Vickers microhardness test is the possibility of reduced elastic modulus or creep characteristics measurement.

ACKNOWLEDGEMENTS

The authors gratefully acknowledge the support by the Operational Program Education for Competitiveness – ESF (CZ.1.07/2.4.00/17.0014) and by the Technology Agency of the Czech Republic (TA01010517).

REFERENCES

1. DULEY, W. W., *Laser welding*, Wiley, 1999.
2. Jenney, C. L., O'Brian, A., *Welding Handbook*, Volume 1 – Welding Science and Technology, AWS, 2001.
3. STEEN, W. M., *Laser Material Processing*, Springer, 2003.
4. CHEN, J., SAND, K., XIA, M. S., OPHUS, C., MOHAMMADI, R., KUNTZ, M. L., ZHOU, Y., MITLIN, D., *Transmission Electron Microscopy and Nanoindentation Study of the Weld Zone Microstructure of Diode-Laser-Joined Automotive*, Transformation-Induced Plasticity Steel, Metallurgical and Materials Transactions A, **39A**, pp. 593-603, 2008.
5. HERNANDEZ, V. H. B., PANDA, S. K., OKITA, Y., ZHOU, N. Y., *A study on heat affected zone softening in resistance spot welded dual phase steel by nanoindentation*, Journal of Materials Science, **45**, *6*, pp. 1638-1647, 2010.
6. CABIBBO, M., FORCELLESE, A., EL MEHTEDI, M., SIMONCINI, M., *Double side friction stir welding of AA6082 steets: Microstructure and nanoindentation characterization,* Materials Science & Engineering A, **590**, pp. 209–217, 2014.
7. CHARITIDIS, C. A., DRAGATOGIANNIS, D. A., KOUMOULOS, E. P., KARTSONAKIS, I. A., *Residual stress and deformation mechanism of friction stir welded aluminum alloys by nanoindentation*, Materials Science & Engineering A, **540**, pp. 226–234, 2012.
8. KOUMOULOS, E. P., CHARITIDIS, C. A., DANIOLOS, N. M., PANTELIS, D. I*., Nanomechanical properties of friction stir welded AA6082-T6 aluminum alloy*, Materials Science & Engineering B, **176**, pp. 1585–1589, 2011.
9. OLIVER, W. C., PHARR, G. M., Pharr G.M., *Improved technique for determining hardness and elastic modulus using load and displacement sensing indentation experiments*, Journal of Materials Research, **7**, *6*, pp. 1564-1580, 1992.
10. OLIVER, W. C., PHARR, G. M., *Measurement of hardness and elastic modulus by instrumented indentation: Advances in understanding and refinements to methodology*, Journal of Materials Research, **19**, *1*, pp. 3-20, 2004.

Received February 24, 2014

THE PUBLISHING HOUSE
OF THE ROMANIAN ACADEMY

PROCEEDINGS OF THE ROMANIAN ACADEMY, Series A,
Volume 15, Number 3/2014, pp. 254–261

GROUND FAULT LOCATION INFLUENCE ON AC POWER LINES IMPEDANCES

Maria VINȚAN

"Lucian Blaga" University of Sibiu
E-mail: maria.vintan@ulbsibiu.ro

In this paper it will be presented an analytical method in order to determine the ground fault current distribution in effectively grounded power networks. In our previous works it has been assumed that the transmission line has only one ground wire. In this paper, additionally it is considered the case where there are two ground wires. There are also presented some useful quantitative results obtained through a dedicated developed MATLAB 7.0 program.

Key words: power system faults, transmission lines, ground fault current.

1. INTRODUCTION

When a ground fault occurs on an overhead transmission line in a three-phase power network with grounded neutral, the fault current returns to the grounded neutral through the towers, ground return path and ground wires. The estimation of the ground current distribution has many major applications in power systems design, especially in grounding systems. Extensive work has been undertaken in order to model transmission network for ground fault current analysis [2–13]. The ground fault divides the line into two sections, each extending from the fault towards one end of the line. Depending of the number of towers between the faulted tower and the stations, respectively of the distance between the towers, these two sections of the line may be considered infinite, in which case the ground fault current distribution is independent on the termination of the network; otherwise, they must be regarded as finite, in which case the ground fault current distribution may depend greatly on the termination of the network [3, 4, 8, 12, 13]. In our previous works it was presented an analytical method in order to determine the ground fault current distribution in effectively grounded power network. It was assumed that the transmission line has only one ground wire [14, 15, 16]. In this paper it will be presented the case when there are two ground wires, too. It will be considered the case that those two sections of the line are both infinite, respectively both finite. The calculation method is based on the following assumptions: the network is considered linear in the sinusoidal steady-state; only the fundamental frequency is considered and impedances are considered as lumped parameters in each span of the transmission.

2. GROUND FAULT CURRENT DISTRIBUTION ON AN INFINITE TRANSMISSION LINE WITH ONE GROUND WIRE

A long line is one which has a middle section where the line is divided by each tower into infinite half-lines. In Fig. 1 the fault occurs at large distance from both terminals, at the tower number *0*. It is assumed that the fault is fed from both directions. The impedance of the ground wire connected between two grounded towers, called the self impedance per span, it is noted with Z_{cp_d}. The mutual impedance between the ground wire and the faulted phase conductor, per span, was noted with Z_m. Those two section of the line being both infinite, the situation in the left part from the faulted tower is identically with the situation in the right part.

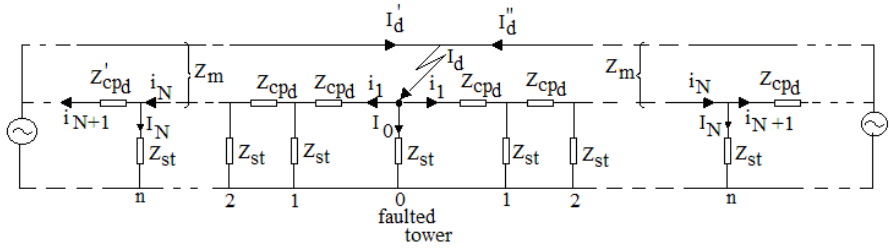

Fig. 1 – Ground fault current distribution on an infinite transmission line with one ground wire.

The current I_n flowing to ground through the n-th tower, counted from the faulted tower, is equal with the difference between the currents i_n and i_{n+1} [14, 15, 16]:

$$I_n = i_n - i_{n+1}. \tag{1}$$

The loop equation for the n-th mesh is given by the next expression:

$$I_n Z_{st} - I_{n-1} Z_{st} + i_n Z_{cp_d} - \nu I_d Z_{cp_d} = 0. \tag{2}$$

In expression (2) ν represents the coupling factor between the overhead phase and ground wire $\left(\nu = \frac{Z_m}{Z_{cp_d}}\right)$.The equation (2) could be written in the next form:

$$i_n = \frac{(I_{n-1} - I_n) Z_{st}}{Z_{cp_d}} + \nu I_d. \tag{3}$$

Similarly:

$$i_{n+1} = \frac{(I_n - I_{n+1}) Z_{st}}{Z_{cp_d}} + \nu I_d. \tag{4}$$

Substituting relations (3) and (4) in relation (1), for the current I_n will be obtained the next second order homogeneous difference equation:

$$I_n \frac{Z_{cp_d}}{Z_{st}} = I_{n+1} - 2I_n + I_{n-1}. \tag{5}$$

According to [10], the solution of this equation is the following:

$$I_n = A e^{\alpha n} + B e^{-\alpha n}. \tag{6}$$

The parameters A and B could be obtained from the boundary conditions. Parameter α in the solution (6) could be obtained by substituting the solution (6) in equation (5). By applying equation (1) to the (n-1) tower, it will be obtained the following expression:

$$I_{n-1} = i_{n-1} - i_n. \tag{7}$$

By substituting the equations (1) and (7) in equation (2), it will be obtained the next equation:

$$i_n \frac{Z_{cp_d}}{Z_{st}} = i_{n+1} - 2i_n + i_{n-1} + \nu I_d \frac{Z_{cp_d}}{Z_{st}}. \tag{8}$$

Similarly with equation (5), the current in the ground wire is given by the next solution:

$$i_n = a e^{\alpha n} + b e^{-\alpha n} + \nu I_d. \tag{9}$$

In expression (9) *a, b* represent parameters. Due to the link between currents i_n and I_n, the parameters *A, B* and *a, b* are not independent. By substituting the solutions (6) and (9) in equation (1), it will be obtained:

$$A\mathrm{e}^{\alpha n} + B\mathrm{e}^{-\alpha n} = a\mathrm{e}^{\alpha n}(1-\mathrm{e}^{\alpha}) + b\mathrm{e}^{-\alpha n}(1-\mathrm{e}^{-\alpha}). \tag{10}$$

Because these relations are the same for every value of *n*, it will be obtained the next expressions:

$$A = a(1-\mathrm{e}^{\alpha}) \tag{11}$$

$$B = b(1-\mathrm{e}^{-\alpha}). \tag{12}$$

The current in the ground wire will be then given by the following expression:

$$i_n = A\frac{\mathrm{e}^{\alpha n}}{1-\mathrm{e}^{\alpha}} + B\frac{\mathrm{e}^{-\alpha n}}{1-\mathrm{e}^{-\alpha}} + \nu I_d. \tag{13}$$

If the line is sufficiently long so that, after some distance, the varying portion of the current exponentially decays to zero (infinite line), then the parameter $A \to 0$. In this case only the parameter *B* must be determined from the boundary conditions [10], [13]. According to (6) and (13), it can be written:

$$I_n = B\mathrm{e}^{-\alpha n} \tag{14}$$

$$i_n = B(\mathrm{e}^{-\alpha n}/1-\mathrm{e}^{-\alpha}) + \nu I_d. \tag{15}$$

The boundary condition at the faulted tower will be the following:

$$I_d = I_0 + 2i_1. \tag{16}$$

Substituting expressions (14) and (15) in (16), with $n=0$ for I_n and $n=1$ for i_n, it could be obtained the expression for the current in the faulted tower.

3. GROUND FAULT CURRENT DISTRIBUTION ON A FINITE TRANSMISSION LINE WITH ONE GROUND WIRE

Next, it is treated the case when those two sections of the line are divided by the faulted tower into two finite sub-lines. In Fig. 2 the fault occurs at the tower number *0*.

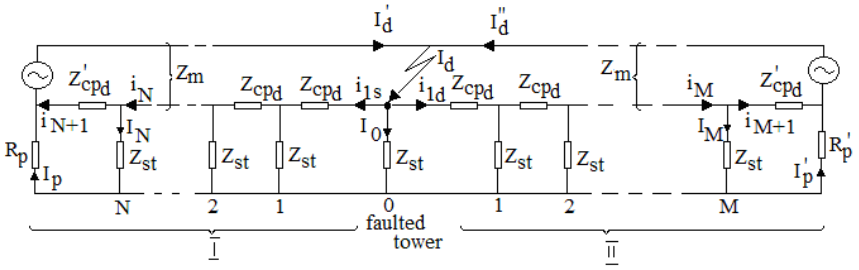

Fig. 2 – Ground fault current distribution on a finite transmission line with one ground wire.

There are *N* towers between this tower and the left station and respectively *M* towers between tower number 0 and the right station. The resistances of the grounding systems from the left, respectively from the right stations (Fig. 2) are R_p, respectively R'_p. The impedance of the ground wire in the last span is Z'_{cp_d}, and $Z_p = R_p + Z'_{cp_d}$, respectively $Z'_p = R'_p + Z'_{cp_d}$. The total fault current I_d is given by the sum between the current I'_d from one side, and I'_d from the other side of the transmission line.

Considering the left part from the faulted tower, the situation is identically with that presented in Fig. 1. The solutions for the current in the towers, respectively in the ground wire are:

$$I_{n-s} = A_s \mathrm{e}^{\alpha n} + B_s \mathrm{e}^{-\alpha n}, \tag{17}$$

$$i_{n-s} = A_s \frac{\mathrm{e}^{\alpha n}}{1-\mathrm{e}^{\alpha}} + B_s \frac{\mathrm{e}^{-\alpha n}}{1-\mathrm{e}^{-\alpha}} + \nu I_d^{'}. \tag{18}$$

The subscript s is used for the left part from the faulted tower [3]. I_{n-s} represents the current in the tower number n, counted from the faulted tower to the left part of the transmission line. The parameters A_s, B_s will be obtained from the boundary conditions. For the faulted tower, the following formulas can be written:

$$\begin{cases} I_0 Z_{st} - I_{1s} Z_{st} - i_{1s} Z_{cp_d} + \nu Z_{cp_d} I_d^{'} = 0 \\ I_{1s} Z_{st} - I_{2s} Z_{st} - i_{2s} Z_{cp_d} + \nu Z_{cp_d} I_d^{'} = 0. \end{cases} \tag{19}$$

Also it can be written the next expression:

$$I_{1s} = i_{1s} - i_{2s}. \tag{20}$$

Substituting i_{1s} and i_{2s} from equations (19) in equation (20), it will be obtained:

$$I_{1s}(2 + Z_{cp_d} / Z_{st}) = I_0 + I_{2s}. \tag{21}$$

According to [3] for the left terminal it can be written:

$$I_N + i_{N+1} = i_N, \tag{22}$$

$$I_N Z_{st} + I_p R_p - i_{N+1} Z'_{cp_d} + Z'_m I'_d = 0, \tag{23}$$

$$(I_{N-1} - I_N) Z_{st} - i_N Z_{cp_d} + \nu Z_{cp_d} I'_d = 0, \tag{24}$$

$$i_{N+1} = I'_d - I_p, \tag{25}$$

where Z'_m represents the mutual coupling between the ground wire and the faulted phase, in the last span. Replacing i_{N+1} and i_N from expressions (23), (24) in (22), by taking into account expression (25), it will be obtained the following expression:

$$I_N \left(1 + \frac{Z_{st}}{Z_{cp_d}} + \frac{Z_{st}}{Z'_{cp_d} + R_p}\right) = I_{N-1} \frac{Z_{st}}{Z_{cp_d}} + I_d^{'} \left(\nu - \frac{R_p + Z'_m}{Z'_{cp_d} + R_p}\right). \tag{26}$$

The expressions (21) and (26) represent the boundary conditions. A_s and B_s will be obtained by replacing I_{1s}, I_{2s}, I_N and I_{N-1} from the solutions (17) and (18) in (21) and (26).

4. SIMILAR EXPRESSIONS COULD BE OBTAINED FOR THE CURRENTS FROM THE RIGHT PART OF THE FAULTED TOWER. TRANSMISSION LINE WITH TWO GROUND WIRES

So far it was considered that the transmission line has only one ground wire. When there are two ground wires, if they are identical and disposed in a mutually symmetrical position, the expressions presented for single ground wire can still be used. In this case, those two ground wires are represented by an imaginary single wire, but the geometric mean radius of the equivalent wire and the geometric mean distance relative to the faulted phase must be substituted [4]. In the general case, presented in Fig. 3, those two ground wires could be modelled as un equivalent ground wire. In this case, the self impedance of the equivalent

ground wire it is noted with Z_{cpe}, respectively the mutual impedance between equivalent ground wire and the faulted phase it is noted with Z_{cpme}. The equivalent impedances Z_{cpe} and Z_{cpme} will represent the group of the ground wires. Expressions for the self impedance of a ground return circuit and for the mutual impedance between two ground return circuits are available from the literature [2], [4]. In case of a single ground wire, these expressions could be directly applied in order to find the mutual impedance between the ground wire and the faulted phase conductor. When there are multiple ground conductors, in order to find the equations for the self and mutual impedances of the group, it must be taken into consideration the mutual coupling between the individual ground wires.

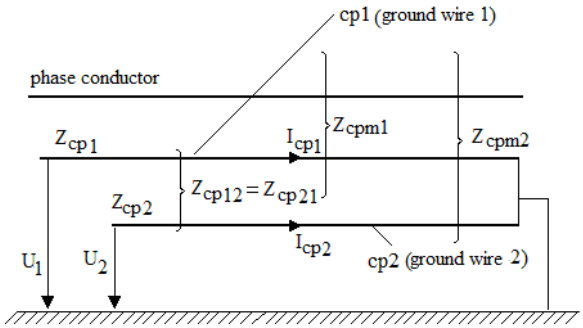

Fig. 3 – Transmission line with two ground wires.

Considering Fig. 3, the following equations could be written:

$$\begin{aligned} U_1 &= Z_{cp11} I_{cp1} + Z_{cp12} I_{cp2} \\ U_2 &= Z_{cp21} I_{cp1} + Z_{cp22} I_{cp2}. \end{aligned} \tag{27}$$

In equation (27), Z_{cp11}, Z_{cp22} represent the self impedance of the ground wires, and Z_{cp12}, Z_{cp21} represent the mutual impedance between the ground wires. These two ground wires, being interconnected at both ends, thus $U_1 = U_2$, and the self impedance of the group can be defined as [4]:

$$Z_{cpe} = \frac{U}{I_{cp1} + I_{cp2}}. \tag{28}$$

The mutual impedance between the equivalent ground wire and the faulted phase conductor is given in the following equation by particularising the corresponding formula presented in [4]:

$$Z_{cpme} = \frac{I_{cp1} Z_{cpm1} + I_{cp2} Z_{cpm2}}{I_{cp1} + I_{cp2}}. \tag{29}$$

In equation (29) Z_{cpm1}, Z_{cpm2} represent the mutual impedances between the ground wires and the faulted phase. From these three expressions, it will be determined the expressions for the self impedance of the equivalent ground wire, respectively for the mutual impedance between equivalent ground wire and the faulted phase.

$$Z_{cpe} = \frac{Z_{cp1} Z_{cp2} - Z_{cp12}^2}{Z_{cp1} + Z_{cp2} - 2Z_{cp12}}, \tag{30}$$

$$Z_{cpme} = \frac{Z_{cpm1}(Z_{cp2} - Z_{cp12}) + Z_{cpm2}(Z_{cp1} - Z_{cp12})}{Z_{cp1} + Z_{cp2} - 2Z_{cp12}}. \tag{31}$$

5. OBTAINED RESULTS

In order to illustrate the theoretical approach outlined in the sections above, we are considering that the line who connects two stations is a 220kV transmission line. The line (Fig. 4) has two aluminium-steel ground wires 160/95 mm^2 [7].

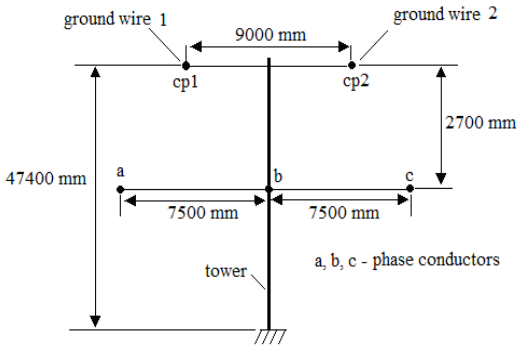

Fig. 4 – Disposition of the transmission line conductors.

Line impedances per one span are determined on the basis of the following assumption: average length of the span is 250 m. Impedance Z_m is calculated only in relation to the faulted phase conductor, because it could not be assumed that a line section of a few spans is transposed. Ground wires impedances per one span and the mutual impedance between the ground wires and the faulted phase are calculated for different values of the soil resistivity with formulas based on Carson's theory of the ground return path [1]. The fault was assumed to occur on the phase which is the furthest from the ground conductors, because the lowest coupling between the phase and ground wire will produce the highest tower voltage. The total fault current from both stations was assumed to be $I_d = 15\,000\ A$. Those values are valid for a soil resistivity of 100 $\Omega \cdot$m. All the further quantitative results are based on the theoretical approaches presented during the previous sections. In order to do this there were developed some numerical intensive programs written in MATLAB 7.0 software frame.

Figure 5 presents the obtained mutual impedance between the two ground wires as a function of the soil resistivity based on Carson's formulas [1], for different values of the horizontal distance between those wires.

Figure 6 presents on the same theoretical basis the mutual impedance between the two ground wires as a function of the horizontal distance between ground wires, for different values of the soil resistivity.

Figure 7 presents, based on expressions (14), the currents flowing through transmission towers as a function of the number of spans, considering, respectively neglecting the coupling factor between the ground wires and the faulted phase.

Figure 8 presents currents through transmission line towers as a function of the number of spans, for different values of the tower impedances. It was considered the case of an infinite transmission line.

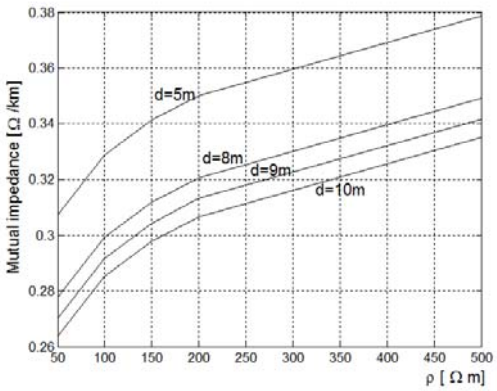

Fig. 5 – The mutual impedance between the two ground wires as a function of the soil resistivity.

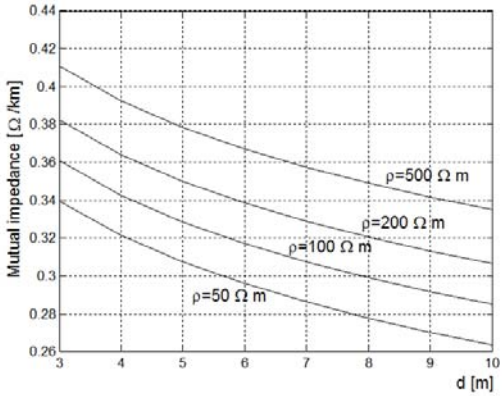

Fig. 6 – The mutual impedance between the two ground wires as a function of the horizontal distance between ground wires.

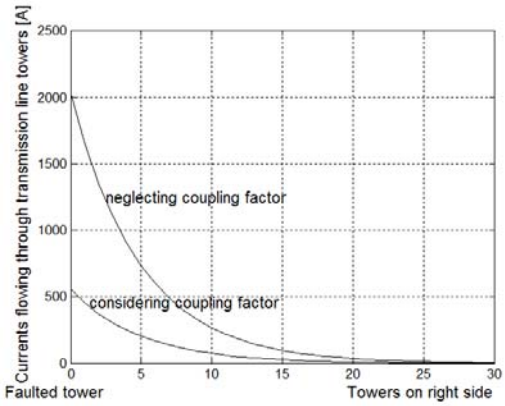

Fig. 7 – Currents flowing through transmission towers as a function of the number of spans.

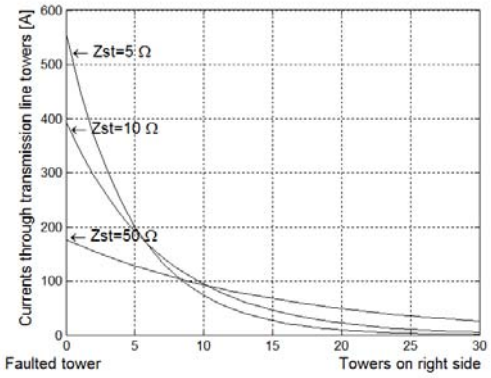

Fig. 8 – Currents through transmission line towers as a function of the number of spans.

Figure 9 presents the currents flowing through transmission towers for different values of the faulted tower impedance. It was considered the case of a finite transmission line and that the fault appears in the middle of the transmission line, and there are 20 towers of each side of the faulted tower.

Figure 10 presents the current through the faulted tower, for a finite line in both directions, as a function of the line length. When the line length exceed a limit, the current remains practically constant with the further increase of the line length.

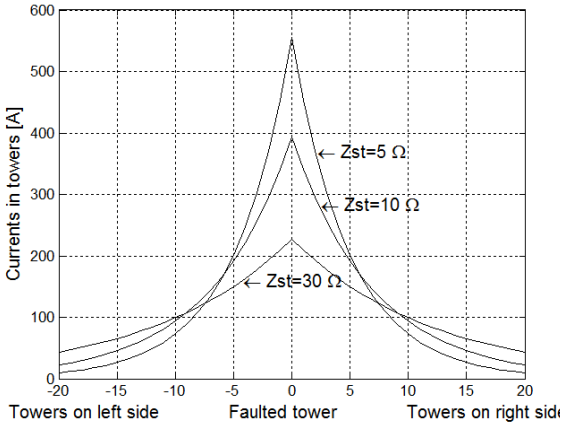

Fig. 9 – Currents flowing through transmission towers for different values of the faulted tower impedance.

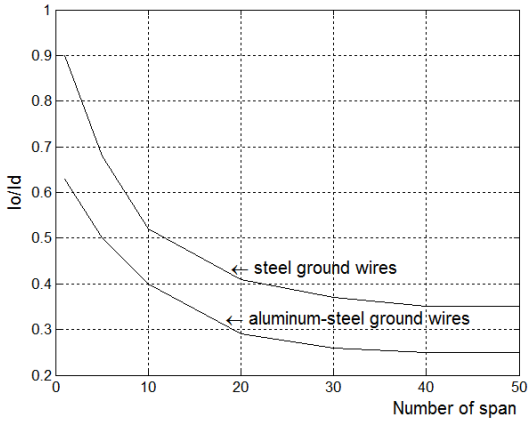

Fig. 10 – The current through the faulted tower as a function of the line length.

In order to validate the analytical expressions, their corresponding results were compared with those measured in similar conditions using real fault tests [3] or with those obtained using other recognized analytical methods [5, 8, 12, 13]. The obtained computations results are in a good agreement with those obtained from real measurements, respectively with those analytically obtained by other researchers. As important advantages, the presented method is simpler, easily understandable and far less time consuming than others.

6. CONCLUSIONS

At first was considered an overhead transmission line with one ground wire, connected to the ground at every tower of the line. But, quite often there are more than one ground wire installed on the transmission line. Additional ground wire reduces the overall series impedance. As a consequence the tower voltages during a ground fault will be lower than in the case of a single ground wire. Considering two ground wires, the method and equations presented for single ground wire can be still applied, but in equations for the self and mutual impedances of the two ground wires, the mutual coupling between the two ground wires must be

taken into consideration [4]. The mutual impedance between the ground conductor and the faulted phase conductor, reduces the total circuit impedance. In these conditions, the fault current will be higher if the mutual impedance is neglected. It also can be seen that in the absence of mutual coupling, the fault current will flow through the ground, through a smaller number of towers then in the mutual coupling presence. The method can be used for the design of new transmission lines in order to select the size of the ground wire, for evaluating safety conditions near transmission towers, etc.

REFERENCES

1. CARSON J. R., *Wave propagation in Overhead Wires with Ground Return,* Bell System Techn., **5**, *1*, 1926.
2. CLARKE E, *Power System Circuits Analysis* (in Romanian), Edit. Academiei, Bucharest, Romania, 1979.
3. DAWALIBI F., NILES G. B., *Measurements and Computations of Fault Current Distribution on Overhead Transmission Lines,* IEEE Transactions on Power Apparatus and Systems, **PAS-103**, *3*, 1984.
4. ENDRENYI J., *Paper's Analysis of Transmission Tower Potentials during Ground Faults,* IEEE Transactions on Power Apparatus and Systems, **PAS-86**, *10*, 1967.
5. GOCI H. B., SEBO S. A., D*istribution of Ground Fault Currents along Transmission Lines – an Improved Algorithm,* IEEE Transactions on Power Apparatus and Systems, **PAS-104**, *3*, pp. 663–669, 1985.
6. Li C., Wei X., Li Y., DAWALIBI F., *A Parametric Analysis of Fault Current Division between Overhead Wires and Substation Grounding Systems*, Proceedings of the Seventh IASTED International Conference on Power and Energy Systems, Clearwater Beach, FL, USA, November 28 – December 1, 2004.
7. *** *Methodology of Current Fault Calculus in Electrical Networks* (in Romanian), PE 134/1984, Electrical Research and Development (ICEMENERG), Bucharest, Romania, 1993.
8. POPOVIC L. M., *Practical method for evaluating ground fault current distribution in station, towers and ground wire,* IEEE Trans. On Power Delivery, **13**, *1*, pp. 123–128, 1998.
9. RACHIDI F., *Transient Analysis of Multiconductor Lines Above a Lossy Ground*, IEEE Transactions on Power Delivery, **14**, *1*, 1999.
10. RUDENBERG R., *Transient Performance of Electric Power Systems* (in Romanian), Edit. Academiei, Bucharest, Romania, 1959.
11. SAAD O., *A Closed-Form Approximation for Ground Return Impedance of Underground Cables*, IEEE Transactions on Power Delivery, **11**, *3*, July 1996.
12. SEBO S. A., *Zero Sequence Current Distribution Along Transmission Lines,* IEEE Transactions on Power Apparatus and Systems, **88**, 1969.
13. VERMA R., MUKHEDKAR D., *Ground Fault Current Distribution in Sub-Station, Towers and Ground Wire,* IEEE Transactions on Power Apparatus and Systems, **PAS- 98**, *3*, 1979.
14. VINTAN M., BUTA A., *Ground fault current distribution on overhead transmission lines,* Facta Universitatis (NIS) – Electronics and Energetics, **19**, *1*, 2006.
15. VINTAN M., *Evaluating transmission towers potentials during ground fault,* Journal of Zhejiang University Science A, Zhejiang University Press (co-published with Springer Verlag GmbH), **9**, *2*, pp. 182–189, 2008.
16. VINTAN M., *About the Coupling Factor Influence on the Ground Fault Current Distribution on Overhead Transmission Lines,* Advances in Electrical and Computer Engineering, **10**, *2*, pp. 43–48, 2010.

Received August 1, 2012

THE PUBLISHING HOUSE
OF THE ROMANIAN ACADEMY

PROCEEDINGS OF THE ROMANIAN ACADEMY, Series A,
Volume 15, Number 3/2014, pp. 262–271

PASSIVE MITIGATION SOLUTIONS USING EXPLICIT DYNAMICS SIMULATION

Iuliana-Florina CIORTAN [1], Ioan-Tiberiu GIURGIU [1], Cristina PUPĂZĂ [2]

[1] Military Equipment and Technologies Research Agency, Clinceni, Romania
[2] "Politehnica" University of Bucharest, Romania
E-mail: cristinapupaza@yahoo.co.uk

The paper presents the results of a research on armor plates behavior subjected to shock waves generated by a TNT blast on the soil surface. The main objective was to propose passive solutions to mitigate the effects of the explosions by means of perforated plates made by composite materials. Simulations using ANSYS AUTODYN and explicit dynamics procedures were performed on several models, with different material configuration, in order to find an optimal distribution and a good protection against the shock wave effects. The second aspect that was taken into account was the weight of the models, in order to decrease the mass of the armor plates. Simulation results were checked and appropriate solutions were found.

Key words: simulation, blast, passive mitigation, composites, explicit dynamics.

1. INTRODUCTION

Over the past years, both the violence and the terrorist attacks have been on the rise. There is a wide variety of protective defense systems available but, faced with the complexity of the equipment and of the materials it is a tough job for scientists to find counter threats solutions and appropriate protection systems. Statistical data [1], obtained in the context of the modern war, provide information which represents a strong motivation for scientists towards reducing the vulnerability of the society to bomb attacks.

Military armed vehicle with increased mobility, great protection capacity and minimum weight, represent the main concern of the researchers in the domain of the protection of the vehicle hull by the shock waves effects and interaction.

Recommendations regarding the soft condensed materials for blast mitigation using a simplified approach are found in published papers [2], but this analysis is confined to some abnormal effects and suggestions are done for future research in this area. The development of a blast simulation environment, intended to be used, was also tested on Biomimetic Tendon-Reinforced models [3]. A multinomial regression statistical model was developed [4] for structural modifications and a number of alterations were performed in order to explore these effects. This study used clinical data to detail the effects of configuration changes on vehicle occupant survival, and as such, can be used for future blast mitigation measures. Although recent results were published and discussed [5, 6, 7], they refer only to theoretical and reduced models, or provide solutions for a specific case. We applied a simulation driven method to find the appropriate configuration for passive mitigation systems based on layered composites. The study was performed on real scale models, using a commercial solver and aiming a reasonable computational time.

2. ATTENUATION OF THE EXPLOSION EFFECTS

The use of Improvised Explosive Devices (IED) as means for destruction has grown-up the interest in improving the resistance of the military structures against blast effects [8]. Active measures are those which need to be deployed in response to a blast event.

a) open cell foam b) closed cell foam c) multilayer lattice truss d) prismatic corrugated core

Fig. 1 – Examples of cellular materials used for blast mitigation [10].

After the stimulus action (e.g. mine detonation, IED explosion) the active system must first detect the threat, than activate the appropriate mitigation system. Consequently, the mitigation system must have the capacity to be activated in a very short time after the stimulus attack (e.g. milliseconds). That is why passive mitigation systems are widely used. They are embedded within the structure and do not require a trigger mechanisms for activation. For most blast scenarios, such systems are usually preferred as they do not rely upon the detection and deployment mechanisms, but are always activated [9]. Most of the concepts for the blast mitigation are based on the increase of energy dissipation capabilities of the structure, by using metal foams, or foam-like materials, such as honeycombs and polymers. Fig. 1 shows some examples of cellular materials used for blast mitigation [10].

3. THEORETICAL APROACH REGARDING THE DYNAMIC LOADS OF THE BLAST

3.1. Material models

To model the behavior of composite materials subjected to high speed deformation different elastic-plastic models are available in explicit dynamics solvers. Because the shock effects are the most important, the use of a non-linear equation of state is recommended. One model for KEVLAR-EPOXY was proposed in [11], based on experiments and this model is already included in AUTODYN [12]. Significant hardening was observed. In this case it is necessary to have the stress-strain data obtained from the experiments, so that the plasticity parameters can be calculated. Since the tension tests are usually performed to ultimate failure, this experimental data will also indicate whether or not softening is significant. The equation of state specific to Kevlar-epoxy, using orthotropic parameters C_{ij} is [11]:

$$P = -\frac{1}{9}\cdot\left(C_{11}+C_{22}+C_{33}+2C_{12}+2C_{23}+2C_{31}\right)\varepsilon_{\nu} - \frac{1}{3}\cdot\left(C_{11}+C_{21}+C_{31}\right)\varepsilon_{11}^{\mathrm{d}} - \\ -\frac{1}{3}\cdot\left(C_{12}+C_{22}+C_{32}\right)\varepsilon_{22}^{\mathrm{d}} - \frac{1}{3}\cdot\left(C_{13}+C_{23}+C_{33}\right)\varepsilon_{33}^{\mathrm{d}}, \tag{1}$$

where P is the average stress or pressure, C_{ij} are the stiffness matrix coefficients, ε_v – the volumetric strain and $\varepsilon_{ij}^{\mathrm{d}}$ – the deviator strain components. In this study the Kevlar equation of state (1) was modeled using the orthotropic parameters whose values are shown in Table 1.

When using orthotropic materials, the elastic-plastic behavior of the material is modeled by different material laws. Therefore, IRON-ARMCO (Table 1) and Al5083H116 were described by the Johnson-Cook material model, which is a strain-rate and adiabatic, temperature dependent plasticity model. This is suitable for problems were the strain rates vary over a large range, and the temperature changes due to plastic dissipation, causing material softening. The behavior of the materials under sever dynamic load vary from large plastic deformations up to rupture.

The SOIL is composed of porous particles, among which the most common are the silica particles. The soil properties depend on the degree of compaction, the presence of minerals, and of the moisture. This material was chosen from ANSYS AUTODYN material library, with the default characteristics. The equation of state for sand used in the present work is based on a linear pressure-density relation. The piece-wise linear equation of state is implemented within AUTODYN using up to ten pairs of values for density-pressure parameters. The strength model for sand is based on an isotropic, perfectly plastic, rate independent

yield-surface approximation. The yield stress is assumed to depend explicitly only on the pressure and not on the density of the porous material, following the material properties described in [13].

The AIR was described as ideal gas, with regular characteristics and the blast was defined by the JWL equation of state model for explosive detonation with TNT. $Al_{5083}H_{116}$ and IRON-ARMCO were used for the mitigation plate layers, chosen with their default values from AUTODYN library.

Table 1

Material Data

KEVLAR/EPOXY	
Equation of states : *Orthotropic* Sub-Equation of States : *Polynomial* Stiffness Matrix C11 (kPa) *3.425E+06* C22 (kPa) *1.35E+07* C33 (kPa) *1.35E+07* C12 (kPa) *1.14E+06* C23 (kPa) *1.2E+06* C31 (kPa) *1.14E+06* Shear modulus (kPa) *1E+06* Material axes *X-Y-Z-Space* Reference density (g/cm3) *1.58* Young modulus 11 (kPa) *2.392E+05* Young modulus 22 (kPa) *6.311E+06* Young modulus 33 (kPa) *6.311E+06* Poisons ratio 12 *0.115* Poisons ratio 23 *0.216* Poisons ratio 31 *3.034*	Failure : *Material Stress/Strain* Tensile failure Stress 11 (kPa) *5.00E+04* Maximum Shear Stress 12 (kPa) *1.00E+05* Tensile Failure Strain 11 *0.01* Tensile Failure Strain 22 *0.08* Tensile Failure Strain 33 *0.08* Post Failure Response *Orthotropic* Fail 11 & 11 Only Fail 22 &22 Only Fail 33 & 33 Only Fail 12 & 12 and 11 Only Fail 23 & 23 and 11 Only Fail 31 & 31 and 11 Only Residual shear Stiff. Frac. *0.20*
IRON-ARMCO	
Equation of States : *Linear* Reference density (g/cm^3) *7.83* Bulk modulus (kPa) *1.64E+07* Reference temperature (K) *300* Specific heat capacity (J/kgK) *451.99* Strength : *Johnson-Cook* Shear modulus (kPa) *8E+07*	Yield Stress (kPa) *1.75E+05* Hardening constant (kPa) 3.8*E+05* Hardening exponent *0.32* Strain rate constant *0.06* Thermal softening exponent *0.55* Melting temperature (K) *1811* Failure model : *None*

3.2. General aspects regarding the shock wave-structure interaction

When an explosive charge detonates, an incident shock wave propagates into the surrounding environment, which is initially at rest. After the passage of the shock wave, the physical properties of the air (pressure, temperature, density and velocity of the material particles) are compressed and a discontinuity of the thermodynamic quantities arises. The pressure profile of a shock wave in respect with the time (Fig. 2) is characterized by its incident peak overpressure ΔP^+, the maximum drop value ΔP^-, the time of the arrival t_a, the positive and negative phase durations, t^+ and t^- and its positive and negative pulses I^+ and I^- [14].

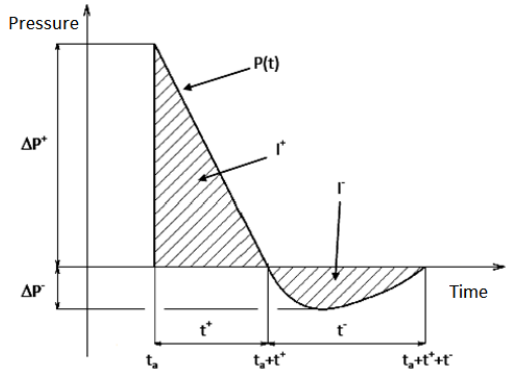

Fig. 2 – Temporal pressure profile of the shock wave [15].

Generally, the pressure profile of a shock wave is characterized by the Friedlander function as:

$$\Delta P(t) = \Delta P^{+}(1-\frac{t-t_a}{t^{+}})\mathrm{e}^{-\alpha\frac{t-t_a}{t^{+}}}, \tag{2}$$

where α is a dimensional parameter depending on the shock wave intensity.

The Jones-Wilkins-Lee (JWL) equation of state model for explosive detonation is given by [16]:

$$P = A\left(1-\frac{\omega}{R_1 V}\right)\mathrm{e}^{-R_1 V} + B\left(1-\frac{\omega}{R_2 V}\right)\mathrm{e}^{-R_2 V} + \frac{\omega E}{V}, \tag{3}$$

where A, B, C, R_1, R_2 and ω are constants calibrated experimentally, V is the product volume relative to the initial explosive volume, E is the energy per unit volume, and P is the pressure. Values for the constants are found in the literature [17].

3.3. Basic formulation of explicit dynamics

The basic equation solved by an explicit dynamic analysis express the conservation of mass, momentum and energy in Lagrange coordinates. These, together with a material model and a set of initial and boundary conditions, define the complete solution of the problem.

For Lagrange formulations, the mesh moves and distorts with the material. The density at any time can be determined from the current volume of the zone V_0 and its initial mass $(\rho_0 V_0)$

$$\rho = \frac{m}{V} = \frac{\rho_0 V_0}{V}. \tag{4}$$

Energy conservation is written as:

$$e = \frac{1}{\rho}\left(\sigma_{xx}\dot{\varepsilon}_{xx} + \sigma_{yy}\dot{\varepsilon}_{yy} + \sigma_{zz}\dot{\varepsilon}_{zz} + 2\sigma_{xy}\dot{\varepsilon}_{xy} + 2\sigma_{yz}\dot{\varepsilon}_{yz} + 2\sigma_{zx}\dot{\varepsilon}_{zx}\right). \tag{5}$$

For each time step, these equations are solved explicitly for each element in the model, based on input values at the end of the previous time step. The explicit dynamics solver uses a central difference time integration scheme – Leapfrog method. The advantages of using this method for time integration are: equations can be solved directly (explicitly), no convergence checks are needed since the equations are uncoupled and no inversion of the stiffness matrix is required [9].

4. CASE STUDIES

In the absence of the similarity laws, which might have simplified the model, the numerical simulation of the armor plates behavior subjected to the dynamic action of the shock waves started with a study on an initial test model (M1). This model was built taking into account the geometry and the working conditions of a military vehicle skeleton. The plate dimensions, the explosive load conditions and the location of the dynamic load, which produces the plate deformation and fracture were chosen using information taken from the literature [16, 18]. The model was checked and tested in order to assure realistic simulation results.

The protection of the vehicle to the action of the shock waves generated by the explosion is highly dependent on the position of the explosive charge to the machine. From this point of view, the worst case has been studied, placing 5 kg of TNT on the soil surface in the center of the plate.

The behavior of an armor plate, called the witness plate was then studied when placing a perforated plate in front of it, at a distance of 200 mm (model M2). As such, the research was focused on how the perforated plate retrieves the dynamic shock waves and dissipates the energy transmitted by the blast.

In order to analyze the behavior of the multilayer perforated plate, two other models were processed and compared (M3 and M4).

4.1. Configuration models

At the beginning a 2D axisymmetric model of the TNT explosion with only soil and air and with a very fine mesh was performed. The initial model (M1) uses the results of the 2D axisymmetric model as an initial

input for air and soil in a 3D model. M1 contains a part filled with AIR (Euler Ideal Gas) and a structural one, IRON-ARMCO – Lagrange type, which represents the witness plate (Fig. 3). The Euler part was filled with soil (SAND) and with TNT in the soil region, where the Improvised Explosion Device (IED) was placed. The symmetry of the model was defined around the X axis, the blue axis in Fig. 3, where the model is plotted rotated with 90 degrees clockwise. Fig. 4 shows the geometry and the material assignment for the model M2, comprising the witness plate and a perforated plate.

The models M3 and M4 were developed with the same 3D configuration, but with a different distribution of the material layers for the perforated plate. Model M3 has a steel perforated plate with a thickness of 6.5 mm and model M4 has two additional layers of aluminum and steel, having a thickness of 11.3 mm both. This aimed to modify the material from which the shield plate is made while maintaining the mass constant. Both M2 and M4 models contain layered structures.

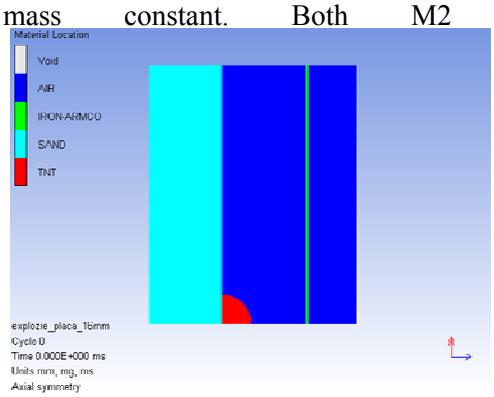

Fig. 3 – Initial 2D model (M1).

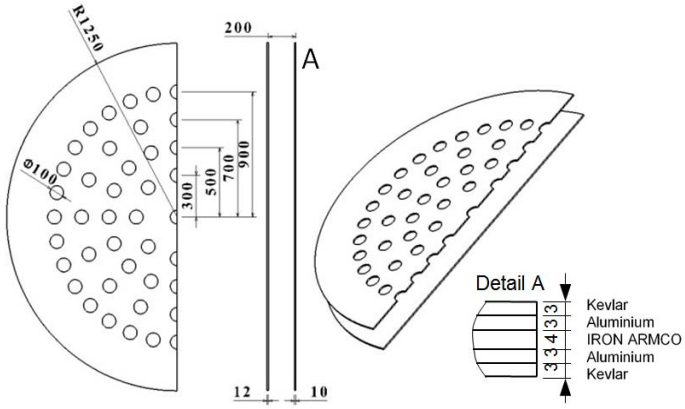

Fig. 4 – Layered model M2.

Fig. 5 shows the multilayered perforated plate (M2) through-out different preparation stages, when AUTODYN options were activated in order to take into account the thickness of the plates. The model preparation of the two plates was performed using a shell technique, which allows a very fine mesh. The element size was less than 1 mm. The true thickness of the plates is shown in Fig. 5 b. Then, an artificial thickness was assigned (Fig. 5 c), where the solver calculates precisely the interaction between the shock wave and the structure, including the passing of the shock wave through the holes of the perforated plates. The TNT explosion was simulated by setting the Boundary conditions. The interaction of the shock wave with the plate was coupled by the Euler-Lagrange Interaction, while the interaction between the two plates

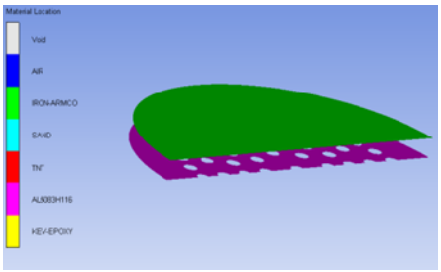

a) shell model

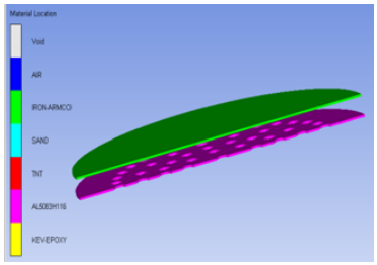

b) real thickness of the plates

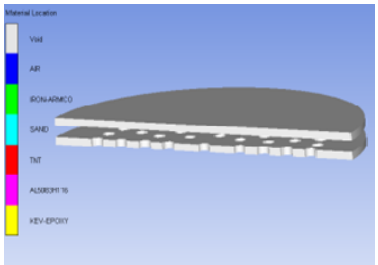

c) artificial thickness of the plates

Fig. 5 – Model of the plates.

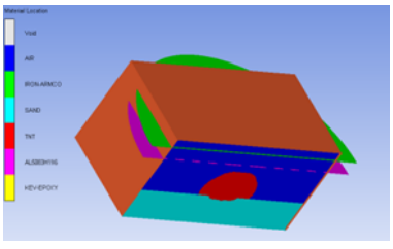

a

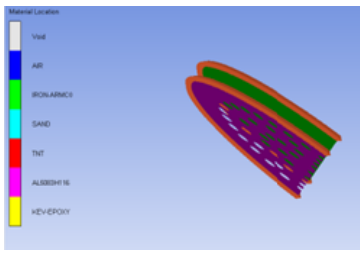

b

Fig. 6 – Boundary conditions.

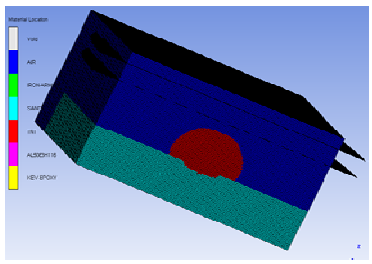

Fig. 7 – FEM model.

was described by Lagrange-Lagrange Interaction. The Flow Out boundary condition (Fig. 6 a) allows the material to pass outside the Euler domain. These conditions were set at a distance of 700 mm from the area of interest. The margins of both the witness and the perforated plate were fixed (Fig. 6 b), preventing the deformation or the movement of the material in that region. The external environment has been modeled by a cube of air.

The FEM model (Fig. 7) comprises more than $2 \cdot 10^6$ elements. In order to reduce the computational time and taking into account the symmetry of the model, only half of the entire structure was calculated. A standard mesh sensitivity analysis was carried out to ensure a proper fine mesh.

4.2. Blast mitigation through numerical simulations

Simulation is widely used in technical sciences, because it helps finding a suitable solution without accessing the optimization procedures, especially when analyzing complex models that involve large computational time. Therefore all the models were subjected to the action of the shock waves generated by the same detonation of the explosive charge and from one model to another the mitigation effect of the explosion was followed.

Figure 8 shows the pressure variation of the shock wave during time, recorded by a gauge placed in the vicinity of the explosion. The mesh inside and around the charge was fine enough to assure a similar pressure profile of the explosion with the theoretical one. This proved that the mesh was properly tuned with the peculiarity of the problem.

First the behavior of the witness plate and the explosion effects were analyzed without a protective plate. Figure 9 shows the evolution of the internal energy during time in this case.

The deformation map of the witness plate, with a maximum displacement of 100 mm along the Z axis in the central aria of the model are plotted in Fig. 10.

The quality and the accuracy of the simulation were further confirmed when comparing the experiments with the simulation results (Fig. 11). The maximum value of the displacements measured during the experiments is around 45 mm (Fig. 11 a), while the computed one was 46.6 mm (Fig. 11 b) for one of the simulation attempts.

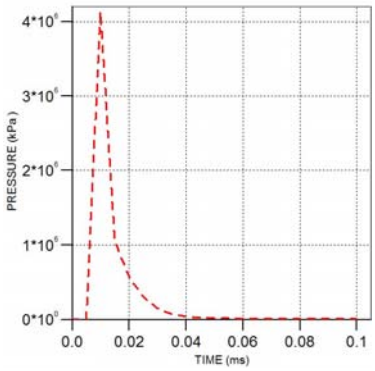

Fig. 8 – Pressure profile of the simulated shockwave.

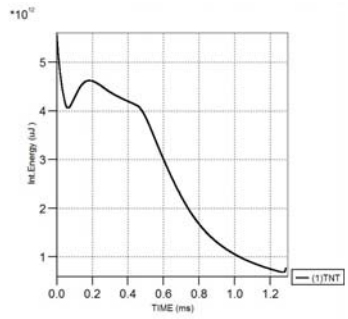

Fig. 9 – Internal energy during time M1.

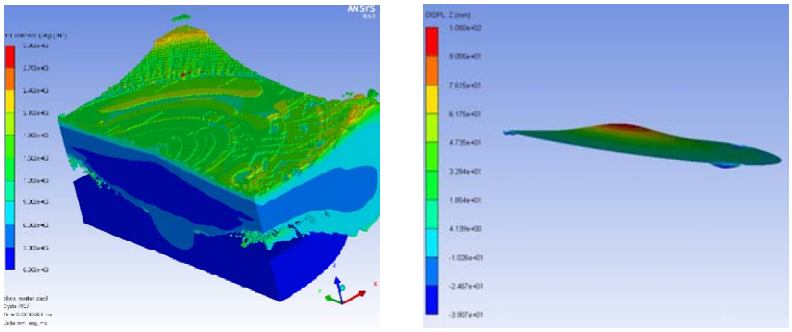

Fig. 10 – Displacements of the witness plate M1.

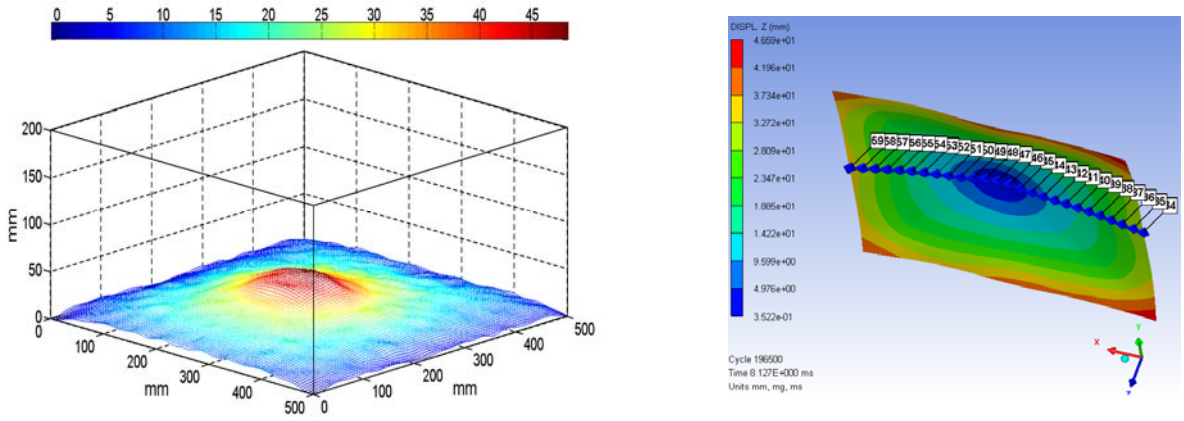

a) displacements obtained during experiments b) simulation results

Fig. 11 – Experiments vs. simulation results.

Theoretical reasons [19] and preliminary practical remarks determined us to focus the research on the following aspects: the strain development and the fracture phenomena, the energy dissipation of the shock wave and the analysis of the loading that arise due to the overpressure in the shock wave.

The displacement map of the protection plate for the three studied models is shown in Fig. 12. The common denominator of all the studied models was the weight of the plates. Taking into account the real conditions in which a passive mitigation system works, the preservation of the total weight or even the possibility to decrease the weight was pursued. The resulting steel protective plate (M2) was found to be even thinner than for the other models (M3 and M4). The behavior of this last configuration is also presented in Fig. 12.c, together with the previous 2 models.

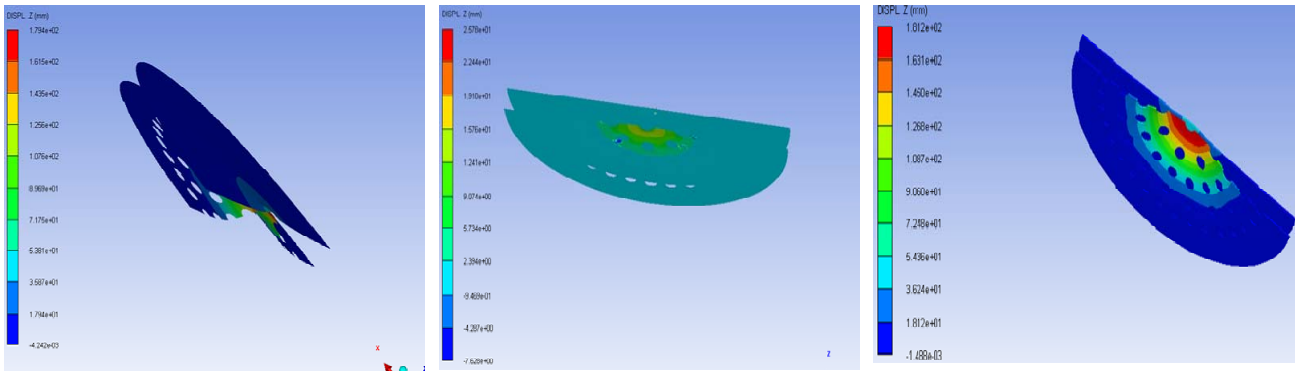

a) model M2 b) model M3 c) model M4

Fig. 12 – Displacements of the perforated plate.

The internal energy plots of the explosive (Fig. 13 and Fig. 14) show the dissipation of the energy after the interaction with the perforated plate for model M2 and M4, proving that the time while the explosion interacts with the plate structure was significantly reduced as the result of introducing the perforated plate, from an initial value of 0.5 ms (M1) to 0.25 ms (M2). Because the structure of the perforated plate of model M3 collapsed (Fig. 12 b) no further processing of the results for this model was performed.

The maximum values of the displacements of the armor plate are shown in Fig. 14. The simulations proved that introducing a perforated plate, improves the behavior of the mitigation model both by the protective qualities of the material, as well as by a gainful effect of the plate pattern.

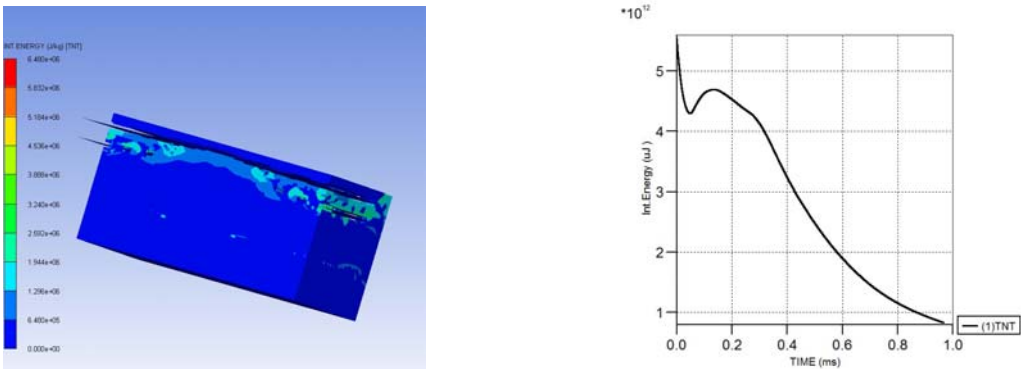

a) 3D plot of the internal energy b) internal energy during time

Fig. 13 – Internal energy plot of the explosion – model M2 and M4.

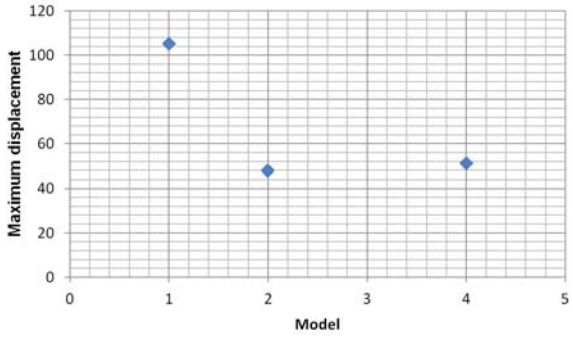

Fig. 14 – Maximum displacements of the models.

5. CONCLUSION

The objective of the paper was to present a simulation driven method to find the appropriate material configuration for a passive blast mitigation system, using a commercial solver and a reasonable computational time.

The effects of the shock wave on four real-scale models, having different material configuration for the perforated plates have been studied by means of explicit dynamic simulations. The four models were named as: M1 – initial model, M2- multilayered perforated plate, M3 – perforated plate made by steel and M4 – two layered perforated plate. Comparing all the studied cases, conclusions regarding the best layout of the passive mitigation system have been drawn. All the simulations were performed on real scale models, tailored to a military vehicle skeleton.

The use of perforated protective plates proved to be a good solution to mitigate the effects of the shock waves caused by a blast. Using composite materials, the requirement of an optimal total weight can be fulfilled, as well as an increase in the energy dissipation.

The explicit dynamic simulation led to the following concluding remarks:

- The numerical simulation of the phenomenon of the interaction between the shock waves generated by the detonation of explosive charges and the structure of the metal plates is a complex procedure that requires computing time and high hardware capabilities.
- The lack of the similarity laws led to the idea of creating different models. Comparing their behavior, practical solutions to mitigate the effect of the explosion were found.
- The quality and the accuracy of the finite element model was validated by means of experiments (Fig. 11).
- After analyzing the results of the theoretical models and numerical simulations, the multilayer composite plate was found as a good solution to mitigate the effects of the explosion. In this case the amount of energy transferred to the base plate was significantly decreased (Fig. 13), and the deformation of the base plate was reduced to the half (Fig. 14).
- The explicit dynamics study was performed on real scale models, apart other studies found in recent literature. This allowed a precise comparison with the experimental data.

• The fixed distance of 200 mm between the perforated plate and the witness plate was imposed by the ground clearance of the vehicle. Since the geometrical constraints of the vehicle in the vertical plane were taken into account, it is assumed that the model is accurate and does not need to be optimized from this point of view.

• The dynamic simulation for the last model (M4) provided similar results with the model M2 (Fig. 13) until the simulation was stopped, at 1 ms. In order to take into account the formation of the soil secondary fragments and to study the model behavior subjected to the shock waves after the appearance of large plastic strains further explicit dynamics simulations, mathematical developments and analytical calculations are still required.

6. FUTURE WORK

In order to take into account the formation of the soil secondary fragments and to study the model behavior loaded by the shock waves after the appearance of large plastic strains further explicit dynamics simulations will be performed.

The action of the shock waves generated at the detonation of the explosive charges depends on the external environment conditions and the characteristics of the explosive material. Including real engineering data for the TNT and more precise soil characteristics may improve the simulation capabilities. Therefore, further simulations can provide important results from this point of view, as well.

The geometry of the protective plate has a great influence on the mitigation effects of the explosions. In the same time, the position of the protective plate, according to the position of the witness plate, and on the location of the IED's are also important factors that determine the behavior of the base plate and may be studied in an optimization parameterized study in the future.

The study encourage the use of computer simulation for conceiving passive mitigation solutions in order to avoid expensive, dangerous and time consuming experiments.

REFERENCES

1. CALDWELL John, *Understanding the Basics of Improvised Explosive Devices* (IED), Civil-Military Fusion Centre (CFC), September 2011.
2. NESTERENKO Vitali, *Shock (Blast) Mitigation by "Soft" Condensed Matter*, MRS Symp. Proceedings, **759**, pp. MM4.3.1–4.3.12, Pittsburgh, 2003.
3. JIANG Dongying, LIU Yuanyuan, QI Chang, MA Zeng-Dong, RAJU Basavaraju, BRYZIKWalter, *Innovative Composite Structure for Blast Protection*, SAE International, 2007-01-0483, Detroit, Michigan, 2007.
4. RAMASAMYA Arul, HILL Adam M., MASOUROSA Spyridon D., GORDONB Fabiana, CLASPERA Jon C., BULLA Anthony M.J., *Evaluating the effect of vehicle modification in reducing injuries from landmine blasts*. An analysis of 2212 incidents and its application for humanitarian purposes, Accident Analysis and Prevention, **43**, pp. 1878–1886, 2011.
5. CHIAN-FONG Yen, JONES M.L., *Composite Material Modeling For Blast Protection*, March 1997.
6. LI Renfu, KARDOMATEAS George, SIMITSES George, *Point-wise impulse (blast) response of a composite sandwich plate including core compressibility effect*, International Journal of Solids and Structures, **46**, *10*, pp. 2216–2223, 2009.
7. RIEDEL W., Harwick W., White D.M., Clegg R.A., *Advanced Material Damage Models for Numerical Simulation Codes*, EMI-Report No. I 75/03, ESA CR(P) 4397, October 2003.
8. RANDAL C., *Improvised explosive device defeat*, FMI 3-34.119/MCIP 3-17.01, September 2005.
9. LANGDON G.S., NURICK G.N., BALDEN V.H., TIMMIS R.B., *Perforated Plates as Passive Mitigation Systems*, Defense Science Journal, **58**, *2*, pp. 238–247, March 2008.
10. WADLEY H.N.G., DHARMASENA K.P., HE M.Y., MCMEEKING R.M., EVANS A.G, BUI-THANH, RADOVITZKY T.R., *Active Concept for Limiting Injuries Caused by Air Blast*, International Journal of Impact Engineering. **37**, pp. 317–323, 2010.
11. HAYHURST Colin, HIERMAIER Stefan, CLEGG Richard, RIEDEL Werner, LAMBERT Michel, *Development of Materials Models for Nextel and Kevlar-Epoxy for High Pressure and Strain Rates*, Hypervelocity Impact Symposium, 1999.
12. *** *Composite Modelling*, Revision 1.3, Release 12.1, AUTODYN®, ANSYS Inc., November 2009.
13. LAINE, L, SANDVIK, A., *Derivation of Mechanical Properties for Sand*, Proceedings of the 4th Asia-Pacific Conference on Shock and Impact Loads on Structures, CI-Premier PTE LTD, Singapore, November 2001, pp. 361–367.
14. DRAGON André, HILD François, ROTA Laurent, TRUME Hervé, *Modélisation du comportement et de la rupture des matériaux sous sollicitations dynamiques*, Revue Mécanique et Industries, **1**, *5*, pp. 521–537 ; DOI : 10.1016/S1296-2139(00)01057-5, Septembre 2001.
15. SAUVAN Pierre-Emmanuel, *Etude des phénomènes physiques associés à la propagation d'ondes consécutives à une explosion et leur interaction avec des structures, dans un environnement complexe*, École Doctorale Sciences et Technologies, 17 octobre 2012.

16. FIŠEROVÁ Darina, *Numerical Analyses of Buried Mine Explosions with Emphasis on Effect of Soil Properties on Loading*, PhD Thesis, Cranfield University, January 2006.
17. THIEL V.M., LEE E.L., COCHRAN S., *Effects of overdriven shock states on the equation of state of 9404 explosive*, Journal of Applied Physics, **54**, *11*, pp. 6760–6763, 1983.
18. SHOWICHEN Adisak, *Numerical analysis of vehicle bottom structure subjected to anti-tank mine explosions*, PhD Thesis, Cranfield University, May 2008.
19. MOLIMARD J., *Mécanique des Matériaux composites*, EMSE, Version 2, Septembre 2004.

Received October 22, 2013

THE PUBLISHING HOUSE
OF THE ROMANIAN ACADEMY

PROCEEDINGS OF THE ROMANIAN ACADEMY, Series A,
Volume 15, Number 3/2014, pp. 272–282

THE ELECTROMECHANICAL IMPEDANCE METHOD FOR STRUCTURAL HEALTH MONITORING OF THIN CIRCULAR PLATES

Cristian RUGINA[1], Adrian TOADER [2], Victor GIURGIUTIU [2,3], Ioan URSU [2]

[1] Institute of Solid Mechanics of the Romanian Academy
[2] "Elie Carafoli" National Institute for Aerospace Research (INCAS)
[3] University of South Carolina, Columbia, SC 29208, USA
e-mail: rugina.cristian@gmail.com

This paper describes the electro-mechanical (E/M) impedance method applied to structural health monitoring (SHM) of thin circular plates. The method allows us to identify the local dynamics of the structure directly through the E/M impedance signatures of piezoelectric wafer active sensors (PWAS) permanently mounted to the structure. An analytical model for 2-D thin-wall structures, which predicts the E/M impedance response at PWAS terminals, was developed and validated. The model accounts for axial and flexural vibrations of the structure and considers both the structural dynamics and the sensor dynamics. Calibration experiments performed on circular thin plates with centrally attached PWAS show that the presence of a damage modifies the high-frequency E/M impedance spectrum causing frequency shifts, peak splitting, and appearance of new harmonics. Comparisons between the analytical method, the finite element method, and experiments were performed, with a fabricated structural arc-shape defect.

Key words: structural health monitoring, electro-mechanical impedance method, piezoelectric wafer active sensors, circular thin plate.

1. INTRODUCTION

The active SHM sensing techniques are based on two different approaches: transient guided waves and standing waves [1, 2]. In such SHM processes, a PWAS is required to generate elastic waves. These travel along the mechanical structure, are reflected by different structural abnormalities, or boundary edges, and then are recaptured by the same sensor in a pulse-echo configuration or by other sensors of same or different type, even passive sensors, in pitch-catch configuration [1]. If the structural damage or boundary edges are in the close vicinity of the active sensor, their reflections overlap the incident transient wave, making impossible the interpretation. This drawback can be overpassed by using the ultrasonic standing waves, in the so-called electromechanical impedance (E/M) method [1, 2]; by sweeping the frequency of the input signals to PWAS, some changes appear in the impedance, measured by an impedance analyzer connected to the PWAS terminals. By monitoring the changes in the real part of the impedance function, which is most sensitive to structural changes, one can evaluate the integrity of the host structure.

It is worthy of note that the SHM, vibration and fatigue control, flutter suppression, gust load alleviation, maneuvers load alleviation and optimization of adaptive wing structures, all together compose an inventory of technologies, attentively evaluated in the framework of the ambitious EU project CleanSky SFWA (CleanSky – Smart Fixed Wing Aircraft, Integrated Technology Demonstrator – ITD, Seventh Framework Programme, see http://www.cleansky.eu), having INCAS Cluster as Associate Partner (see http://www.incas.ro and [3, 4]).

This paper describes a unitary and self-contained mathematical modeling and analytical solution for the E/M impedance of a circular aluminum plate, PWAS instrumented. This approach serves as a reference point for extending the method to other models with unusual geometries. Further, are presented, for comparison, the simulation of the analytical solution, followed by numerical solution based on finite element method. Finally, the two solutions, analytical and numerical, are compared with experimental results, measured on aluminum disks, with and without a laser fabricated defect.

2. ANALYTICAL SOLUTION OF E/M IMPEDANCE FOR A CIRCULAR PLATE

The classical differential equation of motion for the transverse displacement w of a plate is [5]:

$$D\nabla^4 w + \rho h \frac{\partial^2 w}{\partial t^2} = 0,\ D = \frac{Eh^3}{12\left(1-\nu^2\right)}, \tag{1}$$

where: D is the transverse (flexural) rigidity, E is Young's modulus, h is the plate thickness, ν is Poisson's ratio, ρ is mass density per unit area of the plate, t is time, and $\nabla^4 = \nabla^2\nabla^2$, where ∇^2 is the Laplace operator.

2.1. General solution for flexural vibration of a circular plate

The study of the flexural vibration of circular plates has a rich history comprising works and classical studies, e.g., [6]. Some of the main results in the field will be inventoried in the following. Assuming time harmonic vibrations and taking polar coordinates (r, θ), the space and time dependencies will be considered as separated and thus the displacement is expressed in the form:

$$w(r, \theta, t) = \hat{w}(r, \theta)\mathrm{e}^{\mathrm{i}\omega t}. \tag{2}$$

The problem is to find the space-dependent solution $\hat{w}(r, \theta)$ such that it satisfies the differential equation (1) and certain boundary conditions. Equation (1) becomes, after factorization:

$$\left(\nabla^2 + \gamma^2\right)\left(\nabla^2 - \gamma^2\right)\hat{w} = 0,\ \gamma^4 = \frac{\rho h}{D}\omega^2,\ \nabla^2 = \frac{\partial^2}{\partial r^2} + \frac{1}{r}\frac{\partial}{\partial r} + \frac{1}{r^2}\frac{\partial^2}{\partial \theta^2}. \tag{3}$$

The complete solution to equation (3) is obtained by superposition of the solutions of the system:

$$\left(\nabla^2 + \gamma^2\right)\hat{w}_1 = 0,\ \left(\nabla^2 - \gamma^2\right)\hat{w}_2 = 0. \tag{4}$$

The solution of equation (1) is searched in the general Fourier form:

$$\hat{w}(r, \theta) = \sum_{n=0}^{\infty} W_n(r)\cos n\theta + \sum_{n=0}^{\infty} W_n^*(r)\sin n\theta. \tag{5}$$

The substitution of equation (5) into equations (4) gives:

$$\frac{\mathrm{d}^2 W_{1_n}}{\mathrm{d}r^2} + \frac{1}{r}\frac{\mathrm{d}W_{1_n}}{\mathrm{d}r} - \left(\frac{n^2}{r^2} - \gamma^2\right)W_{1_n} = 0,\ \frac{\mathrm{d}^2 W_{2_n}}{\mathrm{d}r^2} + \frac{1}{r}\frac{\mathrm{d}W_{2_n}}{\mathrm{d}r} - \left(\frac{n^2}{r^2} + \gamma^2\right)W_{2_n} = 0, \tag{6}$$

and two other similar equations for W_n^*. Equations (6) are Bessel equations [7] having solutions:

$$W_{1_n} = A_n J_n(\gamma r) + B_n Y_n(\gamma r),\ W_{2_n} = F_n I_n(\gamma r) + G_n K_n(\gamma r), \tag{7}$$

where J_n and Y_n are the Bessel functions of the first and second kind and order n, whereas I_n and K_n are the modified Bessel functions of the first and second kind and order n [7]. The coefficients A_n, B_n, C_n, D_n are found by the imposition of the boundary and initial conditions. The general solution of equation (3) is:

$$\begin{aligned}\hat{w}(r, \theta) = &\sum_{n=0}^{\infty}\left[A_n J_n(\gamma r) + B_n Y_n(\gamma r) + F_n I_n(\gamma r) + G_n K_n(\gamma r)\right]\cos n\theta + \\ &+\sum_{n=0}^{\infty}\left[A_n^* J_n(\gamma r) + B_n^* Y_n(\gamma r) + F_n^* I_n(\gamma r) + G_n^* K_n(\gamma r)\right]\sin n\theta.\end{aligned} \tag{8}$$

However, the Bessel functions $Y_n(\gamma r)$ and $K_n(\gamma r)$ have infinite values at $r=0$ and are discarded (unless the plate has a hole around $r=0$, which is not the case considered here). This means, for solid plates without a central hole, the terms of equation (8) involving $Y_n(\gamma r)$ and $K_n(\gamma r)$ are discarded because they become unbounded at $r=0$. In addition, if the boundary conditions have some symmetry with respect to at least one diameter, then the terms in $\sin n\theta$ are not needed. Where these assumptions are employed, equation (8) simplifies to [5] ($n=0,1,\ldots$ represents the number of nodal diameters):

$$W_n = \left[A_n J_n(\gamma r) + F_n I_n(\gamma r)\right]\cos n\theta . \tag{9}$$

2. 2. Flexural vibration of free circular plates

Consider the volume $\mathrm{d}V = h\,r\,\mathrm{d}r\,\mathrm{d}\theta$ of a differential element in cylindrical coordinates. Bending and twisting moments $M_r, M_\theta, M_{r\theta}, M_{\theta r}$ are related to the flexural displacement *w* by [5]:

$$M_r = -D\left[\frac{\partial^2 w}{\partial r^2} + \nu\left(\frac{1}{r}\frac{\partial w}{\partial r} + \frac{1}{r^2}\frac{\partial^2 w}{\partial\theta^2}\right)\right],\ M_\theta = -D\left[\frac{1}{r}\frac{\partial w}{\partial r} + \frac{1}{r^2}\frac{\partial^2 w}{\partial\theta^2} + \nu\frac{\partial^2 w}{\partial r^2}\right],$$
$$M_{r\theta} = M_{\theta r} = -(1-\nu)D\left[\frac{1}{r}\frac{\partial^2 w}{\partial r\partial\theta} - \frac{1}{r^2}\frac{\partial w}{\partial\theta}\right]. \tag{10}$$

Transverse shearing forces Q_r, Q_θ are related to the flexural displacement, *w*, in the form:

$$Q_r = -D\frac{\partial}{\partial r}\left(\nabla^2 w\right),\ Q_\theta = -D\frac{1}{r}\frac{\partial}{\partial\theta}\left(\nabla^2 w\right). \tag{11}$$

The Kelvin-Kirchhoff edge reactions in polar coordinates are given by:

$$V_r = Q_r + \frac{1}{r}\frac{\partial M_{r\theta}}{\partial\theta},\ V_\theta = Q_\theta + \frac{\partial M_{r\theta}}{\partial r}. \tag{12}$$

The boundary conditions for a free circular plate of outer radius *a* are:

$$M_r(a) = 0,\ V_r(a) = 0. \tag{13}$$

The substitution of boundary conditions (13) into equations (10), (12), with the use of Eq. (11) yields the characteristic equation [7, p. 10]:

$$\frac{\lambda^2 J_n(\lambda) + (1-\nu)\left[\lambda J_n'(\lambda) - n^2 J_n(\lambda)\right]}{\lambda^2 I_n(\lambda) - (1-\nu)\left[\lambda I_n'(\lambda) - n^2 I_n(\lambda)\right]} = \frac{\lambda^3 J_n'(\lambda) + (1-\nu)n^2\left[\lambda J_n'(\lambda) - J_n(\lambda)\right]}{\lambda^3 I_n'(\lambda) - (1-\nu)n^2\left[\lambda I'(\lambda) - I_n(\lambda)\right]}, \tag{14}$$

where $\lambda = \gamma a$. Itao and Crandall [8] performed a comprehensive numerical solution of eigenvalue roots of the characteristic equation (14) and of the associated mode shapes. The eigenvalues of equation (14) were presented as $\lambda_{j,p}$, where $j=1,2,\ldots$ is the number of *nodal circles* and $p=0,1,\ldots$ is the number of *nodal diameters*. (The case $j=0$ yields a triple root at $\lambda=0$ that corresponds to three rigid-body motion modes of a free plate). The mode shapes were presented in the form:

$$W_{j,p}(r,\theta) = A_{j,p}\left[J_p\left(\lambda_{j,p}\,r/a\right) + C_{j,p} I_p\left(\lambda_{j,p}\,r/a\right)\right]\cos p\theta . \tag{15}$$

A sample of values for the eigenvalue $\lambda_{j,p}$, the mode shape parameter $C_{j,p}$, and amplitude $A_{j,p}$ are given in Itao and Crandall [8]. The mode shapes amplitudes $A_{j,p}$ [10] were found based on the mass-normalization formula and mode shapes orthogonality (*m* is the total mass of the plate and δ_{ij} is the Kronecker delta):

$$\int_0^{2\pi}\int_0^a \rho\, h\, W_{j,p}^2(r,\theta)\, r\mathrm{d}r\mathrm{d}\theta = \rho\pi a^2 h = m,\ \int_0^{2\pi}\int_0^a \rho h W_{j,p} W_{i,q}\, r\mathrm{d}r\mathrm{d}\theta = m\delta_{ij}\delta_{pq}. \tag{16}$$

2. 3. Circular plates: particular case of axisymmetric free flexural vibration

Axisymmetric flexural vibration of a circular plate can be understood in terms of standing circular-crested waves that propagate in a concentric circular pattern from the center of the plate and reflect at the plate circumference. The problem is θ-invariant, i.e. $\partial/\partial\theta = 0$. The general solution (2) is sought in the form:

$$w(r,t) = \hat{w}(r)\mathrm{e}^{\mathrm{i}\omega t}. \tag{17}$$

By substitution in equation (1), the decomposition (3) is retrieved:

$$\left(\frac{\mathrm{d}^2}{\mathrm{d}r^2} + \frac{1}{r}\frac{\mathrm{d}}{\mathrm{d}r} + \gamma^2\right)\hat{w} = 0 \quad \text{or} \quad \left(\frac{\mathrm{d}^2}{\mathrm{d}r^2} + \frac{1}{r}\frac{\mathrm{d}}{\mathrm{d}r} - \gamma^2\right)\hat{w} = 0. \tag{18}$$

Fourier form (5) is no longer present, given the absence of $\theta-$dependence. This is equivalent to $n = 0$ in the equations (8) and thus the general solution for axisymmetric flexural vibration of circular plates has the form

$$w(r,t) = \left[AJ_0(\gamma r) + FI_0(\gamma r)\right]e^{i\omega t}, \tag{19}$$

where $J_0(\gamma r)$ is the Bessel function of first kind and order zero, whereas $I_0(\gamma r)$ is the modified Bessel function of first kind and order zero. The constants are to be determined from the initial and boundary conditions. From the same reasons shown in Section 2.1, the functions $Y_0(\gamma r)$ and $K_0(\gamma r)$ were discarded. Closely following equations (10)-(14), one gets the characteristic transcendental equation:

$$\frac{\lambda^2 J_0(\lambda) + (1-\nu)\lambda J_0'(\lambda)}{\lambda^2 I_0(\lambda) - (1-\nu)\lambda I_0'(\lambda)} = \frac{\lambda^3 J_0'(\lambda)}{\lambda^3 I_0'(\lambda)}, \quad \lambda = \gamma a, \quad \omega_j = \lambda_j^2\sqrt{\frac{D}{\rho h a^4}}. \tag{20}$$

That gives natural frequencies ω_j associated with each eigenvalue λ_j and mode shape. For each eigenvalue, one finds the corresponding mode shape by calculating the constants A and F in the equation (19). The general expression of the mode shape is written using an amplitude A_j and a mode shape parameter C_j, i.e.,

$$W_j(r) = A_j\left[J_0(\lambda_j r/a) + C_j I_0(\lambda_j r/a)\right]. \tag{21}$$

From the normalization relationships (16), one obtains [10]:

$$A_j = \frac{1}{\sqrt{2}}\left\{\left[J_0(\lambda_j) + C_j I_0(\lambda_j)\right]^2 - \left[J_0'(\lambda_j)\right]^2 - \left[C_j I_0'(\lambda_j)\right]^2\right\}^{-\frac{1}{2}}. \tag{22}$$

2.4. Forced axisymmetric flexural vibration of circular plates

Consider the circular plate undergoing axisymmetric flexural vibration under the excitation of an externally applied time-dependent distributed moment $m_e(r,t)$ (Fig. 2.1, left). The units of $m_e(r,t)$ are moment per unit area (e. g., Nm/ m^2). Let ω_j, $W_j(r)$ and A_j described by (20), (21), and (22), respectively.

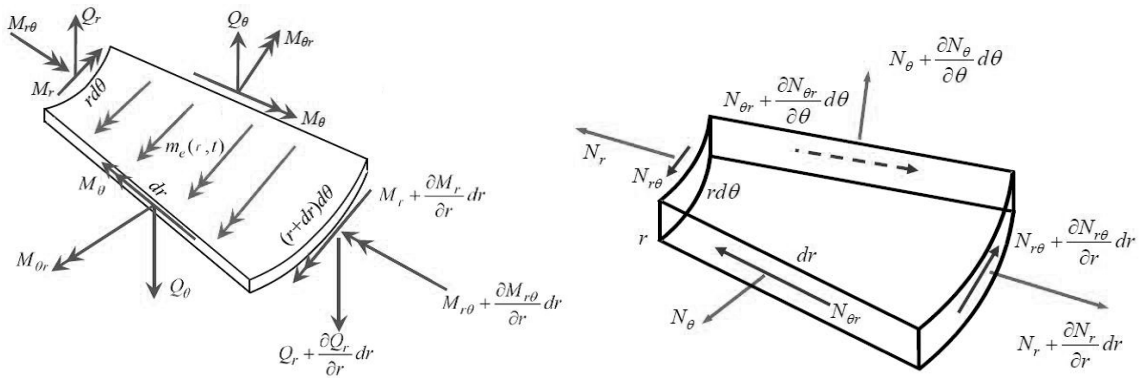

Fig. 2.1 – Circular plate. Left: sketch for flexural vibration analysis; right: sketch for axial vibration analysis.

PROPOSITION 2.1. *The equation of motion for forced vibrations of the circular plate under axisymmetric flexural moment excitation and its solution are:*

$$D\nabla^4 w + \rho h\ddot{w} = \hat{m}_e' + \hat{m}_e / r\,. \tag{23}$$

$$\begin{aligned} w(r,t) &= \frac{2}{\rho h a^2}\sum_{j=1}^{\infty}\frac{f_j}{-\omega^2 + +2i\zeta_j\,\omega\omega_j + \omega_j^2}W_j(r)\,\mathrm{e}^{\mathrm{i}\omega t}, \\ f_j &= a\,\hat{m}_e(a)W_j(a) - \int_0^a \hat{m}_e(r)W_j'(r)r\mathrm{d}r,\ j = 1, 2, 3, \ldots \end{aligned} \tag{24}$$

Proof. For reasons of space, we only sketch the proof. Apply free-body analysis in the *r*-direction to an infinitesimal plate element $r\,\mathrm{d}r\,\mathrm{d}\theta$. Equations for force and moments are obtained in the form $Q_r + r(\partial Q_r/\partial r) = \rho h r\,\ddot{w}$, $r(\partial^2 M_r/\partial r^2) + 2(\partial M_r/\partial r) - (\partial M_\theta/\partial r) + m_e + r(\partial m_e/\partial r) = \rho h r\,\ddot{w}$; substituting of those in (10) gives (23), and assuming both excitation and response are harmonic, we have:

$$m_e(r,t) = \hat{m}_e(r)\,\mathrm{e}^{\mathrm{i}\omega t},\ w(r,t) = \sum_{j=1}^{\infty}\eta_j W_j(r)\,\mathrm{e}^{\mathrm{i}\omega t}\ . \tag{25}$$

The constants η_j are the modal participation factors. Substitution of Eq. (25) into equation (23), division by $\mathrm{e}^{\mathrm{i}\omega t}$, use of natural frequencies ω_i described by the equation $D\nabla^4 W_i - \omega^2\rho_i h W_i = 0$, recalling (16) and deliberate introduction of modal damping ζ_j lead to expressions (24), so completing the proof.

2.5. General solution for the axisymmetric axial vibration of circular plates

Consider the infinitesimal plate element in polar coordinates shown in Fig. 2.1 right. Under the axisymmetric assumption, the wave equation in polar coordinates is:

$$c_L^2\nabla^2 u_r - \ddot{u}_r = 0,\ c_L^2 = E/\left(\rho(1-\nu^2)\right), \tag{26}$$

where c_L is the longitudinal wave speed in plate. Stress-displacement relations of elasticity theory were used, followed by integration of stresses across the thickness and the free-body analysis applied to element Similarly to the approach at the beginning of paragraph 2.1, the displacement u_r is considered harmonic:

$$u_r(r,t) = \hat{u}(r)\,\mathrm{e}^{\mathrm{i}\omega t}\,. \tag{27}$$

Substitution in (26) yields a Bessel equation. Introducing the wavenumber γ, the same considerations as those at the end of paragraph 2.1 lead to the solution:

$$u_r(r,t) = AJ_1(\gamma r)\mathrm{e}^{\mathrm{i}\omega t},\ \gamma = \omega/c_L\ . \tag{28}$$

The constant A, the frequency ω, and the wavenumber γ are determined from the boundary condition $N_r(a)=0$, which means $\left(\frac{\partial u_r}{\partial r}+\nu\frac{u_r}{r}\right)\Big|_{r=a}=0$. Substituting (27) in the last equation and applying standard reasoning, we obtain the characteristic equation, the constant A_n and the mode shapes U_n :

$$zJ_0(z)-(1-\nu)J_1(z)=0,\ A_n=\left(J_1^2(z_n)-J_0(z_n)J_2(z_n)\right)^{-0.5},\ \omega_n=c_L(\gamma a)_n/a,\ U_n(r)=A_nJ_1(\gamma_n r), \tag{29}$$

where $z=\gamma a$, $\gamma_n=c_L(\gamma a)_n/a=z_n/a$. Mode shapes U_n are orthonormal, $\int_0^a U_p(r)U_q(r)r\mathrm{d}r=a^2\delta_{pq}/2$, with respect to weight function r (as for flexural vibrations). Indeed, the afferent Bessel equation is related to a Sturm-Liouville problem: $(rU')'+\left(\gamma^2 r-r^{-1}\right)U=0$, $U_i'(a)+U_i(a)=0,\ i=p,q.$

2.6. Forced axisymmetric axial vibration of circular plates

Consider the circular plate undergoing axisymmetric axial vibration under the excitation of an externally applied time-dependent distributed axial force $f(r,t)$ (Fig. 2.1, left). The units of $f(r,t)$ are force per unit area (e. g., Nm/ m^2). Consider $U_j(r)$, ω_j described by (29).

PROPOSITION 2.2. *The equation of motion for forced axial vibrations of the circular plates under axisymmetric axial force excitation and its solution are, respectively:*

$$c_L^2\nabla^2 u_r-\ddot{u}_r=-\frac{f}{\rho h},u_r(r,t)=\frac{2}{\rho ha^2}\sum_{j=1}^{\infty}\frac{f_j\,U_j(r)\mathrm{e}^{\mathrm{i}\omega t}}{-\omega^2+2i\zeta_j\,\omega\omega_j+\omega_j^2},\quad f_j=\int_0^a\hat{f}(r)U_j(r)r\mathrm{d}r,\ j=1,2,3,.. \tag{30}$$

Proof. A simple application of the free-body analysis in the r-direction to an infinitesimal plate element $r\,\mathrm{d}r\mathrm{d}\theta$ gives the first equation in (30). Further, it is assumed that excitation and response are harmonic $f(r,t)=\hat{f}(r)\mathrm{e}^{\mathrm{i}\omega t}$, $u_r(r,t)=u_r(r)\mathrm{e}^{\mathrm{i}\omega t}$. The substitution of the modal form $\hat{u}(r)=\sum_j U_j(r)\eta_j$, ($\eta_j$ are modal participation factors) in the equation of motion, the use of natural frequencies ω_i and the deliberate introduction of modal damping ζ_j lead to the other two expressions (30).

2.7. The interaction between a circular PWAS and a circular plate. Electromechanical impedance

The E/M method is exemplified in the case of a 2-D PWAS circular modal sensor bonded on a thin isotropic circular plate (Fig. 2.2). The basic concept of the method is to use high frequency structural excitations to monitor the local area of a structure for changes in structural impedance that would indicate imminent damage. This is possible using PWAS sensor/actuators whose electrical impedance is directly related to the structure mechanical impedance. The structural dynamics affects the PWAS response; it modifies the PWAS E/M impedance, measured by an impedance analyzer connected to the PWAS terminals.

It is assumed that the circumferential boundary of the PWAS disc is conditioned by the structure through the dynamic stiffness $k_{str}(\omega)$, which includes both axial and flexural vibration modes. The problem is formulated in terms of interaction line force, F_{PWAS}, and the corresponding displacement, u_{PWAS}, measured at the PWAS circumference. The units of F_{PWAS} are force per unit length (e.g., N/m). The corresponding distributed excitation axial force and flexural moment are expressed as, respectively:

$$f_e(r,t)=\hat{f}_e(r)\mathrm{e}^{\mathrm{i}\omega t}=\hat{F}_{PWAS}\mathrm{e}^{\mathrm{i}\omega t}\delta(r-r_a)/r,\ m_e(r,t)=m_e(r)\mathrm{e}^{\mathrm{i}\omega t}=h\hat{F}_{PWAS}\delta(r-r_a)/(2r). \tag{31}$$

By dividing the Dirac function δ with r, its total effect around a circular circumference does not change when radius changes. Consider ω_{j_u}, $U_{j_u}(r_a)$, ω_{j_w}, $W_{j_w}(r_a)$, described by (29), (20), (21), respectively.

PROPOSITION 2.3. *The dynamic structural stiffness* $k_{str}(\omega)$ *constraining PWAS sensor is given by:*

$$k_{str}(\omega)=\frac{\hat{F}_{PWAS}}{\hat{u}_{PWAS}}=\frac{\rho h a^2}{2}\left[\sum_{j_u}\frac{U_{j_u}^2(r_a)}{-\omega^2+2\mathrm{i}\zeta_{j_u}\omega\omega_{ju}+\omega_{j_u}^2}+\left(\frac{h}{2}\right)^2\sum_{j_w}\frac{W_{j_w}'^2(r_a)}{-\omega^2+2\mathrm{i}\zeta_{j_w}\omega\omega_{j}+\omega_{j_w}^2}\right]^{-1}. \tag{32}$$

Proof. Substitution of the first relation (31) into the last relation (30) gives the modal axial excitation $f_i=\hat{F}_{PWAS}U_j(r_a)$, $j=1,2,\ldots$. Substitution of these expressions into the second equation (30) gives the axial vibration response $u(r,t)=\frac{2}{\rho h a^2}\hat{F}_{PWAS}\sum_{j_u}\frac{U_{j_u}(r_a)}{-\omega^2+2\mathrm{i}\zeta_{j_u}\omega\omega_{j_u}+\omega_{j_u}^2}U_{j_u}(r)\mathrm{e}^{\mathrm{i}\omega t}$ (*). The substitution of the 2nd relation (31) into 2nd relation (24) gives the modal flexural excitation $f_i=-h\hat{F}_{PWAS}W_j'(r_a)/2$, $j=1,2,\ldots$. The substitution of these expressions into the first relation (24) gives finally the flexural vibration response to PWAS excitation $w(r,t)=-\frac{2}{\rho h a^2}\frac{h}{2}\hat{F}_{PWAS}\sum_{j_w}\frac{W_{j_w}'(r_a)}{-\omega^2+2\mathrm{i}\zeta_{j_w}\omega\omega_{j_w}+\omega_{j_w}^2}W_{j_w}(r)\mathrm{e}^{\mathrm{i}\omega t}$ (**). The radial displacement at the edge of the PWAS is of the form $u_{PWAS}(r_a,t)=u(r_a,t)-hw'(r_a,t)$ [9]. Note that $u(r_a,t)$ and $w(r_a,t)$ are the displacements at the plate neutral plan, whereas $u_{PWAS}(r_a,t)$ is measured at the plate upper surface (Fig. 2.2). Discarding the time dependence $\mathrm{e}^{\mathrm{i}\omega t}$, we rewrite this equation in the form $\hat{u}_{PWAS}(r_a)=\hat{u}(r_a)-h\hat{w}'(r_a)/2$. Now, herein substitution of the relations (*), (**) leads to (32).

Now we introduce the concepts and parameters that characterize a circular-shaped PWAS, starting from the piezoelectric constitutive equations in cylindrical coordinates [1, Ch. 7]:

$$S_{rr}=s_{11}^E T_{rr}+s_{12}^E T_{\theta\theta}+d_{31}E_z,\ S_{\theta\theta}=s_{12}^E T_{rr}+s_{11}^E T_{\theta\theta}+d_{31}E_z,\ D_z=d_{31}(T_{rr}+T_{\theta\theta})+\varepsilon_{33}^T E_z, \tag{33}$$

where S_{rr} and $S_{\theta\theta}$ are the mechanical strains, T_{rr} and $T_{\theta\theta}$ are the mechanical stresses, E_z is the electrical field, D_z is the electrical displacement, s_{11}^E and s_{12}^E are the mechanical compliances at zero electric field $(E=0)$, ε_{33}^T is the dielectric permittivity at zero mechanical stress $(T=0)$, and d_{31} is the piezoelectric coupling between the electrical and mechanical variables. Hence, $S_{rr}=\partial u_r/\partial r$ and $S_{\theta\theta}=u_r/r$. Applying Newton law of motion, one recovers the wave equation, with a general solution in terms of Bessel function:

$$\frac{\partial^2 u_r}{\partial r^2}+\frac{1}{r}\frac{\partial u_r}{\partial r}-\frac{u_r}{r^2}=\frac{1}{c_p^2}\frac{\partial^2 u_r}{\partial t^2},\ c_P=\sqrt{\frac{1}{\rho s_{11}^E(1-\nu_a^2)}},\ u_r(r,t)=AJ_1\left(\frac{\omega r}{c_P}\right)\mathrm{e}^{\mathrm{i}\omega t},\ T_{rr}(r_a)=\frac{k_{\mathrm{str}}(\omega)u_r(r_a)}{t_a}. \tag{34}$$

Last equation (34) expresses the boundary condition. The first two equations (33) give:

$$\begin{aligned}&(\partial u_r(r_a)/\partial r)=\chi(\omega)(1+\nu_a)u_r(r_a)/r_a-\nu_a u_r(r_a)/r_a+(1+\nu_a)d_{31}E_z,\\ &k_{PWAS}=t_a/(r_a s_{11}(1-\nu_a)),\ \chi(\omega)=k_{str}(\omega)/k_{PWAS},\ \nu_a=-s_{12}^E/s_{11}^E\end{aligned}. \tag{35}$$

The notations refer to, successively: the static stiffness of the circular PWAS, the dynamic stiffness ratio, and the Poisson's ratio of the piezoelectric material. Intermediary, we determine the coefficient A:

$$A=\frac{(1+\nu_a)r_a d_{31}E_z}{\varphi_a J_0(\varphi_a)-(1-\nu_a)+(1+\nu_a)\chi(\omega)J_1(\varphi_a)},\quad \varphi_a=\frac{\omega r_a}{c_P}. \tag{36}$$

The electrical admittance is calculated as the ratio between the current and the voltage amplitudes, i.e., $Y = \hat{I}/\hat{V}$. The current is calculated by integrating the electric displacement D_z over the PWAS area to obtain the total charge, and then differentiating the result with respect to time, whereas the voltage is calculated by multiplying the electric field by the PWAS thickness t_a . Finally the impedance is expressed as:

$$Z(\omega) = \left\{ i\omega C \left[1 - k_p^2 + \frac{k_p^2}{2} \frac{(1+v_a) J_0(\varphi_a)}{\varphi_a J_0(\varphi_a) - (1-v_a) J_1(\varphi_a) - \chi(\omega)(1+v_a) J_1(\varphi_a)} \right] \right\}^{-1}, k_p^2 = \frac{2d_{31}^2}{s_{11}^E (1-\nu_a) \varepsilon_{11}^E}. \quad (37)$$

The complex compliance and dielectric constant expressions can be considered:

$$\overline{\chi}(\omega) = \frac{k_{str}(\omega)}{\overline{k}_{PWAS}}, \overline{k}_{PWAS} = \frac{t_a}{r_a \overline{s}_{11} (1-\nu_a)}, \nu_a = -\frac{s_{12}^E}{s_{11}^E}, \overline{s}_{11} = s_{11}(1-i\eta), \overline{\varepsilon}_{33} = s_{33}(1-i\delta), \overline{C} = C(1-i\mu). \quad (38)$$

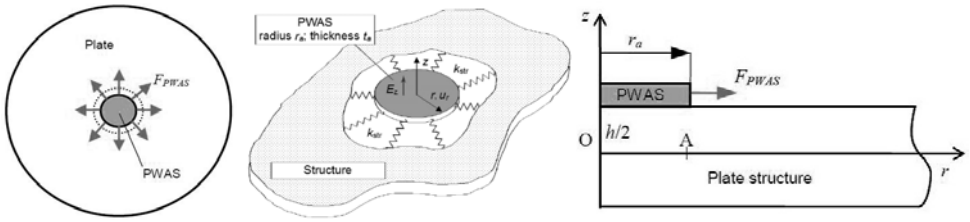

Fig. 2.2 – Circular PWAS constrained by structural stiffness, $k_{str}(\omega)$.

The values of η, δ, μ vary with the piezoceramic formulation of the PWAS material, but are usually small (less than 5%). In this case, we obtain ($\overline{\varphi} = \varphi\sqrt{1-i\eta}$ is also added):

$$Z(\omega) = \left\{ i\omega \overline{C} \left[1 - k_p^2 + \frac{k_p^2}{2} \frac{(1+v_a) J_0(\overline{\varphi}_a)}{\overline{\varphi}_a J_0(\overline{\varphi}_a) - (1-v_a) J_1(\overline{\varphi}_a) - \chi(\omega)(1+v_a) J_1(\overline{\varphi}_a)} \right] \right\}^{-1}, k_p^2 = \frac{2d_{31}^2}{\overline{s}_{11}^E (1-\nu_a) \overline{\varepsilon}_{11}^E} \quad (39)$$

3. EXPERIMENTAL SETUP, NUMERICAL SIMULATION, AND RESULTS

In the experimental setup, the HP 4194A impedance analyzer was used. The chosen geometry for analytical and experimental comparisons is a circular A2024 aluminum plate with a circular Noliac NCE51 PWAS bonded on it (Fig.3.1); the PWAS material is equivalent to the standard PZT-5A material.

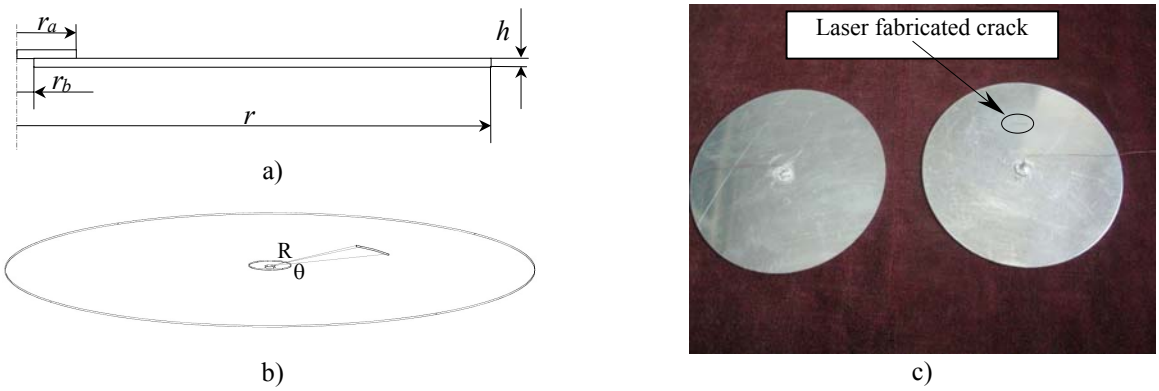

Fig. 3.1 – a) Geometry of the thin plate with central hole and bonded PWAS; b), c) position of the arc-shape crack.

The simulated crack was laser fabricated, in the shape of a circular arc centered on the symmetry center of the plate. Two geometries of the A2024 plates were considered, in FEM simulations, without and with central hole. The central hole was initially used to correctly position the PWAS as centered as possible.

The specimen A2024 with bonded PWAS has the geometry (Fig. 3.1.a,b): r = 50.08mm, h = 0.835mm, r_a = 4mm, r_b = 1mm. The geometry of the simulated crack (0.15mm wide, and 10mm long) is the following (Fig. 3.1a,b): R =25mm, θ = 23°. The adhesive used to bond the PWAS to the A2024 aluminum plate was an electro-conductive epoxy ELPOX15. The thickness of the adhesive layer was measured with a comparator, and was found to be between 20 μm and 100 μm.

The numerical model used in this paper is based on the FEM, and was implemented in the software Comsol 4.3 (Fig. 3.3). A coupled field frequency analysis based on piezoelectric constitutive equations that include structural losses has been taken into consideration, with the following symbol notation:

$$\sigma = \tilde{c}^E \varepsilon - \tilde{e}E, \quad D = \tilde{e}\varepsilon + \varepsilon^0 \tilde{\varepsilon}^r E, \tag{40}$$

in the stress-charge form; σ is the stress matrix, ε denotes strains matrix, D denotes electric charge matrix, $\tilde{c}^E$ denotes the elasticity matrix, $\tilde{e}$ denotes the piezoelectric coupling matrix, $\tilde{\varepsilon}^r$ the relative permittivity matrix, ~ denotes complex values where the imaginary part defines the dissipative function of the material.

The material of the PWAS was taken PZT5A, that belong to the 6 mm class symmetry, which have compliance, piezoelectric coupling, and relative permittivity matrices in the stress-charge form [11]:

$$\begin{gathered} c_{11}^E = c_{22}^E = 120.35\ \text{GPa}, \quad c_{12}^E = 75.18\ \text{GPa}, \quad c_{13}^E = c_{23}^E = 75.09\ \text{GPa}, \quad c_{33}^E = 110.86\ \text{GPa}, \\ c_{44}^E = c_{55}^E = 21.05\ \text{GPa}, \quad c_{66}^E = 22.57\ \text{GPa}, \quad e_{31} = e_{32} = -5.35116\ \text{C/m}^2, \\ e_{33} = 15.7835\ \text{C/m}^2, \quad e_{15} = 12.2947\ \text{C/m}^2, \quad \varepsilon_{11}^r = \varepsilon_{22}^r = 919.1, \quad \varepsilon_{33}^r = 826.6. \end{gathered} \tag{41}$$

The mechanical and piezoelectric structural losses for the PWAS were neglected. However the dielectric losses of 1.9% given by the manufacturer were taken into consideration. The mass density of the piezoceramic material was considered $\rho = 7\,750\ \text{kg/m}^3$. The properties of the A2024 aluminum plates were: $E = 73.146\ \text{GPa}$, $\rho = 2\,780\ \text{kg/m}^3$, $\nu = 0.3312$. The adhesive layer being, as shown previously, have a thickness between 20 μm and 100 μm, and transmits most of the shear forces from the PWAS to the thin plate, and therefore was neglected in some cases and considered to be 100 μm in other cases.

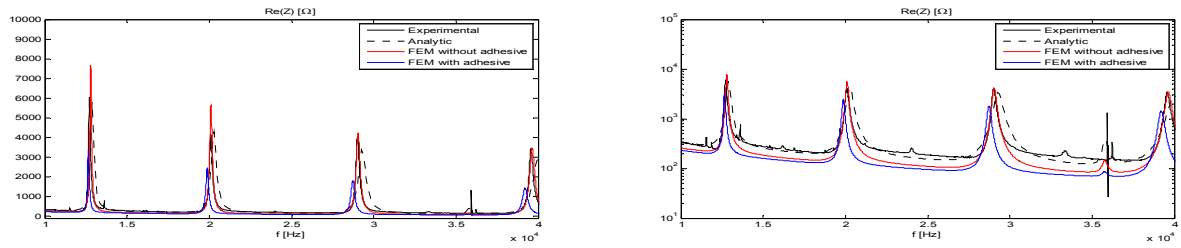

Fig. 3.2 – Real part of the E/M impedance in the case without defect and without central hole: a) in linear scale; b) in logarithmic scale.

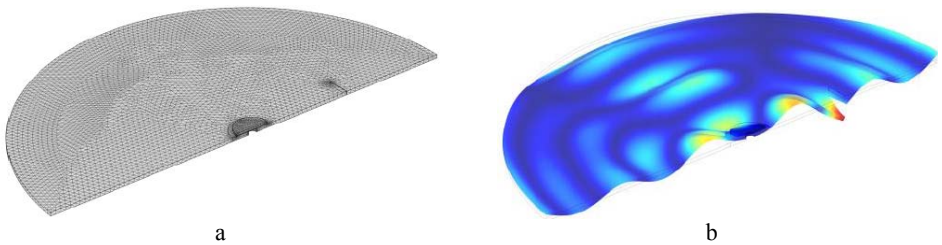

Fig. 3.3 – a) Mesh used in the FEM analysis; b) mode shape of the thin plate with PWAS at 20 kHz, where antiresonance peeks appears, in the case of the defect.

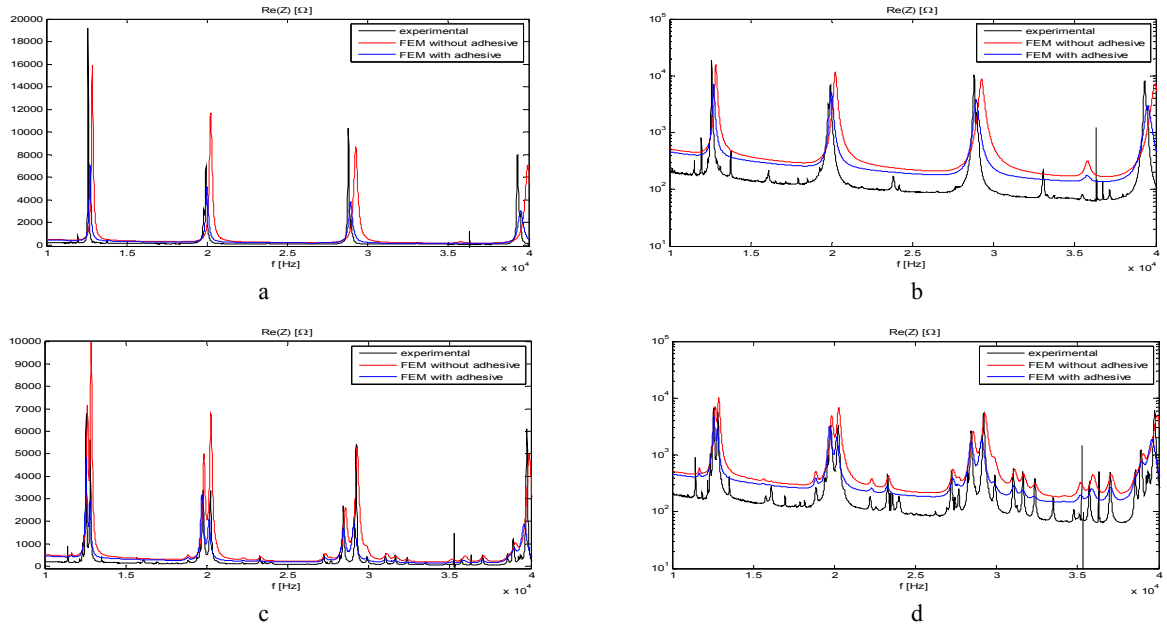

Fig. 3.4 – Re(Z) in the case of thin plate with central hole with bonded PWAS: a), b) without defects, in linear scale (LS), and in logarithmic scale (LogS); c), d) with defect (R = 25mm, θ = 23°), LS and LogS.

Graphics of Re(Z) are presented in Figs. 3.2 and 3.4. It can be seen that the effect of the adhesive layer is not negligible. The FEM analysis shows that there are antiresonance peaks, and the differences are less than 1% in frequency, but larger in amplitude, in the presence of an adhesive layer of 100 μm, compared to the one without adhesive. Because of the axial symmetry, the numerical FEM analysis was done in the 2D axisymmetric mode.

A comparison of the analytic and numerical (FEM) solutions with experiments is done in the frequency range [10kHz, 40kHz] and is given in Fig. 3.2. Analyical solution has input data the geometry and material properties of the A2024 aluminum plate and PWAS. The roots of the characteristic equations (20), (29) are found numerically. The key parameters $\zeta_{j_u} = 0.45\%$ $\zeta_{j_w} = 0.9\%$, $\eta = 2\%$, $\delta = 2\%$ were chosen to match the theoretical results with the experimental data.

Another comparison was made in the case of a plate with central hole, with a laser fabricated crack described above. The presence of central hole is not covered by the theory in this paper, and so the next comparisons were made between experimental data, and FEM analysis with and without adhesive layer. The FEM analyses were done in the 3D mode with XZ symmetry plane; a finer mesh has been taken around the central hole and PWAS, and around the crack (Fig. 3.3.a). Displacements, mode shape of the thin plate with bonded PWAS and with the considered defect at 20 kHz can be seen in Fig. 3.3.b.

It no defect is present, only one antiresonance peek is present. When the defect is present, many antiresonance peeks, appear (Fig. 3.4), visible on the linear scale. From the logarithmic scale, it can be seen that FEM computations follow, also, the smaller peeks that are not easy to observe on the linear scale. It can be seen that an ideal adhesive layer of 100μm, with parallel faces, taken in FEM computations change significantly the shape of the E/M signature. But in real cases, the position of the PWAS is not perfectly parallel to the plate surface, nor perfectly centred, the adhesive layer is not perfect (some delaminations or voids can be present, which can overlap the bonding area etc.), and so significant alteration of the Re(Z) can occur, as it can be seen experimentally and in FEM computations.

4. CONCLUSIONS

The article presents a self-contained study about E/M impedance method for SHM thin circular plates. Comparisons between the analytical method, the finite element method, and experiments were performed, with fabricated structural arc-shape defects. Changes in the E/M impedance spectrum due to presence of a

crack were investigated. It is certified that the E/M impedance method presents the following advantages: small size of the permanently attached or embedded piezoelectric sensors, ultrasonic frequency range application, and ability to be used for on-line and in service SHM.

ACKNOWLEDGEMENTS

The authors gratefully acknowledge the financial support of the National Authority for Scientific Research−ANCS, UEFISCSU, through STAR research project code ID 188/2012.

REFERENCES

1. GIURGIUTIU, V., *Structural Health Monitoring with Piezoelectric Wafer Active Sensors*, Elsevier Academic Press, 2008.
2. ZAGRAI, A., GIURGIUTIU, V., *Electro-mechanical impedance method for crack detection in thin plates,* Journal of Intelligent Material Systems and Structures, **12**, *10*, pp. 709–718, 2001.
3. URSU, I., TECUCEANU, G., TOADER, A., BERAR, V., *Simultaneous active vibration control and health monitoring of structures. Experimental results*, INCAS Bulletin, **2**, *2*, 114–127, 2010.
4. URSU, I., GIURGIUTIU, V., TOADER, A., *Towards spacecraft applications of structural health monitoring*, INCAS Bulletin, **4**, *4*, pp. 111–124, 2012.
5. LEISSA, A., *Vibration of Plates*, NASA SP-160, US Gov't Printing Office, 1969.
6. POISSON, S.-D., *Memoires de l'Academie royale des Sciences de l'Institut de France*, Tome VIII, 1829.
7. ABRAMOWITZ, M., STEGUN, I., *Handbook of Mathematical Functions with Formulas, Graphs, and Mathematical Tables*, Dover Publications, Inc., 1964.
8. ITAO, K., CRANDALL, S. H., *Natural modes and natural frequencies of uniform, circular free-edge plates,* J. Appl. Mech., **46**, 448–453, 1979.
9. KREYSZIG, E., *Advanced Engineering Mathematics*, Wiley, NY, 1968.
10. BICKFORD, W. B., *Advanced Mechanics of Materials*, Addison Wesley Longman, Inc., 1998.
11. *** *Standard on Piezoelectricity,* IEEE std 176-1987; doi: 10.1109/IEEESTD.1988.79638.

Received Decenber 3, 2013

THE PUBLISHING HOUSE
OF THE ROMANIAN ACADEMY

PROCEEDINGS OF THE ROMANIAN ACADEMY, Series A,
Volume 15, Number 3/2014, pp. 283–291

ANALYTICAL-NUMERICAL COUPLING ANALYSIS OF SUBMARINE PIPELINE IN J-LAY PROBLEM

Zheng LIANG [1], Fei WANG [1], Xiong DENG [2]

[1] Southwest Petroleum University, School of Mechatronic Engineering, Chengdu, 610500, RP China
[2] Southwest Petroleum University, School of Petroleum and Natural Gas Engineering, Chengdu, 610500, RP China
E-mail: hanshuichun1@126.com

The article present an analytical-numerical coupling model to deal with the submarine pipeline during its installation in deep water using J-lay method. The pipeline is divided into two segments in this paper: the touchdown segment and the suspended segment. An analytical method was used to analyse the touchdown segment considering the elastic deformation of the seabed as Pasternak foundation and a numerical method for the suspended segment which allows the influence of ocean current to be considered using the method of weighted residuals after the deformation differential equation was proposed to analyse the behaviour of the whole pipeline during its installation. The variation tendency of the longitudinal stress, the hoop stress and the shearing stress of the pipeline as well as the influence of different launching angles and tension forces to them are analysed in this paper which could give good suggestions to the submarine pipeline designers or the pipeline installation managers.

Key words: analytical-numerical coupling analysis, submarine pipeline, *J*-lay installation, touchdown segment, suspended segment, launching angle, tension force.

1. INTRODUCTION

Submarine pipelines, the most efficient cost-effective means of large scale transportation for oil and nature gas form producers to end-users in deep-water by far, have caught much attention in recent decades, with on-gong development of offshore oil and gas exploitation. The offshore industry has been called to improve the laying of submarine pipelines technology for the reason that most pipelines may encounter the highest stresses during the installation process [1, 2] to deal with environmental hazards, typical of such hostile ocean environment in deep-water. Compared with the conventional pipeline installation method such as the S-lay method and the Reel-lay method, the J-lay method, whose name comes after the shape of the pipeline during the laying and consists in lowering the pipe almost vertically into the water by an inclined ramp has been widely accepted as the most suitable and favourable installation method in deep-water because of its most important characteristics [3].

To predict the J-lay process mechanical features, e.g., top angle and tension, pipe bending tension stiffness, ocean currents, soil stiffness and slope, boundary layer phenomena, former researchers have pioneered work through both analytical and numerical methods. Plunkett [4] adopted the singular perturbation method to derive asymptomatic expansion to deal with the behaviour of stiffened catenary, considering the boundary layers. Dixon and Rutledge [5] used the perturbation method to analyze the J-lay method. Some researchers [6, 7] have developed the analytical method in the following years and it proves effective and simple except for the disadvantage that it is not able to consider the effect of ocean currents and pipe embedment. Lenci and Callegari [8] raised some analytical models with linearly elastic seabed to reveal the theoretical basis of the J-lay problem, but the created models are not able to consider the ocean currents effects. Some available numerical tools take the influence of ocean current and seabed embedment into account [9, 10]. Of the numerical tools, mechanical features should be assumed before calculation which makes them inconvenient to use and the commercial numerical tools are often uneconomical. Li [3] created a simple numerical model neglecting the high-order terms of the suspended portion of the laying pipe to analyse the J-lay problem and the model can take into account the influence of ocean currents and pipe

embedment. Though years of research on mathematic model of the laying process of submarine pipelines, most researchers regard it as elastic large deflection beam model, considering the non-linearity elasticity large deformation of the pipeline during its installation.

The aim of this paper is to investigate an analytical-numerical coupling method taking the influence of large deformation of the suspended portion of pipeline during J-lay deployment into consideration for the analysis of the mechanical behaviour of the submarine pipeline. The pipeline, in the analytical-numerical coupling model presented in this paper, is divided into two segments: the suspended segment of the pipeline and the touchdown segment of the pipeline. Indeed, one of the main achievements of this paper is proposing an analytical-numerical coupling model taking the influence of currents into consideration using the large deflection theory when analysing the suspended portion of the pipeline and taking into account the pipe embedment during its installation using J-lay method.

2. GOVERNING EQUATIONS

As shown in Fig.1, the submarine pipeline which is to be installed in deep-water, considering its different internal stresses during its installation using J-lay method, is divided into two segments: one segment of the submarine pipeline is the touchdown segment laid on seabed form left boundary point (P_1) where balance the soil frictional force and axial force of the pipeline to touchdown point (TDP) and the other segment of the submarine pipeline is the suspended segment that suspended in the water from touchdown point (TDP) to the lift-off point (P_2) of the laying vessel. In this article, one global coordinate system (x, y) is used with its origin at (0, 0) of touchdown point (TDP). An analytical model to analyse the touchdown segment and a numerical model to analyse the suspended segment are proposed in this chapter.

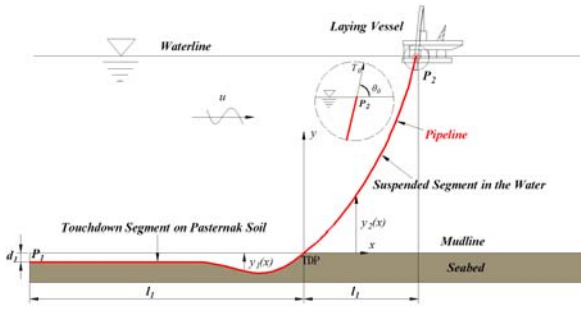

Fig. 1 – Scheme of the model.

2.1. Touchdown segment

The embedment of the touchdown segment of pipeline into the seabed during installation resulting from special soil surrounding environment on the seabed introduce stresses and strains which have significant influence on the success of pipe laying. The influence of current on the touchdown segment could be ignored in this model for the ocean current velocity is small.

Analysing the mechanical model of the touchdown segment of the pipeline shown as in Fig. 2a and considering the application force of a differential touchdown pipe segment of stretched length dx shown as in Fig. 2b, the equilibrium equations for the touchdown segment of the pipe can be derived:

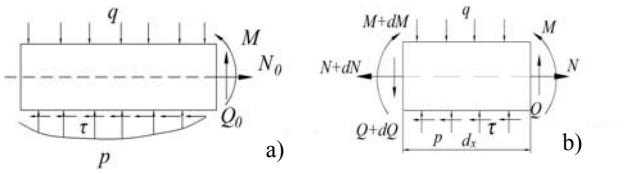

Fig. 2 – a) Fore sketch of the touchdown segment; b) fore sketch of a differential touchdown segment.

$$\begin{cases} \sum X = \mathrm{d}N - \tau \mathrm{d}x = 0 \\ \sum Y = \mathrm{d}Q + (w - p)\,\mathrm{d}x = 0 \\ \sum M = \mathrm{d}M - N\mathrm{d}y - Q\mathrm{d}x = 0, \end{cases} \tag{1}$$

where: N is the axial force and Q is the shearing force of the pipeline, w is the submerged weight of the touchdown pipe per length, p is the soil resistance to a touchdown pipe of a unit length, τ is the soil frictional force to the pipe per length, X, Y and M are the touchdown segment pipe's vertical force, horizontal force and bending moment, respectively.

Considering the seabed is not rigid in this model but behaves like a Pasternak foundation, and the bending moment of the touchdown segment could be obtained by the small deflection theory. Then the governing equation of the touchdown segment of pipeline can be obtained as:

$$EIy_1^{(4)}(x) - (N_0 + G_p D)y_1''(x) + \tau y_1' + kDy_1(x) - w = 0 \quad (x \le 0), \tag{2}$$

where dN is the differential axial force on the touchdown point, and it can be obtained as $N_0=\tau l_1$, here l_1 is the length left boundary point (P_1) to touchdown point (TDP), k is the seabed stiffness, D is the outer diameter of the pipeline, EI is the bending stiffness of the pipeline, G_P is the shear modulus of seabed and it can be obtained as $G_P= 0.5E_s/(1+\upsilon_s)$, where E_s and υ_s are the Young's modulus and Poisson ratio of the seabed.

The general solution of the governing equation can be obtained by

$$y_1(x) = e^{\alpha_1}\left[C_1\cos(\beta_1 x) + C_2\cos(\beta_1 x)\right] + e^{\alpha_2}\left[C_3\cos(\beta_2 x) + C_4\cos(\beta_2 x)\right] - \frac{w}{kD} \quad (x \le 0), \tag{3}$$

where C_1, C_2, C_3, C_4 are unknown coefficients and α_1, α_2, β_1 and β_2 are constant parameters calculated by EI, N_0, E_s, υ_s, τ and k. Then the shearing force of the pipeline can be obtained as $Q(x) =–EIy'''_1(x)$.

Considering the inclination slop, bending moment and shear force at left boundary point, and assuming the embedment depth of the touchdown segment at left boundary point is d_1, we face a system of 4 boundary equations with 4 unknown coefficients (C_1, C_2, C_3, C_4): $y_1(–l_1) = –d_1$; $y'_1(–l_1) = 0$; $y''_1(–l_1) = 0$; $y'''_1(–l_1) = 0$.

Then, the longitudinal stress σ_x, the hoop stress σ_y and the shearing stress τ_{xy} of the touchdown segment of the pipe can be obtained as: $\sigma_x = (N_0–\tau x)/\delta + EIy''_1(x)/W$; $\sigma_y = 0.5\gamma_w hD/\delta$; $\tau_{xy} = 2\,EIy'''_1(x)/B$, where B is the cross section area of the pipe, W is the bending modulus of the pipe, γ_w is specific weight of ocean water, h is the depth of ocean, δ is the thickness of the pipeline.

2.2. Suspended segment

Considering the equilibrium of the vertical force V, horizontal force H and the bending moment M of a differential suspended pipe segment of stretched length d_s subjected to gravity, external hydrodynamic loading and internal structural response loading, shown as in Fig. 3. The influence of the ocean current to the suspended segment of the submarine pipeline is considered in this model during its installation.

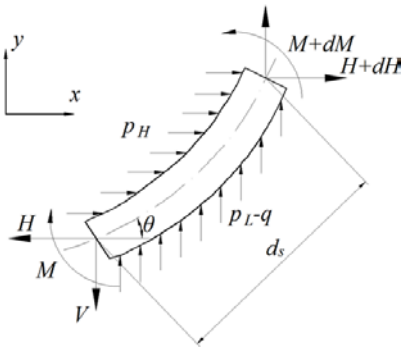

Fig. 3 – Fore sketch of a differential suspended segment.

The equilibrium equations for the suspended pipe segment are set up as:

$$\begin{cases} \mathrm{d}H + p_H \sin\theta \mathrm{d}s = 0 \\ \mathrm{d}V + (p_V - w)\cos\theta \mathrm{d}s = 0 \\ \mathrm{d}M - H\sin\theta \mathrm{d}s + V\cos\theta \mathrm{d}s = 0, \end{cases} \tag{4}$$

where: θ is the inclination slop of the submarine pipeline, d_s is the length of a differential suspended segment, w is the submerged weight of the suspended pipe per length, p_H is the horizontal force obtained as $p_H = 0.5\rho_w C_D D u|u|$, and p_V is the vertical force obtained as $p_V = 0.5\rho_w C_L D u^2$ acted on the suspended pipe by the ocean current, here ρ_w is the density of ocean water, u is the current velocity, C_D and C_L are the drag coefficient and lift coefficient of the pipeline, respectively [11].

The geometric relationship shown as below can be obtained as $\cos\theta \mathrm{d}s = \mathrm{d}x$, $\sin\theta \mathrm{d}s = \mathrm{d}y_2$, $\mathrm{d}x/\mathrm{d}s = \mathrm{d}x/((\mathrm{d}x)^2+(\mathrm{d}y_2)^2)^{-0.5} = 1/(1+(\mathrm{d}y_2/\mathrm{d}x)^2)^{-0.5}$, and the bending moment of the suspended pipeline can be obtained by multiplying the bending stiffness EI and the curvature as $M = EI\mathrm{d}\theta/\mathrm{d}s$. Assuming the length of horizontal suspended segment of the pipeline was l_2, we obtain:

$$\frac{\mathrm{d}M}{\mathrm{d}x}=EI\frac{\mathrm{d}^2\theta}{\mathrm{d}s\cdot\mathrm{d}x}=EI\left(\frac{y_2'''(x)}{1+\left(y_2'(x)\right)^2}-\frac{y_2''(x)}{1+\left(y_2'(x)\right)^2}\cdot\frac{y_2'(x)\cdot y_2''(x)}{1+\left(y_2'(x)\right)^2}\right)\quad(0\le x\le l_2). \tag{5}$$

The governing equation of the pipeline suspended in water could be obtained by means of the Eq. (4), and Eq. (5):

$$EI\left[y_2'''(x)+y_2''(x)\cdot\left(y_2'(x)\right)^2-\left(y_2''(x)\right)^2\cdot y_2'(x)\right]+\left(V-Hy_2'(x)\right)\left[1+\left(y_2'(x)\right)^2\right]^2=0\ \ (0\le x\le l_2), \tag{6}$$

where $H=N_0-\int_0^{y_2}p_H\mathrm{d}y_2$, $V=Q_0-\int_0^{x}\left(p_L-w\right)\mathrm{d}x$. The suspended segment's governing equation belongs to the nonlinear higher-order differential equation and the accurate analytical solution could not be obtained. Here we assume $x = 0.5l_2 + 0.5l_2t$ ($-1 \le t \le 1$), then the governing equation of the pipeline suspended in water could be expressed as follows:

$$EI\left[\frac{8\mathrm{d}^3y_2}{l_2^3\mathrm{d}t^3}+\frac{8\mathrm{d}^3y_2}{l_2^3\mathrm{d}t^3}\cdot\left(\frac{2\mathrm{d}y_2}{l_2\mathrm{d}t}\right)^2-\frac{2\mathrm{d}y_2}{l_2\mathrm{d}t}\left(\frac{4\mathrm{d}^2y_2}{l_2^2\mathrm{d}t^2}\right)^2\right]+\left(V-\frac{2H\mathrm{d}y_2}{l_2\mathrm{d}t}\right)\left[1+\left(\frac{2\mathrm{d}y_2}{l_2\mathrm{d}t}\right)^2\right]^2=0\quad(-1\le t\le 1). \tag{7}$$

The approximate solution of Eq. (7) could be found by using the method of weighted residuals (henceforth abbreviated as MWR) and a trial function is taken in the form using Chebyshev polynomial:

$$y=0.5C_5+C_6t+C_7\left(2t^2-1\right)+C_7\left(4t^3-3t\right)+C_9\left(8t^4-8t^2+1\right)+C_{10}\left(15t^5-20t^3+5t\right)\ (-1\le t\le 1), \tag{8}$$

where C_5, C_6, C_7, C_8, C_9 and C_{10} are parameters to be determined in the solution. Substituting Eq. (8) into Eq. (7), we can obtain the residuals within the field as $R_1=\sum_{i=0}^{20}K_it^i\quad(-1\le t\le 1)$, where K_i is a parameter calculated by C_5, C_6, C_7, C_8, C_9 and C_{10}. The weighting functions can be chosen in many ways and each choice corresponds to a different criterion of the MWR [12]. The weighting functions in this article can be obtained using the subdomain method so that $\int_{-1}^{1}R_I\mathrm{d}t=0$. There are six unknown parameters (C_5, C_6, C_7, C_8, C_9 and C_{10}) in the equation, and we could get boundary conditions respectively at lift-off point (P_2) and touchdown point (TDP) considering the displacement and slope angle at P_2 and the continuity of displacement, bending moment and shear force at TDP:

P_2:
$$\begin{cases}y_2(x)|_{x=l_2}=y_2(t)|_{t=1}=0.5C_5+C_6+C_7+C_8+C_9+C_{10}=h\\ y_2'(x)|_{x=l_2}=y_2'(t)|_{t=1}=2l_2^{-1}\left(C_6+4C_7+8C_8+16C_9+25C_{10}\right)=\tan\theta\end{cases} \tag{9}$$

TDP:
$$\begin{cases}y_1(x)|_{x=0}=y_2(x)|_{x=0}=y_2(t)|_{t=-1}\\ y_1'(x)|_{x=0}=y_2'(x)|_{x=0}=y_2'(t)|_{t=-1}\\ y_1''(x)|_{x=0}=y_2''(x)|_{x=0}=y_2''(t)|_{t=-1}\\ y_1'''(x)|_{x=0}=y_2'''(x)|_{x=0}=y_2'''(t)|_{t=-1}\end{cases} \tag{10}$$

where h is the depth of the ocean where vessel located, θ is the slope angle at P_1. Then the tension force that the pipeline need at lift-off point (P_2) can be calculated as $T_2 = B\ (N_2^2 + Q_2^2)^{0.5}$, where N_2, Q_2 are the axial stress and the shear stress of the pipeline at lift-off point (P_2), B is the cross-sectional area of the pipeline.

The longitudinal stress σ_x, the hoop stress σ_y and the shearing stress τ_{xy} of the suspended segment of the pipe can be obtained as: $\sigma_x = (H\cos\theta + V\sin\theta)/B + EIy''_2(x)/W$; $\sigma_y = 0.5\gamma_w\ (h-y_2)\ D/\delta$; $\tau_{xy} = 2\ EIy'''_2(x)/B$.

3. SOLUTIONS

The proposed mathematical model to analyse the submarine pipeline's behaviour during its installation using J-lay method is so complicated that no explicit solution of the model can be found. In this article, a numerical method is used. At the beginning of the solutions, basic parameters such as parameters of pipeline, depth of ocean, ocean currents, and parameters of soil are input for both touchdown segment of pipeline laid on the seabed and pipeline suspended in the water. To start the calculation of the touchdown segment and suspended segment of pipeline, it is necessary to assume an initial d_1 and an initial l_1. And then, the two initial parameters can be input into the 4 boundary equations of touchdown segment to determine the four unknown parameters C_1, C_2, C_3 and C_4. Eventually, the axial force, the displacement, the first-order derivative, the second derivative, the third derivative and the shear force on the touchdown point can be obtained.

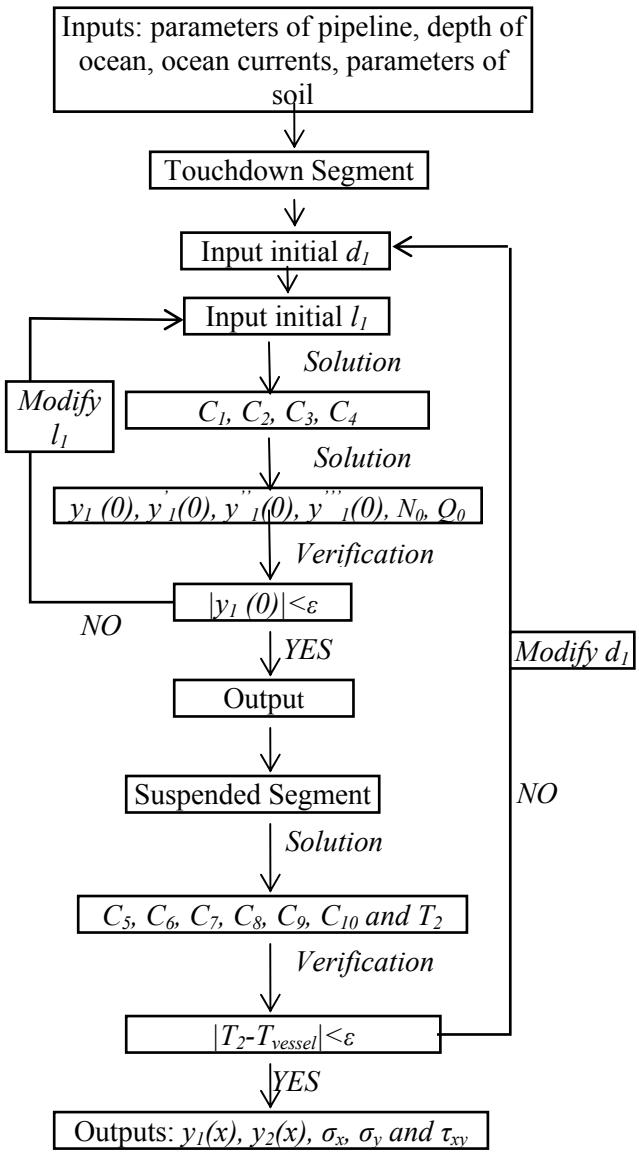

Fig. 4 – Flow scheme for J-lay method calculation.

To guarantee the continuity of displacement at the touchdown point, verification is needed to see if $|y_1(0)| < \varepsilon$ is satisfied, where $y_1(0)$ is the displacement of the pipeline on the touchdown point, and ε is a small specified quantity. If $y_1(0) > \varepsilon$ appears, l_1 must be too large and should be decreased. If $y_1(0) < -\varepsilon$ appears, l_1 must be too small and should be increased. After $|y_1(0)| < \varepsilon$ is satisfied, the solution of the touchdown segment of pipeline is done. The output of the displacement, the first-order derivative, the second derivative and the third derivative on the touchdown point calculated in the touchdown segment can then input into Eq. (9) and Eq. (10) to determine the six unknown parameters C_5, C_6, C_7, C_8, C_9, C_{10} and the parameter of T_2 can be obtained too. Considering the accuracy of the calculation, $|T_2 - T_{vessel}| < \varepsilon$ must be satisfied when the calculation of the suspended segment of pipeline is completed, where T_{vessel} is the total real tension at lift-off point (P_2) during the installation of pipeline. If $|T_2 - Tvessel| > \varepsilon$ appears, d_1 must be modified. After $|T_2 - T_{vessel}| < \varepsilon$ is satisfied, the analysis of the behaviour of the touchdown segment and suspended segment of the submarine pipeline during its installation using J-lay method are done and the detailed process is shown in Fig. 4.

4. EXAMPLES

To illustrate the previous model with some examples, a typical pipeline is selected with its basic parameters including the outer diameter $D = 0.60$m, thickness $\delta = 0.025$m, bending stiffness $EI = 3.92\times10^8$Nm^2,

bending modulus $W = 4.869\times10^{-3}\text{m}^3$, submerged weight of the touchdown pipe per length $w = 632.5\text{N/m}$, lift coefficient $C_L = 1.3$ and drag coefficient $C_D = 1.5$. An ultra-deep water ocean is selected in this section with its depth $h = 2\,000\text{m}$, density of ocean water $\rho_w = 1\,030\text{kg/m}^3$ and current velocity $u = 0.93\text{m/s}$. We assumed the touchdown segment of the pipeline is supposed to be rest on a Pasternak deformable seabed with its soil frictional force to the pipe per length $\tau = 24\,500\text{N/m}$, seabed stiffness $k = 78.6\text{kN/m}^2$, young's modulus $E_s = 80\text{MN/m}^2$ and Poisson ratio $\upsilon_s = 0.2$.

The parameters of launching angle at lift-off point which adjusted by hinged ramp and tensioner of the laying vessel and tension force which adjusted by tensioner of the laying vessel, could controlled by pipe installation managers. Once the ocean environment and seabed condition and the pipeline which to be installed are confirmed, managers could choose suitable launching angle and tension force to ensure the stress of the pipeline is less than the allowable stress of the pipeline. It's important to choose suitable launching angle and tension force to installation managers under the consideration of different sea state, pipeline parameters, ocean depth and soil parameters during the J-lay deployment. The launching angle and tension force are investigated in detail in this article to predict their influence on the pipe configuration, longitudinal stress, hoop stress and shearing stress of the pipeline.

4.1. Influence of launching angle

The influence of different launching angles to configuration and stresses of pipeline predicted by the previous model derived in this article with the tension force $T_{vessel} = 3\text{MN}$ adjusted by the tensioner of the laying vessel at lift-off point are depicted in Fig. 5. Three different launching angles are chosen for the analysis: 85°, 75° and 65°.

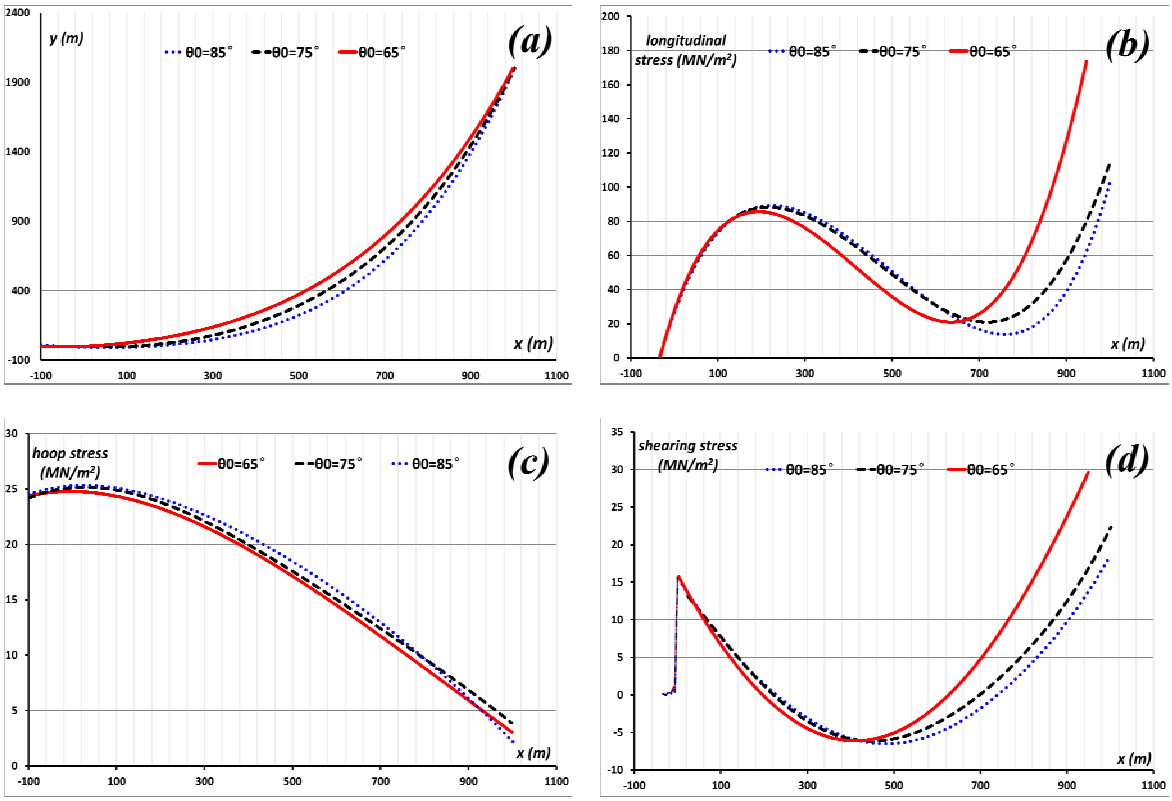

Fig. 5 – a) Configuration of pipeline for different launching angles; b) the longitudinal stresses for different launching angles; c) the hoop stresses for different launching angles; d) the shearing stresses for different launching angles.

Shown as in Fig. 5, the stresses of the pipeline have different variation tendency. The minimum longitudinal stress appears at the touchdown segment of the pipeline and the value of the longitudinal stress has decrease after a short increase to the right of the touchdown point, and then the value of the longitudinal stress increases to the maximum at the lift-off point (Fig. 5b). The maximum hoop stress appears at the touchdown segment of the pipeline and then the value of hoop stress decline to the minimum at lift-of point

of the laying vessel (Fig. 5c). The variation curve of the shearing stress, shown as in Fig. 5d, present a *u* shaped trend: the shearing stress values of the pipeline at touchdown point and lift-off point are much bigger than the shearing stress values of other part of the pipe and the suspended segment even have negative shearing stress values. The maximum shearing stress appears at the lift-off point of the laying vessel.

The configuration and stresses of pipeline vary with the launching angles. Minor differences appear that the radius of curvature of the pipeline becomes smaller when choosing a larger launching angle at lift-off point, although the configurations of pipeline for different launching angles are almost coincide (Fig. 5a).The stresses including the longitudinal stress, the hoop stress and the shearing stress of the pipeline for different launching angles near the touchdown point are almost the same when the launching angles changing. On the other hand, the stresses near the lift-off point vary with the launching angles change: the value of the stresses decrease when choosing a bigger launching angle while installation of the pipeline. The reason for the change is that: the height of the lift-off point will gets lower as the launching angle at the lift-off point increase, causing the support force applied to the pipeline by the tensioner of the laying vessel increase. Then, the stresses of the pipeline will be much smaller. Therefore, the installation manager should choose a larger launching angle of the pipeline if conditions are satisfied.

4.2. Influence of tension force

Same as the launching angle of the pipeline at the lift-off point, the parameter of tension force at the lift-off point which could adjusted by managers is also important. Fig. 6 shows the configuration and stresses of pipeline for different tension force predicted by the previous model derived in this article with the launching angle $\theta_0 = 75°$. Three different tension forces are chosen for the analysis: 4MN, 3MN and 2MN.

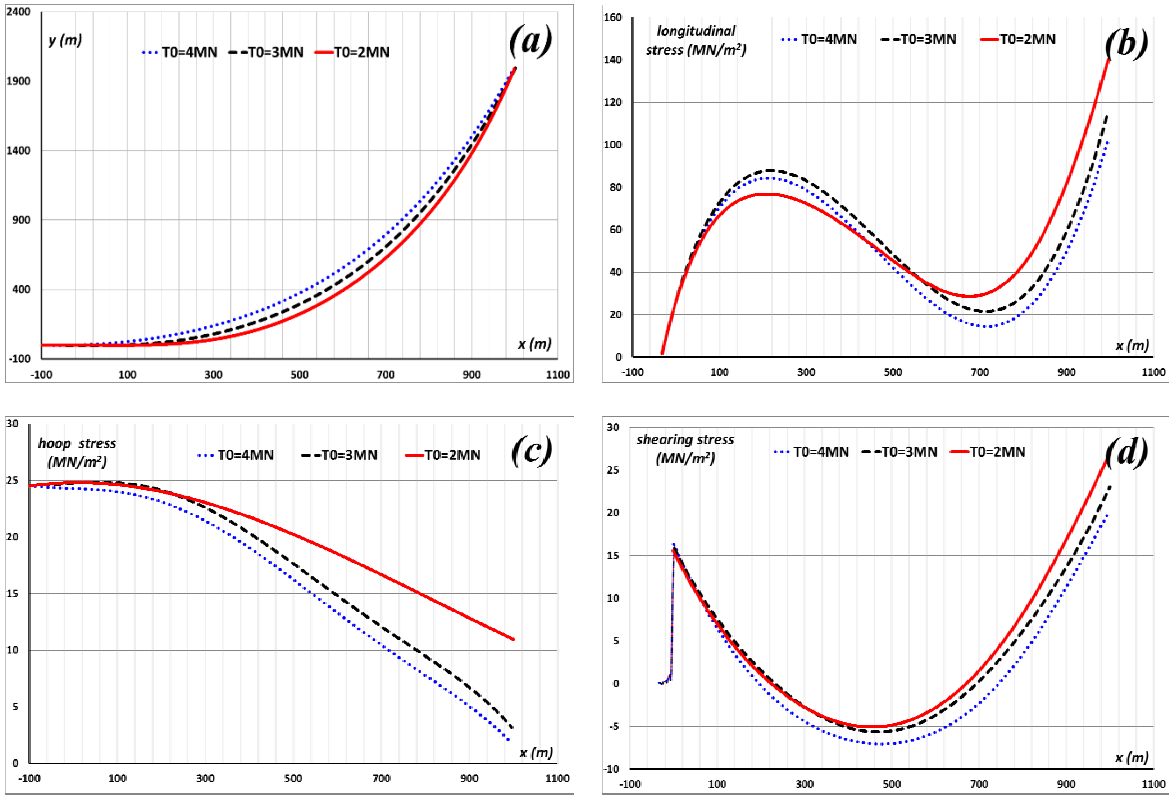

Fig. 6 – a) Configuration of pipeline for different tension force; b) the longitudinal stresses for different tension force; c) the hoop stresses for different tension force; d) the shearing stresses for different tension force

Same as the influence of launching angles, the radius of curvature of the pipeline becomes larger when choosing a larger tension force at lift-off point, although the configurations of pipeline for different tension forces are almost coincide (Fig. 6a).The stresses including the longitudinal stress (Fig. 6b), the hoop stress (Fig. 6c) and the shearing stress (Fig. 6d) of the pipeline for different tension forces near the touchdown

point are almost the same when the tension force changing. On the other hand, the value of the stresses decrease when choosing a bigger tension force while installation of the pipeline. The reason for the change is that: the effect of gravity to the pipeline will be reduced and the height of the lift-off point will gets lower as the tension force at the lift-off point increase, causing the support force applied to the pipeline by the tensioner of the laying vessel increase. Then, the stresses of the pipeline will be much smaller. Therefore, the installation manager should choose a larger launching angle of the pipeline if conditions are satisfied.

5. CONCLUSIONS

A simple analytical model for predicting the submarine pipeline's touchdown segment and a numerical model for the submarine pipeline's suspended segment which allows the influence of ocean current to be considered are proposed to analyse the behaviour of the pipeline during its installation. The general solution for the touchdown segment of the pipeline is obtained considering the elastic deformation of the seabed using Pasternak foundation in the analytical model and the numerical solution for the suspended segment of the pipeline is obtained using the method of weighted residuals after the deformation differential equation of the suspended segment was proposed.

The presented model is applied to analyse the variation tendency of the longitudinal stress, the hoop stress and the shearing stress of the pipeline as well as the influence of different launching angles and tension forces to them:

1. The minimum longitudinal stress appears at the touchdown segment of the pipeline and the value of the longitudinal stress has a decrease after a short increase to the right of the touchdown point, and then the value of the longitudinal stress increases to the maximum at the lift-off point. The maximum hoop stress appears at the touchdown segment of the pipeline and the value of hoop stress decline to the minimum at lift-of point of the laying vessel. The variation curve of the shearing stress presents a "u" shaped trend: the shearing stress values of the pipeline at touchdown point and lift-off point are much bigger than the shearing stress values of other part of the pipe and the suspended segment even have negative shearing stress values. The maximum shearing stress appears at the lift-off point of the laying vessel.

2. The radius curvature of the pipeline becomes smaller when choosing a larger launching angle or a smaller tension force at lift-off point of laying vessel. The stresses of the pipeline near the touchdown point are almost the same when the launching angles or tension force are changing while the stresses near the lift-off point vary much: the value of the stresses decrease when choosing a bigger launching angle or tension force while installation of the pipeline. The reason for the change is that: the height of the lift-off point will gets lower as the launching angle or tension force at the lift-off point increase, causing the support force applied to the pipeline by the tensioner of the laying vessel increase. Then, the stresses of the pipeline will be much smaller. Therefore, the installation manager should choose a larger launching angle or tension force at the lift-off point of the laying vessel if conditions are satisfied.

ACKNOWLEDGMENTS

The authors would like to acknowledge the support of Grant No. 2012AA09A203 from the National High Technology Research and Development Program of China (863 Program) and Grant No. 2011STS04 from the Key Laboratory of Oil and Gas Equipment from Ministry of Education, China.

REFERENCES

1. Brando P., Sebastiani G., *Determination of sea lines elastic curves and stresses to be expected during laying operation*, Offshore Technology Conference, Houston, USA, 1971.
2. Powers J. T., Finn L. D., *Stress analysis of offshore pipelines during installation*, Offshore Technology Conference, Houston, USA, 1969.
3. Li Z. W., Feng Y., Zhen G., Ling L. L., *Numerical analysis of pipeline in J-lay problem*, J Zhejiang Univ-SciA, **11**, *11*, pp. 908–919, 2010.
4. Plunkett R., *Static bending stresses in catenaries and drill strings*, J. Eng. Ind., **89**, *1*, pp. 31–36, 1967.

5. Dixon D. A., Rultledge D. R., *Stiffened catenary calculation in pipeline laying problem*, J. Eng. Ind., **90B**, *1*, pp. 153–160, 1968.
6. Palmer A. C., Hutchinson G., Ells W. J., *Configuration of submarine pipelines during laying operations*, J. Eng. Ind., **96**, pp. 1112–1118, 1974.
7. Guarracino F., Mallardo V., *A refined analytical analysis of submerged pipelines in seabed laying*, Appl. Ocean Res., **21**, *6*, pp. 281–293, 1999.
8. Lenci S., Calegari M., *Simple analytical models for the J-lay problem*, Acta Mechanica, **178**, pp. 23–39, 2005.
9. Savik S., Giertsen F., Bertsen V., *Advances in design and installation analysis of pipelines in congested areas with rough seabed topography*, Proc., 23rd Int. Conf. on offshore Mechanics and Arctic Engineering, Vancouver, Canada, 2004.
10. Callegari M., Carini C. B., Lenci S., Torselletti E., Vitali L., *Dynamic models of marine pipelines for installation in deep and ultra-deep waters: Analytical and numerical approaches*, Proc., 16th AIMETA Congress of Theoretical and Applied Mechanics, Milano, Italy, 2003.
11. Subrata K. C., *Handbook of offshore Engineering*, Elsevier Press, Elsevier Science Publishers, 2005.
12. Finlayson B. A., Scriven L. E., *The method of weighted residuals-a review*, Applied Mechanics Reviews, **19**, *9*, pp. 735–748, 1966.

Received December 23. 2013

THE PUBLISHING HOUSE
OF THE ROMANIAN ACADEMY

PROCEEDINGS OF THE ROMANIAN ACADEMY, Series A,
Volume 15, Number 3/2014, pp. 292–299

GENERATION OF STATIONARY GAUSSIAN TIME SERIES COMPATIBLE WITH GIVEN POWER SPECTRAL DENSITY

Marius GIUCLEA [1,2], Ana-Maria MITU [1], Ovidiu SOLOMON [2]

[1] Institute of Solid Mechanics of the Romanian Academy, 15 Constantin Mile St., 70701, Bucharest, Romania
[2] Bucharest University of Economic Studies, Department of Mathematics, 6 Romana Square, Bucharest, RO-010374, Romania
Ana-Maria Mitu, mitu@imsar.bu.edu.ro

In this paper, an improved method for simulation wide-sense stationary random time-series, derived from either analytical or experimental descriptions of its power spectral density (PSD), is presented. In the proposed approach, the sample functions of the target random process are represented by a superposition of statistically independent sine random signals with uniformly distributed phase angles and random envelopes following Rayleigh distributions. The simulated random processes are asymptotically Gaussian processes as the number of terms approaches infinity. This property is not generally true when the standard representation through a series of random harmonic waves with uniformly distributed phases is employed, as is the case of random signals with PSD displaying sharp peaks. The proposed method is illustrated for analytical forms of road input spectral densities that can or cannot be generated by linear shape filters such as are rational functions or split power approximations, respectively. The method is validated by comparison of spectral response of a quarter car model, obtained by numerical simulation for a generated road profile input with that obtained analytically by using input-output relationships for linear oscillating systems.

Key words: power spectral density, random time series simulation, Rayleigh distribution, road input, quarter car model.

1. INTRODUCTION

In many practical applications, it is necessary to simulate samples of stationary Gaussian stochastic process compatible with given power spectral density, which has specific analytical form or is obtained by fitting experimental data. There are cases in which the sample functions can be generated with satisfactory approximation as the output of linear shape filters to band-limited white noise input. For instance, sample functions of a stationary random process with PSD expressed by polynomial ratio (depending on ω^2), can be obtained as the output of linear shape filters to white noise input [1, 2, 3, 4, 5]. On the other hand, in many cases of practical interest, as is the case of split power law proposed in ISO 8608 [6] for road roughness classification, the problem is that road inputs cannot be simulated by this method [5]. Another approach for generating time series which are required to satisfy a given PSD function, consists in their representation as finite series of harmonic frequency components with amplitudes derived from the target spectral density values, having uniformly distributed random phases [4, 7, 8, 9]. The main drawback of this approach is that the sample distribution function of the simulated random processes is not generally Gaussian even for large values of N. For example, this shortcoming can occur when the target PSD displays sharp peaks.

In this paper, a new approach to the simulation of wide-sense stationary random time series, defined by its PSD, is presented. The proposed method is based on the fact that the Rayleigh distribution is the limiting distribution function of peak values for a narrow–band Gaussian random signal as the bandwidth approaches zero [10, 11]. Accordingly, the sample functions of the target random process are represented by a superposition of N weighted statistically independent harmonic random signals with uniformly distributed phase angles and random envelopes following Rayleigh distributions. The parameters of these distributions are determined from the given PSD in a similar way as the amplitudes of the harmonic components are estimated in the framework of standard method. The weighting coefficients are used to compensate the band-

pass filtering effects on Rayleigh distribution parameters. As the simulated sine waves components can be considered with good accuracy as statistically independent random processes following Gaussian distributions [12], the sample distribution function of the simulated processes is practically Gaussian even for relatively small values of N. The proposed method can be applied for any analytical or experimental description of the given spectral density. In this paper the method is applied to generate sample functions of random inputs induced by road irregularities with PSD specified by a rational expression of ω^2. In the considered application, the spectral densities of numerically generated random time series are estimated by using third-octave band-pass filters. The method is validated by comparing the spectral response of a quarter car model, obtained by numerical simulation for a generated road profile input with that obtained analytically by using input-output relations for linear oscillating systems.

2. ANALYTICAL DESCRIPTION OF SIMULATION METHOD

Consider a Gaussian stationary stochastic process $y(t)$ and $G(\omega)$ its one sided power spectral density. Supposing that the $G(\omega)$ is known, in order to generate stationary Gaussian time series compatible with the given PSD, the following discrete mean square approximation for the sample functions of random process $y(t)$ is considered

$$y(t_i) \cong \tilde{y}(t_i) = \sum_{k=1}^{N} \rho_k x_k(t_i), \quad t_i = i\Delta t, \quad i = 1, 2, ..., M, \quad M\Delta t = T, \tag{1}$$

where

$$x_k(t_i) = A_k(t_i)\cos(\omega_k t_i + \theta_k), \; k = 1, ..., N \tag{2}$$

are discrete narrow-band stationary random signals with bandwidth centre frequencies ω_k. The time moments at which the positive peak values of $\cos(\omega_k t_i + \theta_k)$ occur, are given by

$$t_{kl} = \frac{2\pi l - \theta_k}{\omega_k}, \; k = 1, ..., N, \; l = 0, 1, 2, ..., l(k). \tag{3}$$

The random time series $A_k(t_i)$ are obtained by interpolation of positive peak values $A_k(t_{kl})$ of the components (2).

The random series $A_k(t_{kl})$ are generated as deviates of Rayleigh distributions with parameters λ_k. The phase angles θ_k are treated as random variables uniformly distributed on the interval $[0, 2\pi)$. Therefore, the distributions of discrete random signals (2) are Gaussian with zero mean values and variances λ_k. In order to generate the amplitude modulated random signals (2) within the same time interval $[t_0, T + t_0]$, it is sufficient to set the values of t_0 and $l(k)$ as the integer parts of $(2\pi/\omega_1 + 1)$ and $(T\omega_k/2\pi)$, respectively. Assuming that $x_k(t), k = 1, 2, 3, ..N$, approximate the random processes obtained by filtering $\tilde{y}(t)$ with band-pass filters having sharp cut-off characteristics in the frequency range $[\omega_k - \Delta\omega_k/2, \omega_k - \Delta\omega_k/2]$, the values of its power spectral density $\tilde{G}(\omega)$ at centre frequencies ω_k can be estimated by [10]:

$$\tilde{G}(\omega_k) = \frac{\tilde{\sigma}^2(\omega_k, \Delta\omega_k)}{\Delta\omega_k} = \frac{\lambda_k^2}{\Delta\omega_k}, \tag{4}$$

where $\tilde{\sigma}^2(\omega_k, \Delta\omega_k)$ is the mean square value of the k^{th} filter output.

Hence, by imposing $\tilde{G}(\omega_k) = G(\omega_k)$ yields

$$\lambda_k = \sqrt{\Delta\omega_k \tilde{G}(\omega_k)}\,. \tag{5}$$

The weighting coefficients ρ_k, $k = 1,2,...,N$, are used in relation (1), in order to compensate the band-pass filtering effects on the values of parameters λ_k calculated from (4) and (5).

For generating sample functions of the random process $\tilde{y}(t)$, $0 \le t \le T$, the following algorithm is proposed:

Step 1. Choose a sampling time interval Δt in order to produce the Nyquist folding frequency higher than the highest frequency of practical interest in the given power spectral density $G(\omega)$.

Step 2. Generate N time series of independent random numbers $u_k(t_{kl})$, $k = 1,2,...,N$, $l = 0,1,2,...,l(k)$ uniformly distributed in $[0,1)$.

Step 3. Generate N independent time series of random deviates $A_k(t_{kl})$, $k = 1,2,...,N$, $l = 0,1,2,...,l(k)$ from Rayleigh distributions with parameters λ_k by using the inverse function of Rayleigh cumulative distribution:

$$A_k(t_{kl}) = \lambda_k \sqrt{-2\ln\left[1 - u_k(t_{kl})\right]}, \quad l = 0,1,2,...,l(k)\,. \tag{6}$$

Step 4. Generate a set of independent random numbers $\theta_k, k = 1,2,...,N$ uniformly distributed in the interval $[0,2\pi)$.

Step 5. Determine $A_k(t_i)$, $k = 1,2,...,N, i = 1,2,...,M$, by linear interpolation of $A_k(t_{kl})$.

Step 6. Generate the time series

$$\tilde{y}(t_i,\rho_1,...,\rho_N) = \sum_{k=1}^{N} \rho_k A_k(t_i)\cos(\omega_k t_i + \theta_k)\,, \tag{7}$$

for an initial set of weighting coefficients values (e.g. $\rho_k = 1$, $k = 1,2,...,N$).

Step 7. Filter the generated sample time history (7) with the chosen band-pass filters and calculate the values of its spectral density at centre frequencies from

$$\tilde{G}(\omega_k) = \frac{\tilde{\sigma}^2(\omega_k, \Delta\omega_k)}{\Delta\omega_k}\,. \tag{8}$$

Step 8. Determine the values of weighting coefficients ρ_k, $k = 1,2,...,N$ by using an optimization procedure like genetic algorithms (GA) [13] or trial and error methods with respect to the criterion

$$\frac{\left|\tilde{G}(\omega_k) - G(\omega_k)\right|}{G(\omega_k)} < \varepsilon, \quad k = 1,2,...,N\,, \tag{9}$$

where ε is a convenient threshold for the relative error.

If a spectral analysis with constant percentage bandwidth filters is considered, than the ratio of two consecutive centre frequencies is constant, i.e.

$$\frac{\omega_{k+1}}{\omega_k} = \beta, \quad k = 1,2,...,N-1\,. \tag{10}$$

Therefore if the frequency range for spectral analysis is $[\omega_{\min}, \omega_{\max}]$ the total number of centre frequencies is

$$N \cong 1 + \frac{\log\omega_{\max} - \log\omega_{\min}}{\log\beta}\,. \tag{11}$$

3. APPLICATION OF THE SIMULATION METHOD

In the following applications of the proposed simulation method, the power spectral densities of simulated time histories are estimated from equation (4) by using third-octave band-pass filters centred at preferred frequencies defined in ISO R 266. Although nominal frequencies are used to identify the filters, the true centre frequencies of third octave filters are calculated from $10^{n/10}$, where $n = 0,1,2,...$ is the band number. The extending of preferred frequencies defined in ISO R 266 below 1 Hz can be obtained for negative integer values of n. Therefore, the ratio of two consecutive centre frequencies of third octave filters is $\beta = \frac{\omega_{k+1}}{\omega_k} = 10^{1/10} \cong 2^{1/3}$. In this case,

$$\omega_{\min} = 2\pi \cdot 10^{q/10} \text{ rad/s}, \; \omega_{\max} = 2\pi \cdot 10^{p/10} \text{ rad/s}, \tag{12}$$

where $p > q$ are integer numbers. The application of relation (11) yields

$$N = p - q + 1. \tag{13}$$

The proposed method is applied to simulate the road input with the target PSD expressed by a rational function of two polynomials of ω^2 [2, 3, 4, 15]:

$$G_{\mathrm{T}}(\omega) = \frac{2\sigma_{\mathrm{T}}^2}{\pi} \frac{aV\left[\omega^2 + (a^2 + b^2)V^2\right]}{\omega^4 + 2\left(a^2 - b^2\right)V^2\omega^2 + \left(a^2 + b^2\right)^2 V^4}, \tag{14}$$

where V is the running speed, a, b are coefficients depending on type of road and σ_{T} denotes the standard deviation of road irregularities. For numerical simulation was considered the PSD of a paved road input, given by (14) for the following values involved parameters [15]: $a = 0.32\text{m}^{-1}$, $b = 0.64\text{m}^{-1}$, $\sigma_{\mathrm{T}} = 1.7 \cdot 10^{-2}$ m, $V = 20\text{m/s}$.

By applying proposed method for the threshold of relative error $\varepsilon = 0.1$, the following values of weighting coefficients were obtained:

$$\begin{aligned} &\rho_1 = 1.12,\ \rho_2 = 1.57,\ \rho_3 = 1.1,\ \rho_4 = 1.2,\ \rho_5 = 1.07,\ \rho_6 = 1.08,\ \rho_7 = 1.1, \\ &\rho_8 = 1.03,\ \rho_9 = 1.13,\ \rho_{10} = 1.08,\ \rho_{11} = 1.05,\ \rho_{12} = 1,\ \rho_{13} = 1,\ \rho_{14} = 1.05, \\ &\rho_{15} = 1.1,\ \rho_{16} = 1.1,\ \rho_{17} = 1.1,\ \rho_{18} = 1.05,\ \rho_{19} = 1.15,\ \rho_{20} = 1.16,\ \rho_{21} = 1.25. \end{aligned} \tag{15}$$

The results are presented in Figs. 1 and 2, where subscripts T and R denote the target PSD and the simulated functions obtained by using Rayleigh distribution.

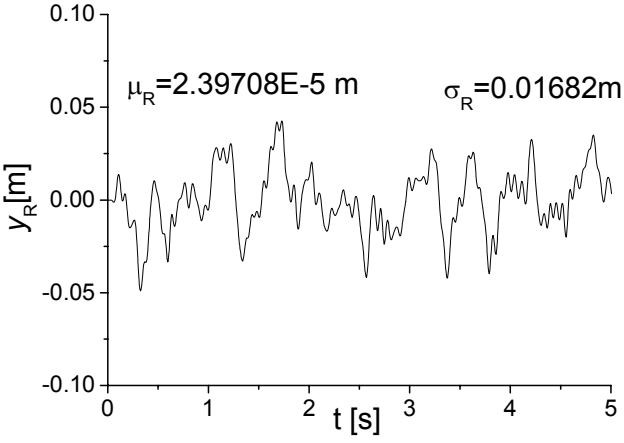

Fig. 1 – Sample of simulated road input for target PSD.

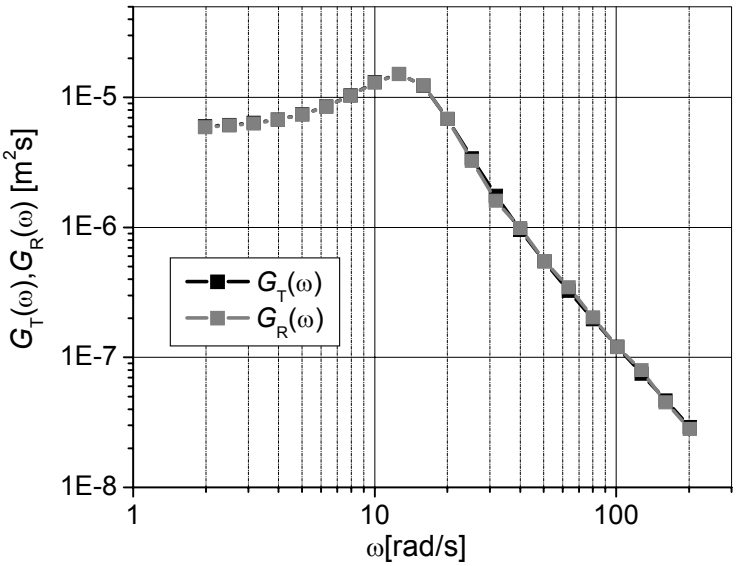

Fig. 2 – Target PSD and approximate PSD, $G_R(\omega)$, obtained from simulated road input.

4. VALIDATION OF SIMULATION METHOD THROUGH THE OF RESPONSE OF A QUARTER CAR MODEL

In this section, the quarter-car model shown in Fig. 3 is used to compare the vehicle response to the above generated road profile input with that obtained analytically by using input-output relationships for linear physical systems. The vehicle is assumed to travel at a constant forward speed V. It is also assumed that the road-tire contact is a point that follows the road profile at all times.

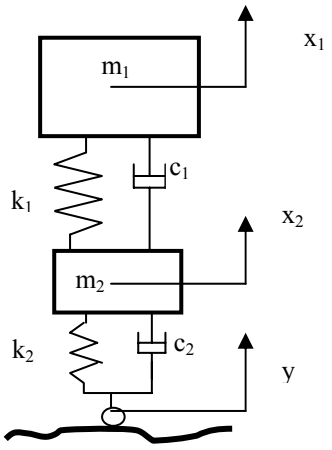

Fig. 3 – The quarter-car model of the vehicle.

The equations of motion can be written as

$$\begin{aligned} &m_1\ddot{x}_1 + c_1\left(\dot{x}_1 - \dot{x}_2\right) + k_1\left(x_1 - x_2\right) = 0 \\ &m_2\ddot{x}_2 - c_1\left(\dot{x}_1 - \dot{x}_2\right) + c_2\left(\dot{x}_2 - \dot{y}\right) - k_1\left(x_1 - x_2\right) + k_2\left(x_2 - y\right) = 0, \end{aligned} \tag{16}$$

where $y(t)$ is the road input for a travelling speed V.

The matrix of frequency response functions of system (16) is obtained as [5, 9, 15]

$$\mathbf{H}_{\mathrm{xy}}(\omega) = -\left[-\omega^2\mathbf{M} + \mathrm{i}\omega\mathbf{C} + \mathbf{K}\right]^{-1} \cdot \left[\mathrm{i}\omega\mathbf{C}_0 + \mathbf{K}_0\right], \tag{17}$$

where the matrices $\mathbf{M},\mathbf{C},\mathbf{K},\mathbf{C}_0,\mathbf{K}_0$ are given by

$$\mathbf{M} = \begin{vmatrix} m_1 & 0 \\ 0 & m_2 \end{vmatrix},\ \mathbf{C} = \begin{vmatrix} c_1 & -c_1 \\ -c_1 & c_1 + c_2 \end{vmatrix},\ \mathbf{K} = \begin{vmatrix} k_1 & -k_1 \\ -k_1 & k_1 + k_2 \end{vmatrix},\ \mathbf{C}_0 = \begin{vmatrix} 0 \\ -c_2 \end{vmatrix},\ \mathbf{K}_0 = \begin{vmatrix} 0 \\ -k_2 \end{vmatrix}. \tag{18}$$

The matrix of frequency response functions the quarter car model can be given the form

$$\mathbf{H}_{\mathrm{xy}}(\omega) = \begin{bmatrix} H_{\mathrm{x_1y}}(\omega) \\ H_{\mathrm{x_2y}}(\omega) \end{bmatrix}. \tag{19}$$

The output spectral density matrix is obtained from [9, 10, 14].

$$\mathbf{G}_{\mathrm{x}}(\omega) = \begin{vmatrix} G_{\mathrm{x_1}}(\omega) & G_{\mathrm{x_1x_2}}(\omega) \\ G_{\mathrm{x_2x_1}}(\omega) & G_{\mathrm{x_2}}(\omega) \end{vmatrix} = \overline{\mathbf{H}_{\mathrm{xy}}(\omega)}\ G_{\mathrm{y}}(\omega)\ \mathbf{H}^{\mathrm{T}}_{\mathrm{xy}}(\omega). \tag{20}$$

The r.m.s. values of the absolute acceleration of sprung and unsprung masses can be calculated from

$$\sigma_{\ddot{x}_1} = \sqrt{\int_{\omega_{\min}}^{\omega_{\max}} \omega^4 G_{\mathrm{x_1}}(\omega)\mathrm{d}\omega},\ \sigma_{\ddot{x}_2} = \sqrt{\int_{\omega_{\min}}^{\omega_{\max}} \omega^4 G_{\mathrm{x_2}}(\omega)\mathrm{d}\omega}. \tag{21}$$

The r.m.s. sprung mass acceleration is considered as a ride quality parameter, while the r.m.s. value of dynamic road-tire contact force $F_{\mathrm{c}}(t) = k_2\left[x_2(t) - y(t)\right]$ is used for road holding assessment. The frequency response function of road-tire contact force can be written as

$$H_{\mathrm{F_cy}}(\omega) = k_2\left[H_{\mathrm{x_2y}}(\omega) - 1\right]. \tag{22}$$

The power spectral density and r.m.s. value of the contact force are given by:

$$G_{\mathrm{F_c}}(\omega) = \left|H_{\mathrm{F_cy}}(\omega)\right|^2 G_{\mathrm{y}}(\omega),\ \sigma_{\mathrm{F_c}} = \sqrt{\int_{\omega_{\min}}^{\omega_{\max}} G_{\mathrm{F_c}}(\omega)\mathrm{d}\omega}. \tag{23}$$

Neglecting the tire internal damping, the vehicle system parameters for the quarter-car model are given in Table 1. They are typical for a medium size passenger car [15].

Table 2

$m_1[\mathrm{kg}]$	$m_2[\mathrm{kg}]$	$k_1[\mathrm{N/m}]$	$k_2[\mathrm{N/m}]$	$c_1[\mathrm{Ns/m}]$	$c_2[\mathrm{Ns/m}]$
265	31.5	11 370	167 000	835	0

The system amplification factors $\left|H_{\mathrm{x_1y}}(\omega)\right|$, $\left|H_{\mathrm{x_2y}}(\omega)\right|$ and $\left|H_{\mathrm{F_cy}}(\omega)\right|/k_2$ are plotted in Fig. 4.

Considering the target PSD given by (14) and previously simulated sample function $y_{\mathrm{R}}(t)$ as the input of the quarter car model shown in Fig. 3, the system outputs $x_{1\mathrm{R}}(t)$, $x_{2\mathrm{R}}(t)$ were obtained by numerical integration of the equations (16) and their power spectral densities $G_{\mathrm{x_1R}}(\omega), G_{\mathrm{x_2R}}(\omega)$ were determined by filtering method using the same set of third-octave filters. Next, the relation $(23)_1$ yields the spectral density $G_{F_{\mathrm{c}}\mathrm{R}}(\omega)$. Figure 5 shows comparatively the predicted and simulated power spectral densities.

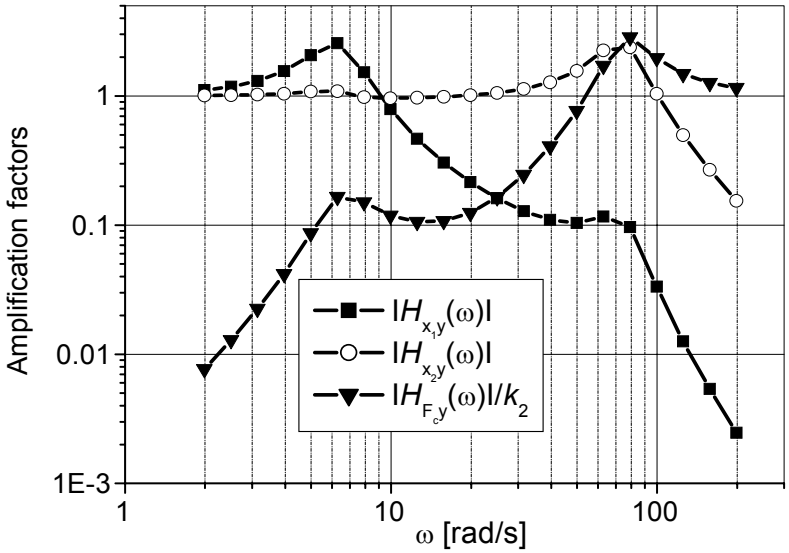

Fig. 4 – Amplification factors of quarter-car model.

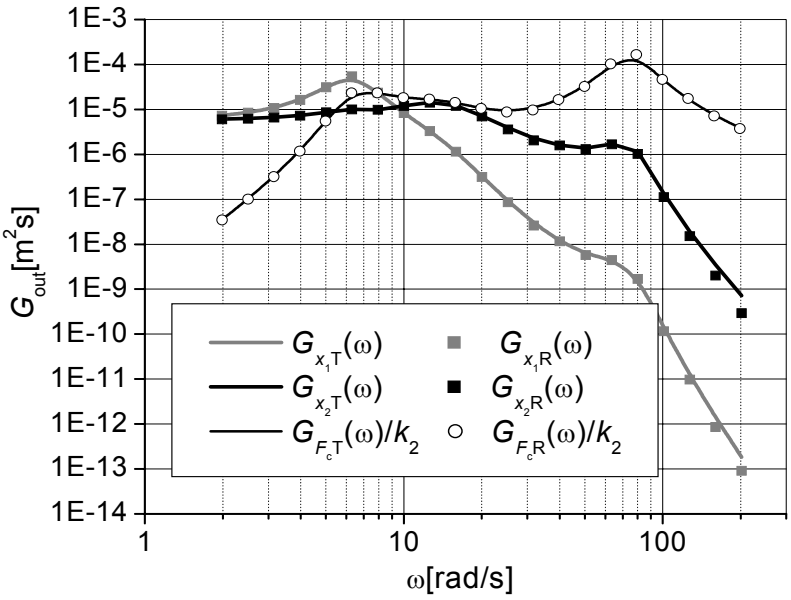

Fig. 5 – Predicted and simulated output power spectral densities.

The mean square of the simulated absolute accelerations and road-tire contact force can be derived straightforward from (21) and $(23)_2$. The results are shown in Table 2.

Table 2

RMS output	$\sigma_{\ddot{x}_1}\left[\mathrm{m/s^2}\right]$	$\sigma_{\ddot{x}_2}\left[\mathrm{m/s^2}\right]$	$\sigma_{F_c}\left[\mathrm{kN}\right]$
Predicted	2.28	43.9	1.433
Simulated	2.21	41.1	1.432

The results presented in Fig. 5 and Table 2 show that the proposed method for generation of time series compatible with a given PSD can provide a sufficient statistical description of a road input as a realization of a Gaussian stationary random process with zero-mean value. Therefore, the simulated sample functions can be used to determine the response of a vehicle traversing the road by means of analytical or numerical simulation methods.

5. CONCLUSIONS

In this paper, an effective approach to the simulation of wide-sense stationary random time series, defined by its PSD, is presented. A sample function of the target random process is represented by a superposition of weighted statistically independent sine waves with uniformly distributed phase angles and random envelopes following Rayleigh distributions. As all components of this representation are deviates from Gaussian distributions, the sampling distribution function of the resulting random time series approaches a Gaussian distribution for reasonable large number of frequencies chosen within the effective frequency bandwidth of target PSD. The proposed method gives the possibility to simulate with good accuracy time series compatible with any given analytical expression or experimental data for power spectral density.

The method is illustrated by the simulation of road input with specified rational power spectral density. The results show a good agreement between the power spectral density of the generated road input and the target one. The method is validated through comparison of the predicted response of a quarter car model for the given road input PSD with that obtained for the simulated road input compatible with the same PSD.

REFERENCES

1. T.K. Caughey, *Nonlinear Theory of Random Vibrations*, Advances in Applied Mechanics, **11**, pp. 209–253, 1971.
2. A. Hac, *Adaptive control of vehicle suspension*, Vehicle System Dynamics, **16**, pp. 57–74, 1987.
3. D. Stăncioiu, T. Sireteanu, M. Giuclea and A.M. Mitu, *Simulation of random road profiles with specified spectral density*, Proceedings of the Annual Symposium of the Institute of Solid Mechanics, Bucharest, Romania, pp. 331–338, 2003.
4. F. Tyan, Y.-F. Hong, S.-H. Tu and W. S. Jent, *Generation of random road profiles*, Journal of Advanced Engineering, pp. 1373–1378, 2009.
5. S. Turkay and H. Akcay, *A study of random vibration characteristics of the quarter-car model,* Journal of Sound and Vibration, **282**, pp. 111–124, 2005.
6. International Organization for Standardization, *Mechanical vibration-road surface profiles – reporting of measured data*, ISO 8608, 1995.
7. S. O. Rice, *Mathematical analysis of random noise*, in: N. Wax (Ed.), *Selected Papers on Noise and Stochastic Processes*, New York, Dover Publications Inc., 1954, pp. 180–181.
8. M. Shinozuka and C.-M. Jan, *Digital simulation of random processes and its applications*, Journal of Sound and Vibration, **25**, pp. 111–128, 1972.
9. G. Verros, S. Natsiavas and C. Papadimitriou, *Design optimization of quarter-car models with passive and semi-active suspensions under random road excitation*, Journal of Vibration and Control, **11**, pp. 581–606, 2005.
10. Y.K.Lin, *Probabilistic Theory of Structural Dynamics*, McGraw-Hill Inc., New York, 1967.
11. J.S. Bendat and A.G. Piersol, *Random Data: Analysis and Measurement Procedures*, John Wiley&Sons, Inc., NewYork, 1971.
12. W.A. Gardner, *Introduction to Random Processes with Applications to Signals and Systems*, McGraw-Hill Inc.,New York, 1989.
13. Z. Michalewicz, *Genetic Algorithms + Data Structures = Evolution Programs*, Springer Verlag, 1992.
14. C.J. Dodds and J.D. Robson, *The Description of Road Surface Roughness*, Journal of Sound and Vibration, **31**, pp. 175–184, 1973.
15. T. Sireteanu, O. Gündisch and S. Părăianu, *Random vibrations of automobiles*, Edit. Tehnică, Bucharest, 1981.

Received February 7, 2014

THE PUBLISHING HOUSE
OF THE ROMANIAN ACADEMY

PROCEEDINGS OF THE ROMANIAN ACADEMY, Series A,
Volume 15, Number 3/2014, pp. 300–309

APPLICATION OF A GTN DAMAGE MODEL TO PREDICT THE FRACTURE OF METALLIC SHEETS SUBJECTED TO DEEP-DRAWING

Abdolvahed KAMI [1], Bijan MOLLAEI DARIANI [1], Ali SADOUGH VANINI [1], Dan-Sorin COMSA [2], Dorel BANABIC [2]

[1] Amirkabir University of Technology, Department of Mechanical Engineering, Tehran, Iran
[2] Technical University of Cluj-Napoca, CERTETA Research Centre, Cluj-Napoca, Romania
E-mail: dariani@aut.ac.ir

In this paper, an anisotropic formulation of the Gurson-Tvergaard-Needleman (GTN) damage model is used for simulating the deep-drawing of a rectangular box made from an AA6016-T4 metallic sheet. The model is implemented as a VUMAT routine in the ABAQUS/Explicit finite-element code. The material parameters involved in the constitutive relationships are determined by means of an identification procedure that combines the response surface methodology (RSM) and the simulation of a uniaxial tensile test. In order to assess the predictive performances of the GTN model, different levels of the blank-holding force are assumed in the finite-element analysis of the deep-drawing process. The comparison between the numerical results and experimental data shows not only a good accuracy of the fracture predictions, but also the capability of the GTN model to provide a realistic description of the material response during the whole forming process.

Key words: deep-drawing, fracture, GTN Damage model, anisotropy.

1. INTRODUCTION

Aluminium alloys have become attractive for the automotive industry mainly because of their light weight. In the form of cold rolled thin sheets, such materials are used to produce car body panels by deep-drawing operations. Because of their special anisotropy characteristics, sheets made from aluminium alloys are prone to fracture when large strains are induced during the forming process. In practical applications, it is very important to predict such undesirable phenomena. One of the theoretical models developed with this aim in view is due to Gurson [1]. According to Gurson's approach, the degradation of the load carrying capacity and finally the fracture of ductile metals are caused by the evolution of voids. In its original formulation, the model takes into account only the growth of pre-existing voids, without assuming any generative mechanisms. In order to overcome this limitation, Tvergaard and Needleman [2–4] proposed mathematical descriptions of the void nucleation and coalescence. This modified model is known as Gurson-Tvergaard-Needleman (GTN) damage model.

Both models (Gurson and GTN) assume that the metal matrix is isotropic and obeys the von Mises yield function. In fact, because of the cold rolling production procedure, sheet metals usually exhibit a non-negligible anisotropic behaviour. Many attempts have been made to include the anisotropy of the matrix material in the GTN model. Liao et al. [5] derived an approximate potential closed to the original Gurson formulation, in which the Hill's quadratic [6] and non-quadratic [7] anisotropic expressions of the equivalent stress are used to describe the anisotropy. They used anisotropy parameters defined as the ratio of the transverse plastic strain rate to the through-thickness plastic strain rate under in-plane uniaxial loading along different directions. Wang et al. [8] proposed to use the average anisotropy parameter instead of the directional parameters in the model proposed by Liao et al. [5]. Chen and Dong [9] extended the GTN model to characterize the matrix material through Hill quadratic [6] and Barlat-Lian 3-component [10] expressions of the equivalent stress. Chen and Dong [11] proposed extensions of the GTN potential based on Hill's quadratic anisotropic expression of the equivalent stress [6].

Various anisotropic GTN models have been successfully used for predicting the fracture occurrence in sheet metal forming processes [11–13]. In this paper, a GTN model based on Hill's quadratic expression of the equivalent stress is used for simulating the deep-drawing of a rectangular box made from an AA6016-T4 metallic sheet. The model is implemented as a VUMAT routine in the ABAQUS/Explicit finite-element code [14]. The material parameters involved in the constitutive relationships are determined by means of an identification procedure that combines the response surface methodology (RSM) and the simulation of a uniaxial tensile test.

2. GTN DAMAGE MODEL

2.1. GTN model based on HILL'48 expression of the equivqlent stress

As previously mentioned, both the original Gurson model [1] and the GTN version developed by Tvergaard and Needleman [2–4] assume the plastic isotropy of the matrix material. However, the experimental data obtained from mechanical tests show that cold rolled sheet metals are anisotropic bodies. In recent years, many attempts have been made to develop anisotropic formulations of the GTN model [5,8, 9, 11]. The expression of the equivalent stress proposed by Hill in 1948 [6] is able to give a sufficiently good description of the plastic anisotropy exhibited by the sheet metals used in industrial applications. This fact, as well as the computational efficiency ensured by its quadratic form, determined the authors to include Hill'48 equivalent stress in the ABAQUS/Explicit implementation of the GTN model.

Hill'48 equivalent stress is expressible as follows [6]:

$$\bar{\sigma} = \left[F(\sigma_{22} - \sigma_{33})^2 + G(\sigma_{33} - \sigma_{11})^2 + H(\sigma_{11} - \sigma_{22})^2 + 2L\sigma_{23}^2 + 2M\sigma_{31}^2 + 2N\sigma_{12}^2 \right]^{1/2}. \tag{1}$$

The quantities denoted as σ_{ij} (i, j = 1, 2, 3) in Eq. (1) are Cartesian components of a corotational Cauchy stress tensor expressed in a frame that follows the local rotation of the anisotropy axes, while F, G, H, L, M, and N are material constants. The parameters F, G, H, L, M, and N can be evaluated using different types of experimental data. In the case of metallic sheets, the standard identification procedure relies on the Lankford coefficients r_0, r_{45} and r_{90} obtained from uniaxial tensile tests performed on specimens cut at 0°, 45° and 90° with respect to the rolling directions. The following relationships can be used to evaluate the parameters F, G, H, L, M, and N when these coefficients are available:

$$\begin{aligned} &F = \frac{H}{r_{90}}, \quad G = \frac{H}{r_0}, \quad H = \frac{r_0}{r_0 + 1}, \\ &L = M = \frac{3}{2}, \quad N = \frac{(r_0 + r_{90})(2r_{45} + 1)}{2r_{90}(r_0 + 1)}. \end{aligned} \tag{2}$$

The general form of the GTN damage potential is:

$$\Phi = \left(\frac{\bar{\sigma}}{Y} \right)^2 + q_1 f^* \left[2\cosh\left(-q_2 \frac{3p}{2Y} \right) - \frac{q_3}{q_1} f^* \right] - 1, \tag{3}$$

where $\bar{\sigma}$ is the equivalent stress defined by Eq. (1),

$$p = -(\sigma_{11} + \sigma_{22} + \sigma_{33})/3 \tag{4}$$

is the hydrostatic pressure, Y is the yield stress of the matrix material defined as a function of the equivalent plastic strain $\bar{\varepsilon}^p$ by means of Swift's hardening law

$$Y(\bar{\varepsilon}^p) = K(\varepsilon_0 + \bar{\varepsilon}^p)^n, \tag{5}$$

and

$$f^* = \begin{cases} f, & \text{if} \quad f \le f_c, \\ f_c + \dfrac{f_f^* - f_c}{f_f - f_c}(f - f_c), & \text{if} \quad f_c < f < f_f, \\ f_f^*, & \text{if} \quad f \ge f_f \end{cases} \tag{6}$$

is a porosity parameter depending on the current void volume fraction f. The quantity f^* has been introduced by Tvergaard and Needleman [0] to describe the accelerated loss of load carrying capacity due to the coalescence of voids. All the other symbols occurring in Eqs (3), (5) and (6) are material constants.

The inequality $\Phi \le 0$ defines all the admissible stress states of the sheet metal. More precisely,

$$\begin{cases} \Phi < 0, & \text{in elastic states,} \\ \Phi = 0, & \text{in elastoplastic states.} \end{cases} \tag{7}$$

With this observation, the flow rule associated to the GTN potential can be expressed in the form

$$\dot{\boldsymbol{\varepsilon}}^{(p)} = \dot{\lambda}\frac{\partial \Phi}{\partial \boldsymbol{\sigma}}, \qquad \text{where} \begin{cases} \dot{\lambda} = 0, & \text{if } \Phi < 0, \\ \dot{\lambda} \ge 0, & \text{if } \Phi = 0. \end{cases} \tag{8}$$

In the above relationship, $\dot{\boldsymbol{\varepsilon}}^{(p)}$ is the plastic part of the strain rate tensor.

The change of the void volume fraction f is caused by the growth of the initial void volume fraction f_0 and the nucleation of new voids at the limits of the second phase particles and inclusions:

$$\dot{f} = \dot{f}_{growth} + \dot{f}_{nucleation} \tag{9}$$

where

$$\dot{f}_{growth} = (1 - f)\left[\dot{\varepsilon}_{11}^{(p)} + \dot{\varepsilon}_{22}^{(p)} + \dot{\varepsilon}_{33}^{(p)}\right] \tag{10}$$

and

$$\dot{f}_{nucleation} = \frac{f_N}{S_N\sqrt{2\pi}} \exp\left[-\frac{1}{2}\left(\frac{\bar{\varepsilon}^{(p)} - \bar{\varepsilon}_N}{S_N}\right)^2\right]. \tag{11}$$

The quantities denoted as S_N, $\bar{\varepsilon}_N$ and f_N in Eq. (11) are also material constants that must be determined by identification.

2.2. Identification procedure

Among the material constants included in the constitutive relationships presented above, $q_1, q_2, q_3, f_0, f_c, f_f, f_N, S_N,$ and $\bar{\varepsilon}_N$ need a special attention, because the predictive performances of the GTN model are strongly dependent on their values. In general, an identification procedure that tries to determine all these parameters would be very inefficient because of the large amount of experimental data needed for calibration. On the other hand, the success of such an approach would be also improbable in many cases due to the non-uniqueness of the solution [15, 16]. Most of the researchers use the values proposed by Needleman and Tvergaard for q_1, q_2, q_3, S_N and $\bar{\varepsilon}_N$ parameters, namely, $q_1 = 1.5,\ q_2 = 1,$ $q_3 = q_1^2 = 2.25,\ S_N = 0.1,$ and $\bar{\varepsilon}_N = 0.3$ [0, 0]. In this paper, with the aim of simplifying the identification procedure, this approach will be adopted. As a consequence, only the remaining parameters $f_0, f_c, f_f,$ and f_N should be found. For their determination, the authors have developed an identification procedure based on the response surface methodology (RSM). A face centred central composite RSM design of experiments

has been implemented in the software package Design-Expert® (trial version 7.0.0). These experiments are uniaxial tensile tests as shown in Fig. 4. A total number of 27 experiments with different parameter (factor) combinations have been performed (see Table 1).

Table 1

Different values of the identification factors

Factor	Values		
f_0	0.0001	0.00055	0.001
f_N	0.001	0.0255	0.05
f_c	0.005	0.0275	0.05
f_f	0.06	0.13	0.2

The response of the experiments has been defined by means of Eq. (12), where $|\square|$ is the absolute value

$$\text{Response} = \sum_{i=1}^{n} \left| F_{exp} - F_{num} \right|_i . \tag{12}$$

The quantities denoted as F_{exp} and F_{num} in Eq. (12) are experimental and numerically predicted values of the tensile force acting on the specimen for different elongation stages individualized by the index *i*. The total elongation of the gauge (up to the fracture occurrence) was assumed to be 25 mm. One should mention that, in the experimental tensile tests, the fracture occurred at about 21.48 mm elongation for the specimens cut along the rolling direction. On the other hand, when using the RSM based identification procedure, different combinations of factors lead to different predictions for the fracture elongation (smaller than 21.48 mm or even larger than 30 mm). The authors noticed that the function expressed by Eq. (12) was able to provide quite reasonable values of the RSM design response when an "averaged" value of the fracture elongation of 25 mm was adopted. For all the experiments included in the RSM design, the values of the force were set to zero between the fracture point and the maximum elongation of 25 mm. The summation limit *n* in Eq. (12) was set to 1000. The results of the identification procedure for the case of an AA6016-T4 sheet metal (1 mm thickness) will be presented in §5.1.

3. EXPERIMENTS

3.1. Uniaxial tensile tests

The material adopted in the experimental research is an AA6016-T4 metallic sheet with the nominal thickness of 1 mm. AA6016-T4 is an Al-Mg-Si alloy currently used in the automotive industry for the production of deep-drawn outer panels. This material has a good formability in the T4 temper state, low springback, good weldability and high corrosion resistance. The uniaxial tensile tests have been performed on specimens cut at 0, 45 and 90° with respect to the rolling direction. In all cases, rectangular specimens with the dimensions $200\,\text{mm} \times 20\,\text{mm} \times 1\,\text{mm}$ have been used. Their elongation has been measured with an extensometer having the gauge length of 80 mm. The testing methodology is presented in [0]. Figure 1 shows some representative results of the uniaxial tensile tests. A summary of the material properties obtained from these experiments is given in Table 2: Lankford coefficients (r), conventional yield stress ($R_{p0.2}$) and ultimate tensile strength (R_m).

The material curves recorded by the tensile testing equipment in the case of the specimens cut along the rolling direction have been also used for the calibration of Swift's hardening law (see Eq. (5)). The authors have developed an identification procedure based on the least squares method. The following values of the coefficients K, ε_0 and n have been obtained in this way: $K = 525.77$ MPa, $\varepsilon_0 = 0.011252$ and $n = 0.2704$.

Finally, the uniaxial tensile tests have also provided the elastic properties of the material. The average values of Young's modulus (E) and Poison's ratio (ν) are 70 GPa and 0.33, respectively.

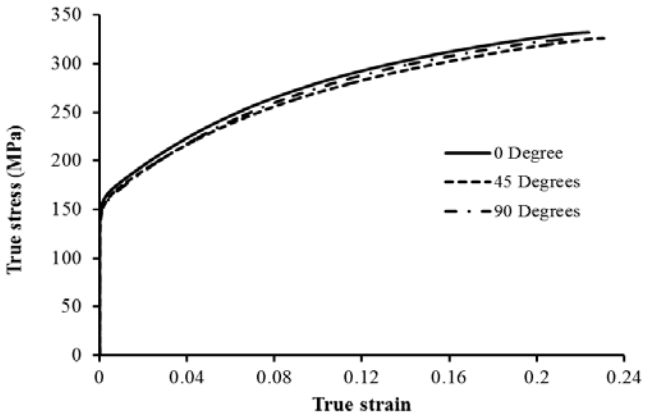

Fig. 1 – Material curves obtained by uniaxial tensile tests performed at 0°, 45° and 90° with respect to the rolling direction (AA6016-T4 sheet metal; 1 mm thickness).

Table 2

Mechanical properties of the AA6016-T4 sheet metal (1 mm thickness)

Orientation	r	$R_{p0.2}$ [MPa]	R_m [MPa]
0°	0.5529	158.07	264.89
45°	0.4091	152.25	259.84
90°	0.5497	154.75	263.32

3.2. Deep-drawing equipament

Fig. 2 shows the tooling setup used in the deep-drawing experiments [20]. The tests have been performed on circular blanks with 85 mm diameter lubricated on both faces with a mixture of oil and graphite. In all cases, the punch speed has been set to a constant value of 33 mm/min. Deep drawing tools have been installed on the Erichsen universal testing machine (Fig. 3) which ensures a hydraulic control of the blank holding force and punch displacement. Different values of the blank holding force have been adopted in the experiments. For values lower than 4 kN, the flange has been affected by wrinkling, while holding forces greater than 10 kN have caused the fracture of the deep-drawn parts. The experimental results obtained in the case of the maximum holding force (10 kN) will be used for comparison with the predictions of the GTN model.

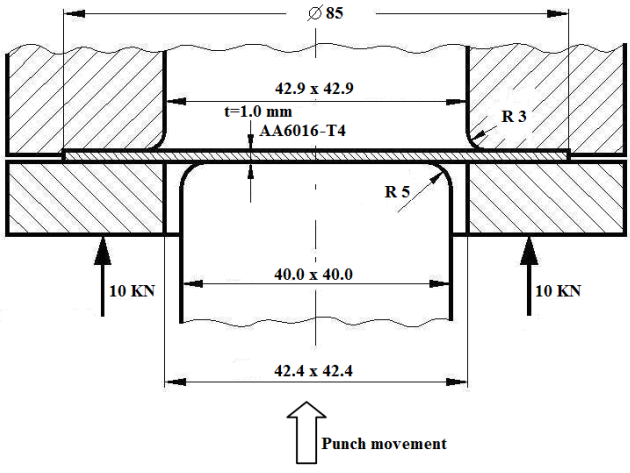

Fig. 2 – Tooling setup used in the deep-drawing experiments [20].

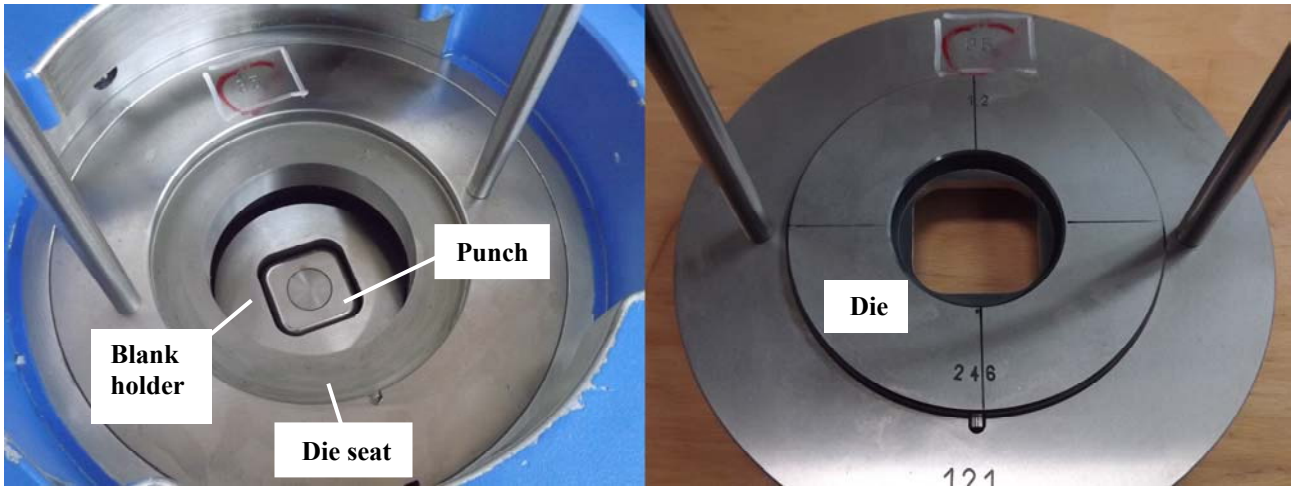

Fig. 3 – Deep-drawing tools installed on the Erichsen universal testing machine.

4. NUMERICAL ANALYSIS

The numerical analysis has been focused on the finite-element simulation of the uniaxial tensile tests and deep-drawing experiments. In all cases, the commercial code ABAQUS/Explicit has been used in combination with the anisotropic GTN damage model implemented as a VUMAT routine.

4.1. Simulation of the uniaxial tensile tests

As discussed in the previous sections, the RSM design of experiments has been used for the identification of the GTN model. The response values for this design have been calculated from force vs. displacement curves corresponding to uniaxial tensile loads. For this reason, uniaxial tensile tests have been numerically simulated. The finite element model used in the numerical analysis has been reduced to the gauge section of the rectangular specimens. The boundary conditions and dimensions of the analysis domain are shown in Fig. 4. A total displacement of 25 mm has been applied at the right end of the finite element mesh. Hexahedral elements with 8 nodes (C3D8R) and the edge size of 0.5 mm have been used for meshing the analysis domain.

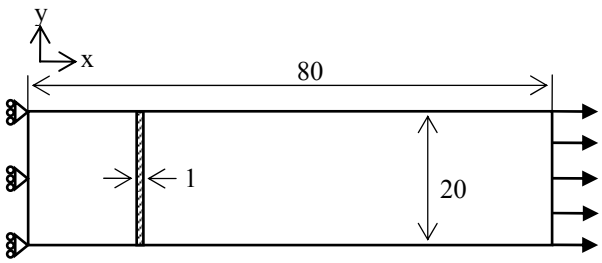

Fig. 4 – Geometry and boundary conditions of the AA6016-T4 specimen (simulation of a uniaxial tensile test).

4.2. Simulation of deep-drawing experiments

The essential surfaces of the tools (punch, die and blank holder) have been meshed using rigid shell elements (R3D4), while solid deformable elements (8-node hexahedra C3D8R with the average edge size of 0.5 mm) have been adopted for meshing the circular blank. Due to the geometric and mechanical symmetry of the deep-drawing process, only one quarter of the tool surfaces and blank volume have been included in the finite-element model. Three layers of solid elements have been generated in the thickness direction of the blank. A concentrated force of 2.5 kN has been applied to the reference point of the blank holder (one quarter

of actual blank holding force – 10 kN). The die has been kept fixed in its position, the punch and the blank holder being allowed to perform vertical translations. The frictional contact between blank and tools has been modelled using a penalty formulation. Taking into account the lubrication conditions of the laboratory experiments, the friction coefficient has been set to a value of 0.05 on all the contact surfaces. The numerical simulation of the deep-drawing process has been divided in two steps: in the first stage, the blank holding force is raised up to its maximum force (2.5 kN); in the next stage, the punch performs a vertical translation until the occurrence of the fracture in the blank.

5. RESULTS AND DISCUSSIONS

5.1. Parameter identification

As previously mentioned, the parameters f_0, f_c, f_f and f_N have been determined using an identification procedure based on the response surface methodology. The optimum values of the parameters provided by this procedure are the following ones: $f_0 = 0.000242$, $f_c = 0.047674$, $f_f = 0.2$ and $f_N = 0.041546$. Numerical simulations of uniaxial tensile tests have been performed using these material constants. Figure 5 shows a comparison between the force *vs*. elongation curve predicted by the GTN model and the experimental curve obtained by averaging the results of the uniaxial tensile tests performed along the rolling direction. One may easily notice that the numerical results are in very good agreement with the experimental data. This fact allows concluding that the values of the parameters f_0, f_c, f_f and f_N obtained by identification are representative for the AA6016-T4 sheet metal with the nominal thickness of 1 mm and can be used for the simulation of more complex forming processes.

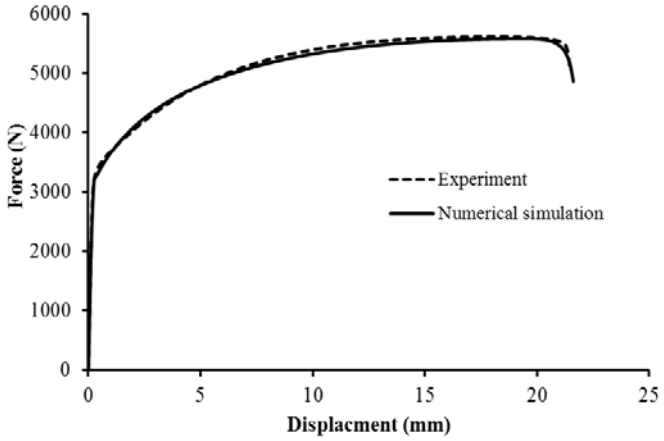

Fig. 5 – Force vs elongation curves corresponding to uniaxial tensile tests performed along the rolling direction (comparison between experimental results and numerical predictions).

Fig. 6 shows a comparison between the tensile specimens fractured during the experimental tests and the numerical simulations. The rectangle in Fig. 6a contains the gauge section which is used in the finite element analysis. After analysing this data, one may conclude that the numerical model with the identified values of the parameters is able to predict the fracture occurrence with an acceptable accuracy. The coloured map in Fig. 6b shows the distribution of the total void volume fraction (denoted as SDV2 in the legend).

Figure 7 presents several stages of a tensile test simulated with ABAQUS/Explicit: uniform distribution of the void volume fraction in a stage preceding the strain localization – Fig. 7a; different stages of the strain localization process characterized by an accelerated evolution of the void volume fraction that tends to accumulate in a narrow region as a consequence of the coalescence phenomenon – Fig. 7b, c, d.

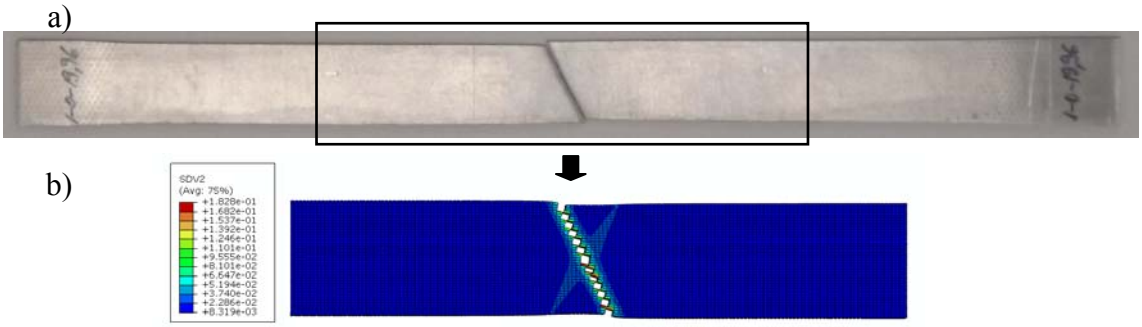

Fig. 6 – Tensile specimen after fracture a) experiment; b) numerical simulation.

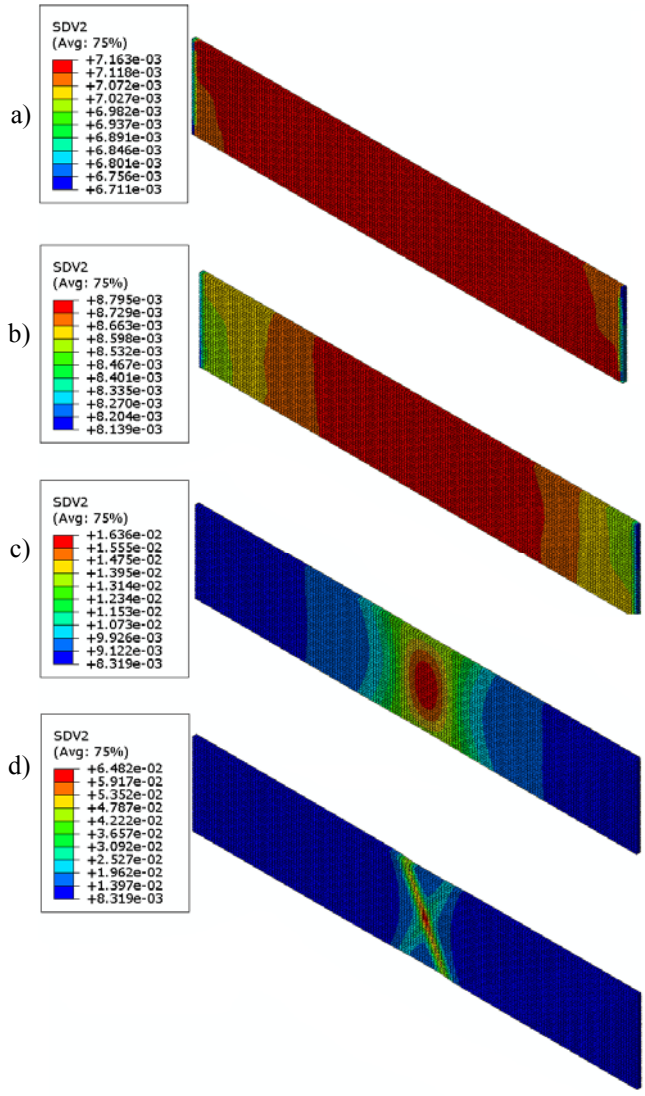

Fig. 7 – Evolution of the void volume fraction during the uniaxial tensile test:
a) 17.99 mm; b) 19.48 mm; c) 20.47 mm; d) 21.22 mm elongation.

5.2. Simulation of the deep-drawing process

Fig. 8 illustrates the fracture of the AA6016-T4 metallic sheet during the deep-drawing tests performed with a blank holding force set to 10 kN. This figure compares the predictions of the anisotropic GTN model with the experimental data. One may notice that fracture path has almost the same shape and position in both images.

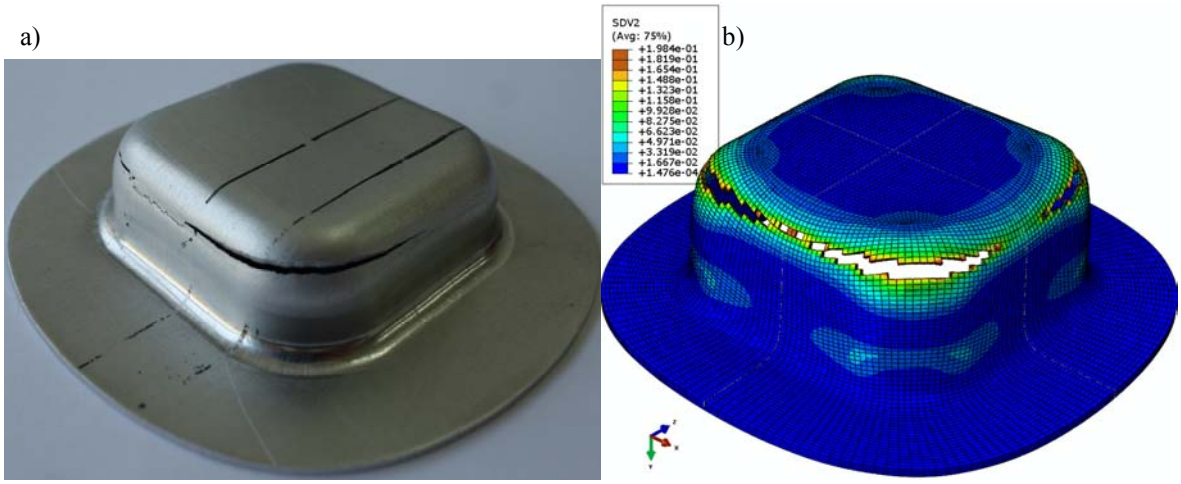

Fig. 8 – Fractured specimens: a) experiment; b) numerical simulation.

Fig. 9 shows the evolution of the punch force during the deep-drawing process. Experimental data and numerical predictions are superimposed on the same diagram. One may notice that the maximum level of the punch force predicted by ABAQUS/Explicit (32.27 kN) is almost equal to the experimentally determined value (34.24 kN). The diagram also allows the evaluation of the drawing depth at which the fracture occurs. This depth corresponds to the sudden drop of the punch force towards zero: 17.90 mm – predicted by ABAQUS/Explicit, in very good agreement with the depth of 18.70 mm measured on the experimental curve.

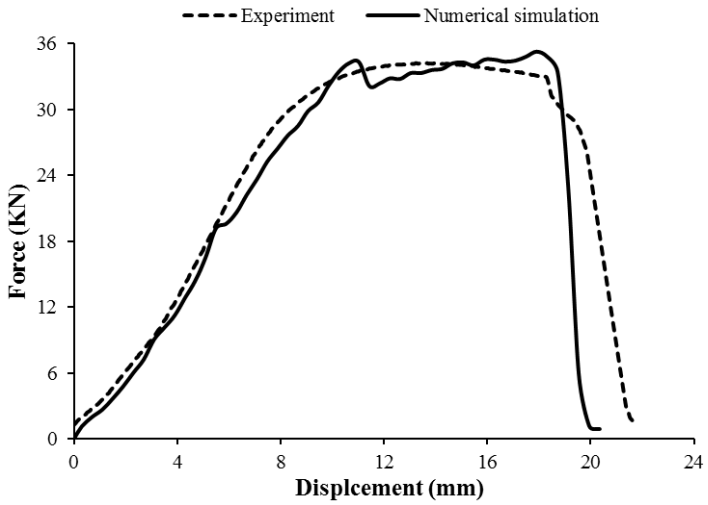

Fig. 9 – Comparison of forming forces for blank holder of 10 kN.

6. CONCLUSIONS

The GTN damage model combined with Hill'48 expression of the equivalent stress has been used to predict the fracture of metallic sheets subjected to deep-drawing. The material constants included in the formulation of the damage model have been calibrated using the response surface methodology. The identification procedure is quick and straightforward as the required material parameters are derived by conducting simple uniaxial tensile tests and their numerical simulation. The finite element simulation of a deep-drawing process has proved not only a good accuracy of the fracture predictions, but also the capability of the GTN model to provide a realistic description of the material response during the whole forming process (relative errors smaller than 5 % in the prediction of the maximum punch force and the drawing depth at which the fracture occurs).

REFERENCES

1. GURSON, A.L., *Continuum theory of ductile rupture by void nucleation and growth. Part I – Yield criteria and flow rules for porous ductile media*, J. Eng. Mater. Tech., **99**, *1*, pp. 2–15, 1977.
2. TVERGAARD, V., *Influence of voids on shear band instabilities under plane strain conditions*, Int. J. Fract., **17**, *4*, pp. 389–407, 1981.
3. TVERGAARD, V., *On localization in ductile materials containing spherical voids*, Int. J. Fract., **18**, *4*, pp. 237–252, 1982.
4. TVERGAARD, V., NEEDLEMAN, A., *Analysis of the cup-cone fracture in a round tensile bar*, Acta Metallurgica, **32**, *1*, pp. 157–169, 1984.
5. LIAO, K.C., PAN, J., TANG, S.C., *Approximate yield criteria for anisotropic porous ductile sheet metals*, Mech. Mater., **26**, *4*, pp. 213–226, 1997.
6. HILL, R., *A theory of the yielding and plastic flow of anisotropic metals*, Roy. Soc. London Proc. A, **193**, *1033*, pp. 281–297, 1948.
7. HILL, R., *Theoretical plasticity of textured aggregates*, Math. Proc. Camb. Phil., **85**, *1*, pp. 179–191, 1979.
8. WANG, D.A., PAN, J., LIU, S.D., *An Anisotropic Gurson Yield Criterion for Porous Ductile Sheet Metals with Planar Anisotropy*, Int. J. Damage Mech., **13**, *1*, pp. 7–33, 2004.
9. CHEN, Z., DONG, X., *Comparison of GTN damage models for sheet metal forming*, J. Shanghai Jiaotong Univ. (Science), **13**, *6*, pp. 739–743, 2008.
10. BARLAT, F., LIAN, K., *Plastic behavior and stretchability of sheet metals. Part I: A yield function for orthotropic sheets under plane stress conditions*, Int. J. Plasticity, **5**, *1*, pp. 51–66, 1989.
11. CHEN, Z., DONG, X., *The GTN damage model based on Hill'48 anisotropic yield criterion and its application in sheet metal forming*, Comput. Mater. Sci., **44**, *3*, pp. 1013–1021, 2009.
12. BRUNET, M., MORESTIN, F., MGUIL, S., *The Prediction of Necking and Failure in 3 D. Sheet Forming Analysis Using Damage Variable*, J. Phys. IV France, **06**, *C6*, pp. C6-473-C6-482,1996.
13. BRUNET, M., MGUIL, S., MORESTIN, F., *Analytical and experimental studies of necking in sheet metal forming processes*, J. Mater. Proc. Tech., **80-81**, pp. 40–46, 1998.
14. HIBBITT, K., SORENSEN, *ABAQUS/Standard user's manual*, Version 6.11, 2011.
15. LI, Z.H., BILBY, B.A., HOWARD, I.C., *A study of the internal parameters of ductile damage theory*, Fatigue Fract. Eng. M., **17**, *9*, pp. 1075–1087, 1994.
16. ZHANG, Z.L., *A sensitivity analysis of material parameters for the gurson constitutive model*, Fatigue Fract. Eng. M., **19**, *5*, pp. 561–570, 1996.
17. NEEDLEMAN, A., TVERGAARD, V., *An analysis of ductile rupture in notched bars*, J. Mech. Phys. Solids, **32**, *6*, pp. 461–490, 1984.
18. BENSEDDIQ, N., IMAD, A., *A ductile fracture analysis using a local damage model*, Int. J. Pres. Ves. Pip., **85**, *4*, pp. 219–227, 2008.
19. PĂRĂIANU, L., BANABIC, B., *Characterization of the plastic behaviour of AA6016-T4 aluminium alloy*, Adv. Eng. Forum, **8-9**, pp. 293–300, 2013.
20. NICODIM, I., CIOBANU, I., BANABIC, D., *Effect of the constitutive law on the prediction of the wall thickness distribution of square cup*, Proceedings of 11th International MeTM Conference, Cluj-Napoca, Romania, 17–19 October 2013, pp. 173–176.

Received April 3, 2014

THE PUBLISHING HOUSE
OF THE ROMANIAN ACADEMY

PROCEEDINGS OF THE ROMANIAN ACADEMY, Series A,
Volume 15, Number 3/2014, pp. 310–314

EFFICIENT COMPUTATION OF THE NUMBER OF SOLUTIONS OF THE LINEAR DIOPHANTINE EQUATION OF FROBENIUS WITH SMALL COEFFICIENTS

Mugurel Ionuț ANDREICA, Nicolae ȚĂPUȘ

"Politehnica" University of Bucharest, Computer Science Department
Splaiul Independenței 313, 060042, Bucharest, Romania
E-mail: mugurel.andreica@cs.pub.ro

In this paper we present a novel approach for computing the number of solutions of the linear diophantine equation of Frobenius $a_1 \cdot x_1 + ... + a_N \cdot x_N = T$ when the coefficients a_1, ..., a_N are small. The proposed algorithm has a time complexity of the order of $O(N \cdot S \cdot \log(T))$, where $S = a_1 + ... + a_N$. The algorithm can also be implemented to run in $O(S \cdot \log(S) \cdot \log(T) + N \cdot S)$ time, which is more efficient when $\log(S) < N$. Note that an elementary operation in these cases consists of an arithmetic operation (e.g. addition, multiplication) applied on numbers of the order of magnitude of the result, which may be exponential in both N and S. A common situation consists of computing the result modulo a given number P, in which case the arithmetic operation is applied on numbers of the same order of magnitude as P.

Key words: Frobenius equation, knapsack, convolution, discrete Fourier transform.

1. INTRODUCTION

The linear diophantine equation of Frobenius is defined as

$$a_1 \cdot x_1 + ... + a_N \cdot x_N = T, \tag{1}$$

where a_1, ..., a_N and T are positive integer numbers. The unknowns are x_1, ..., x_N, which must also be non-negative integer numbers. Computing the number of solutions of the equation (1) (i.e. the number of different tuples $(x_1, ..., x_N)$ which satisfy the equation) is important in several areas of Mathematics. For instance, [14] discusses their applications to the theory of invariant cubature formulas. Applications of linear Diophantine equations in cryptography are discussed in [3, 9]. Computing the number of solutions of equation (1) also has applications in solving a related problem, that of computing the so-called *Frobenius number*, defined as the largest number T for which equation (1) has no solutions [8, 12].

In this paper we present a novel algorithm for computing the number of solutions of equation (1) in the case when the sum of the coefficients a_1, …, a_N is not too large. T, however, can be as large as we want, because our algorithm's dependency on T is only logarithmic. In Chapter 2 we present the first version of our algorithm, which uses a knapsack-like approach for each bit of the number T. The algorithm presented there performs $O(N \cdot S \cdot \log(T))$ elementary operations. In Chapter 3 we improve the algorithm for the case when $N > \log(S)$, achieving $O(S \cdot \log(S) \cdot \log(T) + N \cdot S)$ elementary operations. Note that in this case we trade-off the knapsack-like simplicity of the core routine of the algorithm presented in Chapter 2 for a more complicated, yet well studied, discrete convolution routine. In Chapter 4 we discuss related work and in Chapter 5 we conclude.

2. A KNAPSACK-BASED ALGORITHM FOR COMPUTING THE NUMBER OF SOLUTIONS

We will represent each unknown x_i ($1 \leq I \leq N$) by introducing $K+1$ independent unknowns, as follows:

$$x_i = x_{i,0} \cdot 2^0 + x_{i,1} \cdot 2^1 + ... + x_{i,K} \cdot 2^K. \tag{2}$$

We choose $K = \log_2(T)$, rounded down to the nearest integer. The unknowns $x_{i,j}$ ($1 \le i \le N$, $0 \le j \le K$) can be either 0 or 1 and are independent from one another. $x_{i,j}$ can be imagined as the bit from position j of x_i. It is obvious that no x_i will have more than $K+1$ bits, as that is the number of bits in the binary representation of T. The algorithm for computing the number of solutions of the Frobenius equation will take advantage of this independence, in the sense that the value of each unknown $x_{i,j}$ (0 or 1) can be considered independently of other unknowns $x_{i,j'}$ (for $j' \ne j$).

Let's denote the bits of T by $t_0, t_1, ..., t_K$, i.e.

$$T = t_0 \cdot 2^0 + t_1 \cdot 2^1 + ... + t_K \cdot 2^K. \tag{3}$$

The proposed algorithm will compute the following values:

$CNT(j,C)$ = the number of ways of choosing the values $x_{i,p}$ ($1 \le i \le N$, $0 \le p \le j$), such that the result of the equation matches the bits 0, ..., j of the number T and we have a „carry" equal to C (i.e. C is a number which influences the result for the next bits, starting from $j+1$). To be more precise, $CNT(j,C)$ = the number of ways of choosing the values $x_{i,p}$ ($1 \le i \le N$, $0 \le p \le j$), such that the obtained number is $t_0 \cdot 2^0 + t_1 \cdot 2^1 + ... + t_j \cdot 2^j + C \cdot 2^{j+1}$.

C will never exceed $S = a_1 + ... + a_N$.

Initially we will have $CNT(-1,0)=1$ and $CNT(-1,1 \le C \le S) = 0$.

Let's assume that we computed all the values $CNT(j,C)$ ($0 \le C \le S$) and we will see how to compute the values $CNT(j+1,C)$ ($0 \le C \le S$). We will use an auxiliary (multidimensional) array $CNTAUX$, where $CNTAUX(i,C)$= the number of ways of obtaining a „sum" equal to C ($0 \le C \le 2 \cdot S$) if we started from the values $CNT(j,*)$ and we considered only the unknowns $x_{p,j+1}$ so far ($1 \le p \le i$).

We will initialize $CNTAUX(0,C)=CNT(j,C)$ for $0 \le C \le S$ and $CNTAUX(0,C) = 0$ for $S+1 \le C \le 2 \cdot S$.

Then, we will consider the unknowns $x_{i,j+1}$, in increasing order of i ($1 \le i \le N$). We have:

$$CNTAUX(i, 0 \le C \le a_i - 1) = CNTAUX(i-1, C). \tag{4}$$

For $a_i \le C \le 2 \cdot S$ we have:

$$CNTAUX(i,C) = CNTAUX(i-1,C) + CNTAUX(i-1, C-a_i). \tag{5}$$

The right-hand side terms from equation (5) correspond to the following two cases: $x_{i,j+1}=0$ and $x_{i,j+1}=1$. Note how equation (5) is similar to the equations used in 0-1 knapsack dynamic programming algorithms [15].

Finally, we will compute the values $CNT(j+1,*)$ from the values $CNTAUX(N,*)$. We have:

$$CNT(j+1, 0 \le C \le S) = CNTAUX(N, 2 \cdot C + t_{j+1}). \tag{6}$$

We consider $CNTAUX(N,C) = 0$ for $C > 2 \cdot S$.

The justification of equation (6) is as follows. So far we matched the bits $t_0, ..., t_j$ of T and now we must match the bit t_{j+1}. Thus, we can only consider values $CNTAUX(N,C)$ where the least significant bit of C is equal to t_{j+1}. After matching the bit $j+1$ of T with a number C, the remaining „carry" (for the bits $j+2, \ldots, K$) is equal to $C/2$ (integer division). Thus, we have $CNT(j+1,C/2)=CNTAUX(N,C)$, where bit 0 of C is equal to t_{j+1}.

The final result can be found in $CNT(K,0)$.

In order to analyze the time complexity of our algorithm, let's notice that a knapsack-like algorithm is run for each bit j. The knapsack-like algorithm takes $O(N \cdot S)$ time. Since there are $\log_2(T)$ bits, we obtain a time complexity of $O(N \cdot S \cdot \log(T))$. An elementary operation in our time complexity analysis consists of adding together two numbers which are of the order of magnitude of the final result. When we care about the exact number of solutions, then these numbers can be exponential in N and S. However, adding together two such numbers is proportional to the number of their digits, which is polynomial in N and S. There are cases when the numbers always remain small, such as when we want to compute the number of solutions modulo a given number P. In these cases the numbers involved are always of the order of magnitude of P (because the additions are performed modulo P). If we can consider the number of digits of P to be a constant value, then an elementary operation truly takes $O(1)$ time.

A trivial implementation of the presented algorithm would use $O(K \cdot S)$ memory. However, we can easily notice that the recurrences for the values $CNT(j,C)$ and $CNTAUX(j,C)$ never need values of the form $CNT(j',*)$ and $CNTAUX(j',*)$ with $j' < j-1$. Thus, it is always sufficient to maintain the last two rows of these two 2D arrays, reducing the required memory to $O(S)$.

3. OPTIMIZING THE ALGORITHM TO O(S·LOG(S)·LOG(T)+N·S)

The algorithm proposed in Chapter 2 can be optimized for the situation when $N>log_2(S)$. We will compute the same values. The values $CNT(0,*)$ and $CNT(1,*)$ will be computed as before. When computing the values $CNTAUX(N,*)$ ($j \geq 1$) we will use a different approach. Let's notice that

$$CNTAUX(N,C) = CNT(j,0)\cdot CNT(1,C) + CNT(j,1)\cdot CNT(1,C-1) + ... + CNT(j,C)\cdot CNT(1,0) = \sum_{x=0}^{C} CNT(j,x)\cdot CNT(1,C-x), \quad (7)$$

where we consider $CNT(*, S+1 \leq C \leq 2\cdot S)=0$.

Equation (7) defines a discrete convolution between the sequences $CNT(j,*)$ and $CNT(1,*)$. $CNTAUX(N,*)$ is computed by applying the convolution operation on these two sequences of size $S+1$. The convolution of two sequences of size $O(S)$ can be computed efficiently, by using the Discrete Fourier Transform, in $O(S\cdot\log(S))$ time [23]. After computing the values $CNTAUX(N,*)$ we obtain the values $CNT(j+1,*)$ from them as before. Note that in this case we do not need to compute the values $CNTAUX(i,*)$ for $i<N$, because we can compute $CNTAUX(N,*)$ directly by using the discrete convolution.

Thus, instead of using a knapsack-like algorithm for computing the values $CNTAUX(N,*)$ at each step, we use an algorithm for computing the convolution of two sequences. The overall time complexity of the modified algorithm is $O(S\cdot\log(S)\cdot\log(T)+N\cdot S)$ (the $O(N\cdot S)$ term comes from computing the values $CNT(1,*)$). The amount of memory used by the algorithm can be as low as $O(S)$, by using the same argument presented in the previous chapter.

When computing the convolution of two discrete sequences we will need to add and multiply numbers which are of the same order of magnitude as the final result (which we will call „large" numbers), or multiply and divide such numbers with „small" numbers (of the order of magnitude of N). We consider the addition of two „large" numbers or the multiplication and division of a „large" number with a „small" number to be equally complex and we will denote them as „simple" operations. The multiplication of two „large" numbers is more complex than the other operations and, thus, we will denote it as a „complex" operation. In the DFT-based discrete convolution algorithm applied for two sequences of length $O(S)$, there are $O(S\cdot\log(S))$ „simple" operations performed and only $O(S)$ „complex" operations. Because of this, we can conclude that an elementary operation in this second version of the algorithm is equivalent to an elementary operation in the first version of the algorithm.

4. RELATED WORK

The problem of computing the number of solutions for the Frobenius equation has been studied before in several papers. A common approach [4, 20, 22] is to find a closed-form function which computes the number of solutions of the equation when given the argument T. This approach uses the fact that this function is the sum of a polynomial of degree $N-1$ and a periodic function with period equal to $LCM(a_1, ..., a_N)$ (LCM = lowest common multiple). The coefficients of the polynomial are rational numbers, but the periodic part has a more complicated structure. The theory of generating functions is usually employed in order to explicitly find the function. In [6] the authors tackle only the polynomial part of the function, which can be computed in time exponential in N. The general case (both the polynomial and periodic parts) has been considered in [16], where an exact representation of the „number of solutions" function is given, which can be computed in a reasonable amount of time for moderately large values of the numbers a_i ($1 \leq i \leq N$) and N.

Even assuming that the "number of solutions" function is fully known, computing the exact number of solutions is not always easy, because computations involving real numbers will be performed. By comparison, our algorithm uses only integer numbers (at least in the first version of the algorithm).

Easily computable closed-form expressions of the „number of solutions" function for simple cases (e.g. $N=2$) have also been derived [19].

A very simple, yet inefficient, algorithm for computing the number of solutions of equation (1) is presented in [18]. The algorithm tries every possible value for x_1, ..., x_{N-1} (the value of x_N is then uniquely determined, if it exists). Obviously, this algorithm is exponential in T, while our algorithm's dependency on T is only logarithmic.

A more popular version of the problem studied in this paper [20] is to compute the so-called Frobenius number, i.e. the largest number T for which the Frobenius equation (1) does not have any solutions. Several algorithms have been proposed for this problem [7, 8, 12]. Reference[6] connects the Frobenius number problem and the problem of computing the number of solutions of equation (1) in a natural manner: the authors are interested in computing the largest number T for which equation (1) has a given number of solutions. Extensions to other types of equations have also been considered [11], as well as extensions to multiple dimensions [2].

Because of its popularity, the problem of finding the Frobenius number has also been considered as a useful educational tool in teaching discrete mathematics (particulary for the well studied case N=2) [5]. Moreover, generalizations of this problem have also been considered [10].

The convolution operation is a very useful tool in a wide variety of domains, both continuous and discrete [1, 17, 24]. A common method of efficiently computing the convolution of two discrete sequences is to apply the Discrete Fourier Transform on each sequence, multiply the obtained coefficients together (position by position), and then apply the Inverse Discrete Fourier Transform in order to obtain the result. Other fast convolution algorithms use the Discrete Fourier transform in other spaces than the space of complex numbers (e.g. in rings) [21].

5. CONCLUSIONS

In this paper we presented a novel algorithm for computing the number of solutions of the Frobenius equation $a_1 \cdot x_1 + ... + a_N \cdot x_N = T$ when the coefficients a_1, ..., a_N are small (so that their sum is not too large). Our algorithm works even when T is very large. N can also be moderately large, as long as the sum S of the coefficients is not too large and the product $N \cdot S$ is also not too large. An elementary operation in our algorithm consists of an arithmetic operation applied on two numbers which are of the same order of magnitude as the final result. When computing the result modulo a given number P, the numbers involved in the computations are of the same order of magnitude as P. However, in this case, the standard Discrete Fourier Transform cannot be used. Instead, the number-theoretic transform must be used, which imposes some constraints on the value of P; of course, these constraints can be overcome, at the expense of more complex implementations [13, 17].

REFERENCES

1. F. ABTAHI, R. N. ISFAHANI, A. REJALI, *Convolution on Weighted L^p-spaces of Locally Compact Groups*, Proceedings of the Romanian Academy, Series A, **13**, *2*, pp. 97–102, 2012.
2. J. AMOS, I. PASCU, V. PONOMARENKO, E. TREVINO, Y. ZHANG, *The Multidimensional Frobenius Problem*, Involve – a Journal of Mathematics, **4**, *2*, 2011.
3. M. R. K. ARIFFIN, N. A. ABU, *Linear Diophantine Equation Discrete Log Problem, Matrix Decomposition Problem and the AA_β-Cryptosystem*, IACR Cryptology ePrint Archive, 2011.
4. A. BADRA, *Frobenius Number of a Linear Diophantine Equation*, Lecture Notes in Pure and Applied Mathematics, **231**, pp. 23–36, 2003.
5. M. BECK, *How to Change Coins, M&M's, or Chicken Nuggets: The Linear Diophantine Problem of Frobenius*, in *Resources* for Teaching Discrete Mathematics: Classroom Projects, History Modules, and Articles (B. Hopkins, ed.), pp. 65–74. Mathematical Association of America, 2009.
6. M. BECK, I. M. GESSEL, T. KOMATSU, *The Polynomial Part of a Restricted Partition Function related to the Frobenius Problem*, The Electronic Journal of Combinatorics, **8**, *1*, 2001.
7. M. BECK, S. ROBBINS, *Computing the Continuous Discretely*, Springer, 2009.
8. D. BEIHOFFER, J. HENDRY, A. NIJENHUIS, S. WAGON, *Faster Algorithms for Frobenius Numbers*, The Electronic Journal of Combinatorics, **12**, 2005.
9. D. BISHOP, *Introduction to Cryptography with Java Applets*, Jones and Bartlett Publishers, 2003.
10. A. BROWN, E. DANNENBERG, J. FOX, J. HANNA, K. KECK, A. MOORE, Z. ROBBINS, B. SAMPLES, J. STANKEWICZ, *On a Generalization of the Frobenius Number*, Journal of Integer Sequences, **13**, 2010.
11. M. DELGADO, J. C. ROSALES, *On the Frobenius Number of a Proportionally Modular Diophantine Inequality*, Portugaliae Mathematica - Nova Serie, **63**, *4*, pp. 415–425, 2006.
12. D. EINSTEIN, D. LICHTBLAU, A. STRZEBONSKI, S. WAGON, *Frobenius Numbers by Lattice Point Enumeration*, Integers, **7**, *1*, 2007.

13. W. B. HART, G. TORNARIA, M. WATKINS, *Congruent Number Theta Coefficients to 10^{12}*, Algorithmic Number Theory: 9th International Symposium ANTS-IX, Springer-Verlag, 2010, pp. 186–200.
14. M. I. ISRAILOV, *Numbers of Solutions of Linear Diophantine Equations and Their Applications in the Theory of Invariant Cubature Formulas*, Siberian Mathematical Journal, **22**, *2*, pp. 260–273, 1981.
15. H. KELLERER, U. PFERSCHY, D. PISINGER, *Knapsack Problems*, Springer-Verlag, 2004.
16. T. KOMATSU, *On the Number of Solutions of the Diophantine Equation of Frobenius – General Case*, Mathematical Communications, **8**, pp. 195-206, 2003.
17. L. M. LEIBOWITZ, *Fast Convolution by Number Theoretic Transforms*, Naval Research Laboratory, Washington D.C., 1975.
18. R. MAHMOUDVAND, H. HASSANI, A. FARZANEH, G. HOWELL, *The Exact Number of Nonnegative Integer Solutions for a Linear Diophantine Inequality*, IAENG International Journal of Applied Mathematics, **40**, *1*, 2010.
19. T. POPOVICIU, *Asupra unei Probleme de Partiție a Numerelor*, Studii și Cercetări Științifice, **4**, pp. 7–58, 1953.
20. J. L. RAMIREZ ALFONSIN, *The Diophantine Frobenius Problem*, Oxford Lecture Series in Math. and its Appl., **30**, Oxford Univ. Press, Oxford, 2005.
21. A. SCHÖNHAGE, V. STRASSEN, *Schnelle Multiplikation großer Zahlen*, Computing, **7**, pp. 281–292, 1971.
22. S. SERTÖZ, *On the Number of Solutions of a Diophantine Equation of Frobenius*, Discrete Mathematics and Applications, **8**, *2*, pp. 153–162, 1998.
23. D. SUNDARARAJAN, *The Discrete Fourier Transform: Theory, Algorithms and Applications*, World Scientific Publishing, 2001.
24. G. ZBĂGANU, *On Infinite Bernoulli Convolutions*, Proceedings of the Romanian Academy, Series A, **7**, *3*, 2006.

Received May 20, 2013